Astronomy & Astrophysics manuscript no. xitau
April 14, 2016

ξ Tauri: a unique laboratory to study the stellar and dynamical evolution of a multiple system

J.A. Nemravová[1], P. Harmanec[1], M. Brož[1], D. Vokrouhlický[1], D. Mourard[2], C.A. Hummel[3], C.T. Bolton[4], I. Tallon-Bosc[5,6,7,8], H. Božić[9], C. Cameron[10], R. Chini[11,12], S. Engle[13], C. Farrington[14], J.H. Grunhut[3], T. Dembsky[11], D.B. Guenther[15], E.F. Guinan[13], D. Korčáková[1], P. Koubský[16], R. Kříček[1], R. Kuschnig[17], J.M. Matthews[10], P. Mayer[1], G.P. McCook[13], A.F.J. Moffat[18], N. Nardetto[2], A. Prša[13], J. Ribeiro[19], J. Rowe[20], S. Rucinski[4], P. Rutsch[1], P. Škoda[16], M. Šlechta[16], V. Votruba[16], W.W. Weiss[17], M. Wolf[1], and P. Zasche[1]

(Affiliations can be found after the references)

Release April 14, 2016

ABSTRACT

Compact hierarchical systems are very rare but their importance for astrophysics is tremendous. Apart from a chance to determine all basic physical properties of all their components (basically free of any calibration) there is also a chance to study dynamical interactions of the components and test theoretical predictions through real observations on a human time-scale. The dynamical interaction also plays a crucial role in the formation of close binaries by Kozai cycles with tides (KCT).

This study provides perhaps the most complex investigation of one such object, ξ Tauri = HD 21364, which is a hierarchical quadruple system composed from an eclipsing binary of two A stars in 7.15 d orbit, B type tertiary in an intermediate 145 d orbit, and a low-mass (possibly F-type) fourth component in an outer 51 yr speckle-interferometric orbit. It is based on extended series of observations from several observatories: ground-based spectral and photometric observations, the high-precision space photometry acquired continuously over two weeks with the satellite MOST, and optical spectro-interferometric observations with the MARK III, NPOI, and CHARA/VEGA instruments.

To infer the properties of the system we used following approaches: (i) A set of "observation-specific" models to fit one type of the observables (radial-velocities, line spectra, light curves, squared visibilities, or astrometric positions), from which the optimal model parameters were estimated using the χ^2 minimisation; and (ii) a complex N-body model, in which each component is represented as a point mass. Starting from a set of osculating elements and masses of individual components, the equations of motions were integrated (forward and backward) over the time interval covered by observations. The osculating elements were then optimised with respect to all observations and a joint χ^2. This way we were able to compare performance of different observational methods.

Our principal results are: (1) The triple subsystem exhibits clear signs of a dynamic interaction between the inner and intermediate orbit: apsidal advance of the 145 d orbit and previously undetected eclipse timing variations. (2) We determined the geometry of all three orbits using both the observation-specific and N-body models. The N-body model properly accounted for the majority of the dynamical interactions between the components. It correctly fitted the newly detected eclipse timing variations, the secular evolution of the argument of periastron of the intermediate orbit, and cyclic variations of the inclinations of the 7.15 d and 145 d orbits. The model was even able to distinguish between the prograde (preferred) and retrograde solutions. (3) Using the perturbation theory we realised that a quadrupole interaction in the triple subsystem is responsible for the detected apsidal motion and eclipse timing variations. (4) The properties of individual stars were obtained with the observation-specific models. Thanks to the MOST photometry we were able to put tight constraints on the masses, radii, and effective temperatures of both components of the inner binary as well as to detect rapid light variations and attribute them to the rotating structures on the surface of the B tertiary. The high angular resolution of the CHARA/VEGA instrument allowed us to resolve the angular radius of the third body. We were also able to estimate its effective temperature and mass. The only component whose properties were not tightly constrained is the distant low-mass fourth component since we were unable to detect its spectral lines in any parts of the spectra available to us (mainly due to its low relative luminosity). (5) We obtained independent estimates of the distance to the system.

The observations of this rare system should definitely continue but already our current results provide an excellent material for forthcoming tests of stellar and/or binary evolution models..

Key words. Stars: binaries: close – Stars: binaries: spectroscopic – Stars: fundamental parameters – Stars: individual: ξ Tau

1. Introduction

Binaries and multiple systems play a crucial role in our understanding of the formation, stability, and evolution of stars and their hierarchies starting from simple binaries up to galaxies.

Among all known binaries, the eclipsing ones has represented the most useful group, since - until recently - accurate determination of component masses and radii was possible primarily for them. For binaries with components of different masses, the joint origin of the system also provided a stringent test of the models of stellar evolution. At the same time, however, this fact represented an unpleasant selection effect, especially for binaries with hot components and rapid rotation: we have observed them roughly equator-on only.

The recent rapid advances in the optical interferometry allowing the usage of longer baselines, co-phasing of more tele-

Send offprint requests to: J.A. Nemravová,
e-mail: janicka.ari@seznam.cz

Table 1. Journal of spectroscopic observations. For each instrument: ΔT refers to time span between the first and the last measurement, N gives the number of RVs measured for components Aa, Ab, and B, respectively, $\Delta\lambda$ is the wavelength interval covered by the spectra in question, and R is a two-pixel spectral resolution.

ΔT	N	$\Delta\lambda$	R	Ins.
(RJD)	Aa/Ab/B	(Å)		
49300.7–52670.5	37/37/37	4357–4568	10800	DDO
51960.3–53637.6	04/04/04	4270–4523	42000	ELO
	04/04/04	4759–4991		
	04/04/04	6260–6735		
55041.9–55867.6	13/13/13	4270–4523	48000	BES
	13/13/13	4759–4991		
	13/13/13	6260–6735		
55579.4–56357.3	34/34/34	4270–4523	19200	OND
56579.4–56889.6	05/04/05	4274–4508	19200	OND
55579.3–55645.3	02/02/02	4378–4632	17700	OND
55579.3–56357.3	20/20/20	4753–5005	19300	OND
56527.6–56592.5	05/05/05	4759–4991	21500	OND
56527.6–56889.6	14/14/14	6260–6735	14000	OND
55561.3–56357.3	58/58/59	6255–6767	12700	OND
55597.4–55980.3	19/19/22	6497–6688	14000	LIS
56555.7–56564.7	12/12/12	4270–4523	48000	FER
	12/12/12	4759–4991		
	12/12/12	6260–6735		

Notes. In column 'Ins.':
DDO - David Dunlap Observatory 1.9 m reflector, Cassegrain CCD spectrograph; ELO - Haute Provence Observatory 1.2 m reflector, echelle ELODIE CCD spectrograph; BES - Cerro Amazones hexapod reflector, BESO echelle CCD spectrograph; OND - Ondřejov Observatory 2 m reflector, coudé CCD spectrograph; LIS - Lisbon Observatory of the Instituto Geográfico do Exército, reflector, CCD spectrograph; FER - La Silla 2.2 m reflector, Feros echelle CCD spectrograph.

scopes and longer integration times, provided the chance to obtain accurate basic physical properties also for of non-eclipsing binaries. It is possible to obtain the spatial orbit of such binaries and derive their accurate orbital inclination. In combination with radial-velocity (RV) curves, this allows the determination of component masses and the absolute value of the semi-major axis. Since the interferometric orbit provides the angular value of the semi-major axis, one also obtains an estimate of the distance of the binary, which is completely independent of the photometric distance modulus. In the most favourable cases, long-baseline interferometry can also provide independent estimates of the component radii.

Large number of binaries are actually members of multiple systems (Eggleton & Tokovinin 2008). In cases, when it is possible to derive masses of more than two components, one can study not only the nuclear but also the dynamical evolution of such systems. In some favourable cases, the dynamical interaction between orbits via the Kozai cycles with tidal friction (Eggleton & Kiseleva-Eggleton 2001; Fabrycky & Tremaine 2007) may cause observable effects. In order to compare the predictions of the theory with observations for a triple system, one has to know the mutual orientation of orbits with respect to each other, i.e. their inclinations and the longitudes of ascending nodes. These are available only for objects for which the astrometric orbit is known. This in turn can only be obtained with the interferometry.

This study is devoted to an investigation of one such system, a unique and rare close quadruple system ξ Tau, whose favourable orbital geometry and luminosity ratios between its components allow the determination of physical properties of the system and its components with a high precision and to study possible dynamical effects in the system. ξ Tau (2 Tau, HD 21364, HIP 16083, HR 1038) is a hierarchical quadruple system, consisting of two sharp-lined A stars, which undergo binary eclipses, a more distant broad-lined B star and a much more distant F star. The visual magnitude V =3.72 mag, the declination of $9°44'$, and quite accurate Hipparcos parallax 15.6 ± 1.04 mas (van Leeuwen 2007) make ξ Tau an easy and interesting target for a wide range of instruments and observational techniques.

The binary nature of the system was discovered by Campbell (1909). The wide orbit was first resolved by Mason et al. (1999) via speckle interferometry. All later available speckle-interferometric observations were analysed by Rica Romero (2010), who derived an astrometric orbit. The inner triple system was first mentioned by Fekel (1981), who quoted orbital periods of 7.15 d and 145.0 d based on a private communication from Dr. C.T. Bolton. The orbital elements of the triple subsystem were published in a catalogue by Tokovinin (1997). More accurate elements were given in a preliminary report by Bolton & Grunhut (2007), who obtained periods of 7.1466440(49) d and 145.1317(40) d. They were also the first to note that the inner binary is an eclipsing system, based on Hipparcos photometry. Hummel et al. (2013) reported a solution of the 145.2 d orbit based on interferometric observations. The first detailed, but still preliminary study of ξ Tau was published by Nemravová et al. (2013). These authors analysed numerous spectral, photometric and interferometric observations and discovered the presence of apsidal motion of the 145.2 d orbit with an apsidal period of 224 ± 147 yrs. They were able to disentangle the spectra of both A stars and the broad-lined B star.

This paper represents a very complex study of the system, based on detailed analyses of a huge and unique body of spectral, photometric and (spectro)interferometric and speckle-interferometric data. Each type of observations is first analysed separately by more or less standard means (chapters 3, 4, and 6) and the results are then confronted and critically compared in sect. 7. Using them as the initial starting point, we then present the N-body model of the whole quadruple system, in which also the mutual interactions of the orbits is modelled. This is a new approach, which tries to embrace the largest number of available pieces of information and which provides the best description of the geometry and dynamics of the system to date (see section 8.1). Finally, this approach is complemented by a purely theoretical model of the dynamical evolution of the close triple subsystem (sect. 9).

In the following text we shall denote the individual components and orbits of the system as follows: Components Aa and Ab are the primary and secondary of the close eclipsing subsystem revolving in a 7.15 d orbit 1. Component B is the broad-lined star of spectral type B, revolving with the close pair in the 145 d orbit 2. Finally, we denote the faint and very distant F-type star as component C and its 51 yr orbit with the triple subsystem as orbit 3.

2. Observations and reductions

To facilitate a smooth reading of the main text, we provide here only basic information about the observational material at our

disposal. More details on the datasets and their reductions are in Appendices.

Throughout this paper we use a shortened form of heliocentric Julian dates, reduced Julian dates given as RJD = HJD−2400000.0 .

2.1. Spectral observations

The series of spectroscopic observations, which has already been used by Nemravová et al. (2013) was complemented with more recent ones secured at Ondřejov, La Silla: echelle spectrograph FEROS (Kaufer et al. 1999), and Cerro Armazones: the BESO spectrograph (Steiner et al. 2008; Fuhrmann et al. 2011). Four archival ELODIE echelle spectra were also used (Moultaka et al. 2004). Having now a rich collection of electronic spectra, we no longer used the early RVs from the DDO photographic spectra, used by Nemravová et al. (2013). The spectra were primarily used to RV measurements of all three components of the close triple subsystem. The journal of all available spectra with the number of measured RVs is in Table 1. More details on the spectra and their reductions can be found in Appenxix A

2.2. Photometric observations

Photometry, which has already been used by Nemravová et al. (2013) was complemented by very accurate observations acquired almost continuously over two weeks with the MOST satellite (Walker et al. 2003), and by another series of Johnson UBV and $UBVR$ observations from Hvar. Additionally, we also analysed the photometric minima published by Zasche et al. (2014).

The MOST satellite monitored ξ Tau over 16 days almost continuously. It acquired 21525 observations, which – after the initial reduction by the MOST team – were still affected by two systematic effects: (i) The stray light from the Earth atmosphere, which introduced narrow peaks with separation $\approx$ 101 minutes, and (ii) the relaxation time after the change of the observed field, during which the CCD had to reach a thermal equilibrium. It manifests itself by a slowly decreasing offset. It usually takes several tens of minutes. The first effect was, with the exception of a few observations during the eclipses, removed with a low-passband Butterworth filter (Butterworth 1930). The second effect forced us to neglect all observations secured prior to RJD = 56522. The remaining 18510 observations were then subjected to analyses.

Journal of available photometric observations is in Table 2 and more details on the observations and data reductions can be found in Appendix B.

2.3. Interferometric observations

The system was observed by three different optical (spectro)-interferometers: (i) The Mark III Stellar Interferometer[1] (Mark III) (Shao et al. 1988), (ii) the Navy Precision Optical Interferometer (NPOI) (Armstrong et al. 1998), and (iii) the Visible spEctroGraph and polArimeter (VEGA) (Mourard et al. 2009) mounted at the Centre for High Angular Resolution Astronomy (CHARA) (ten Brummelaar et al. 2005). The observations from each interferometric instrument and their reductions are described in the following subsections and the journal of the (spectro)-interferometric observations is in Table 3. The phase coverage of orbits 1 and 2 with all spectro-interferometric observations is shown in Figure 1. More details on the (spectro)-interferometric observations are provided in Appendix C.

[1] Decommissioned in 1992.

Table 3. Journal of the (spectro)-interferometric observations. ΔT is the RJD of the first and the last observation, ΔB the range of the projected baselines, $\Delta\lambda$ the wavelength range, and N the total number of visibility observations.

Instr.	ΔT (RJD)	ΔB (m)	$\Delta\lambda$ (Å)	N
1	48275-48563	14-30	5000-8000	108
2	51093-56298	0-79	5500-8500	13461
3	55825-56228	31-279	5320-7600	6132

Notes. In column 'Instr.': 1 - Mark III, 2 - NPOI, 3 - CHARA/VEGA.

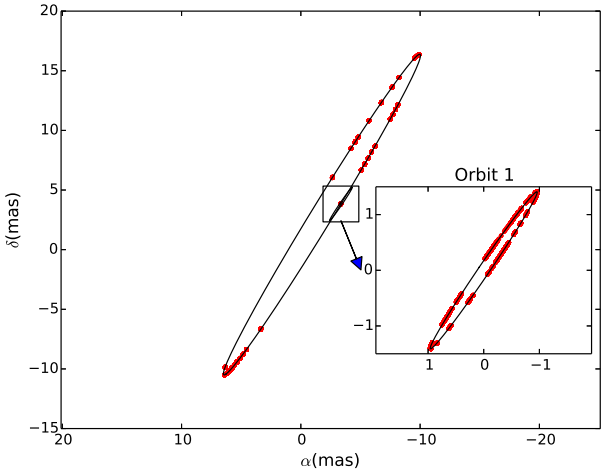

Fig. 1. Phase coverage of orbits 1 and 2 with the spectro interferometric observations. The two orbits are shown as they would appear on the celestial sphere. The orbit 1 is shown only at a certain epoch. It is almost invisible, so it is zoomed in the inset plot. The red dots denote individual spectro-interferometric observations acquired with all available instruments.

3. Spectroscopy

The spectral lines of all three components of the triple subsystem (i.e. orbits 1 and 2) of ξ Tau are clearly seen in all available spectra. The fourth component C was not detected in any of the spectra at our disposal, because its relative luminosity being less than 1%, which is beyond the detection limit of the available spectra. Attempts to detect its spectral lines were carried out via the spectral disentangling and a comparison of the near infrared spectra with the synthetic profiles, both with null results.

Two different approaches to derive the orbital elements of the triple subsystem of ξ Tau were used. The first one was a direct analysis of RVs measured with the method described below and the second one was the spectral disentangling (Simon & Sturm 1994; Hadrava 1995).

Additionally, we also derived the basic radiative properties of ξ Tau using the comparison of the synthetic spectra to observed ones and also disentangled ones.

Table 2. Journal of photometric observations. For each row: N is the number of observations in each of the filters used, ΔT is the time span covered by each dataset, column 'Passbands' shows the photometric filters used, column 'Comp/Check' lists the names of comparison and check star used. UBV and $UBVR$denote the Johnson filters (Johnson, not Cousins R filter is used at Hvar) and MO denotes the broad-band filter of the MOST satellite.

N	ΔT (RJD)	Passbands	Comp / Check	Instrument
429/439/440	46324.6–55945.3[1]	UBV	4 Tau / 6 Tau	HVAR
69	47909.6–48695.0	$V(H_{\rm p})$[2]	all-sky	HIPP
26/26/26	55569.3–55579.4	UBV	6 Tau / 4 Tau	SAAO
131/133/135	55883.9–55956.8	UBV	4 Tau / 6 Tau	VILL
18510	56222.0–56238.0	MO	all-sky	MOST
12/12/12/12	56520.6–56882.6	$UBVR$	4 Tau / 6 Tau	HVAR

Notes. [1]Only three observations were taken before RJD=54116, all at RJD=46324. [2]The original Hipparcos $H_{\rm p}$ broad-band observations were transformed to the Johnson V filter after Harmanec (1998). Note, however, that for the light-curve solutions the limb darkening coefficients corresponding to the original MOST passband were used.
Notation in column 'Instrument': HVAR - Hvar Observatory 0.65 m Cassegrain reflector, photoelectric photometer; HIPP - The ESA Hipparcos Astrometric Mission; SAAO - South African Astronomical Observatory 0.5 m Cassegrain reflector, Lucy photoelectric photometer; VILL - the Four College 0.8 m reflector, photoelectric photometer; MOST - the Canadian MOST satellite.

3.1. RVs measured via comparison of the observed and synthetic line profiles

RVs were derived using an automatic method based on the comparison of synthetic and observed spectra, searching for the best match with the optimisation of χ^2 given by:

$$\chi^2\left(RV_j\right) = \sum_{i=1}^{N_{\rm I}} \left(\frac{I_{\rm OBS}\left(\lambda_i\right) - \sum_{j=1}^{N_{\rm C}} I_{{\rm SYN},j}\left(\lambda_i, RV_j\right)}{\sigma_i} \right)^2 , \quad (1)$$

where $I_{\rm OBS}$ is the observed spectrum, $I_{{\rm SYN},j}$ the synthetic spectrum of the j-th component, $N_{\rm I}$ is the number of discrete elements of the digitised spectrum, $N_{\rm C}$ is the number of the components of the system, RV_j the radial velocity of the j-th component, and σ_i the standard deviation of the i-th point of the observed spectrum, which was estimated from the continuum and adopted for the whole spectrum.

The majority of the spectra at our disposal was acquired in three wavelength regions $\Delta\lambda \in \{4200-4500; 4750-5000; 6200-6700\}$ Å Each region contains a Balmer line, which turned out to be the best one for measurement of RV of component B and several metallic lines, which gave accurate RVs of components Aa and Ab. These regions were also extracted from echelle spectra, and RVs were measured on each region independently. The last region (Hα) contains a number of telluric lines. Although we tried to use mainly the parts of the spectra, not affected by the telluric lines $\approx \{6275-6333; 6440-6530\}$ Å, it was not possible for Hα, which contains a large number of them. Consequently, it was impossible to acquire accurate RV of Hα with this technique.

Initial RVs for the searching program were computed from the orbital solution presented in Nemravová et al. (2013) and the RV for each component was searched over the interval $[-70; 70]$ km s^{-1} surrounding the initial estimate. The similarity of components of the eclipsing binary (Aa, Ab) required us to control whether the two components have not been interchanged by the program, especially near the conjunctions. If they were, the search was repeated using a narrower search intervals.

RVs and their uncertainty were estimated in the following way:

1. The parameters of synthetic spectra were chosen randomly from the Gaussian distributions centred at values listed in Table 6 and the standard deviations were set to their uncertainties.
2. The synthetic spectra were fitted to the observed ones. The procedure was repeated five hundred times for each spectrum and the RV was estimated from the resulting distribution.

We note that this approach allowed to estimate only the 'statistical' part of the total error. Usually, the statistical uncertainty $\Delta RV_{\rm stat}$ was $\leq$ 1 km s^{-1} for components Aa, and Ab and $\leq$ 10 km s^{-1} for component B. The measurement of RVs of component B was more difficult, because the majority of metallic lines in its spectrum is very shallow and smeared out by the high rotational velocity of component B. The measurements also turned out to be very sensitive to the choice of the model and its discrepancies.

The telluric lines in the red and IR parts of the spectra were used to correct for the variations of the zero-point of the RV scale. Such corrections were typically ≤ 2 km s^{-1} for the Ondřejov spectra, hence all measurements for which the RV zero-point could not be checked this way were assigned uncertainty $\max(\Delta RV_{\rm stat}, 2)$ km s^{-1}, and the remaining ones were assigned uncertainty $\max(\Delta RV_{\rm stat}, 1)$ km s^{-1}, where 1 km s^{-1} is the upper bound of the precision of the zero-point correction for the Onřejov spectra.

3.2. Direct analysis of RVs

Since we were not aware of any publicly available program for orbital solutions of hierarchical systems with apsidal advance of the outer orbit(s), JN has developed such a program. The measured RVs were fitted with a model, which takes into account the two dynamical interactions between the three or four components. The effects considered are the apsidal motion of orbit 2, and the light-time (LITE) effect produced by orbits 2 and 3. The RVs of the j-th component RV_j were fitted with the standard Keplerian model:

$$RV_{\rm j}(t) = \sum_i K_{\rm i} \left[\cos\left(\omega_{\rm i}(t) + v_{\rm i}(t)\right) + e_{\rm i} \cos\omega(t)_{\rm i} \right], \quad (2)$$

where the index i goes over those orbits of ξ Tau, which are relevant for the motion of the j-th component of the ξ Tau system,

$K_{\rm i}$ the semiamplitude of the RV curve, $\omega_{\rm i}$ the argument of periastron, $v_{\rm i}$ the true anomaly, $e_{\rm i}$ the eccentricity, and t is time. The light-time correction (LITE) $\Delta t_{\rm LITE}$ was computed from

$$\Delta t_{\rm LITE,j}(t) = \sum_i \frac{P_i K_i \left(1-e_i^2\right)^{\frac{3}{2}}}{2\pi c} \frac{\sin\left[\omega_i(t)+v_i(t)\right]}{1+e_i\cos v_i(t)}, \qquad (3)$$

where the index i goes over those orbits, which are hierarchically above that one, in which the j-th component lies (i.e over those, which produce LITE), P is the orbital period, and c the speed of light. Otherwise the notation is the same as for the Eq. (2). The argument of periastron is a linear function of time $\omega_i(t) = \omega_i(t_0) + \dot{\omega}_i\,(t-t_{0,i})$, where $t_{0,i}$ is the reference epoch, $\dot{\omega}_i$ is the mean apsidal motion of the i-th orbit.

The model elements were optimised by searching the minimum of the following χ^2:

$$\chi^2 = \sum_{k=1}^{N_{\rm S}} \sum_{j=1}^{N_{\rm C}} \sum_{l=1}^{N_{\rm O}} \frac{1}{\sigma_{j,l}^2} \left[RV_j^{\rm OBS}(\tilde{t}_{j,l}) - RV_j^{\rm SYN}\left(\tilde{t}_{j,l}\right) - \gamma_k\right]^2, \qquad (4)$$

where the index k goes over $N_{\rm S}$ subsets of the measured RVs, which are defined in Table 1, the index j over $N_{\rm C}$ components of the ξ Tau system for which RVs were measured, and the index l goes over $N_{\rm O}$ individual measurements of the RV and $\tilde{t}$ is time corrected for the LITE. σ denotes individual rms of the RVs estimated with the procedure described in Section 2, $RV^{\rm OBS}$ the measured RV, $RV^{\rm SYN}$ the model RV computed with Eq. (2), and corrected for the LITE via Eq. (3), and γ denotes the systemic velocity. Minimum of χ^2 given by Eq. (4) was searched with the Sequential Least Squares (Kraft 1988).

As discussed above, RVs of component B are less accurate than those of components Aa, and Ab. Hence only RVs of the members of the eclipsing binary were fitted to obtain the majority of orbital elements. The individual subsets for individual types of the spectra gave very similar values of the systemic velocity (within 3σ), hence all available measurements were grouped together and a joint systemic velocity was derived for them. Once a final solution was obtained, the measurements were complemented with measurements of RVs of component B and the mass ratio q_2 was optimised (keeping the remaining parameters fixed). The parameters corresponding to the best-fit solution are listed in Table 4. RVs and the best-fitting model are plotted against time (to show the secular evolution of the periastron argument) for orbit 2 in Figure 2, and against phase for orbit 1 in Figure 3.

The uncertainties of individual parameters were estimated locally. The uncertainty of the mass ratio q_2, does not account well for the systematic errors of RVs of component B. Robustness test (i.e. similar fit carried out for subsets of all measurements) has shown that $\Delta q_2 = 0.1$ is a more realistic estimate.

The reduced $\chi^2_{\rm R} \approx 2$ is probably caused by: 1) variations of the zero-point larger than what we accounted for (we note that the estimate is based on the variations of the zero-point measured on the Ondřejov red spectra), 2) by the fact that the synthetic spectra need not correspond to the observed ones in all details, which is something what we cannot account for properly.

We also fitted a model including orbit C fixed at the orbital elements given in Table 8. The reduced chi-square was only marginally ($\leq 1\%$) lower than the one in Table 4. It is not surprising, since the semiamplitude of the RV caused by the revolution of the triple subsystem around the common centre of gravity with component C is ≈ 1 km s^{-1} and the LITE produced by that motion is $\approx 6.10^{-3}$ d, i.e. both beyond the detection limit of our measurements.

Table 4. Parameters of the two-orbit (1 and 2) fit given by Eqs. (2), and (3) to measured RVs. $P_{\rm AN}$ denotes the anomalistic period, $T_{\rm min}$ the epoch of the primary minimum of the light curve, $T_{\rm p}$ the epoch of the periastron passage.

El.	Units	Values	
Orb.		1	2
$P_{\rm AN}$	(d)	7.14664±0.00001	145.598±0.041
$T_{\rm min}$	(RJD-56220)	4.7067±0.0025	–
$T_{\rm p}$	(RJD-56600)	–	9.07±0.57
K	(km s^{-1})	87.670±0.24	38.31±0.19
e		0.0[1]	0.2048±0.0048
q		0.9439±0.0037	0.89±0.10
ω	(deg)	90[1]	8.07±1.48
$\dot{\omega}$	(deg.yr^{-1})	0.0[1]	3.04±0.28
N		748	
$\chi^2_{\rm R}$		2.138	
		Systemic velocity	
v_γ	(km s^{-1})	8.44 ± 0.13	

Notes. [1]The parameter was fixed. K_1 refers to the primary of the eclipsing binary $K^{\rm Aa}$, and K_2 to the centre of gravity of the eclipsing binary $K^{\rm Aa+Ab}$.

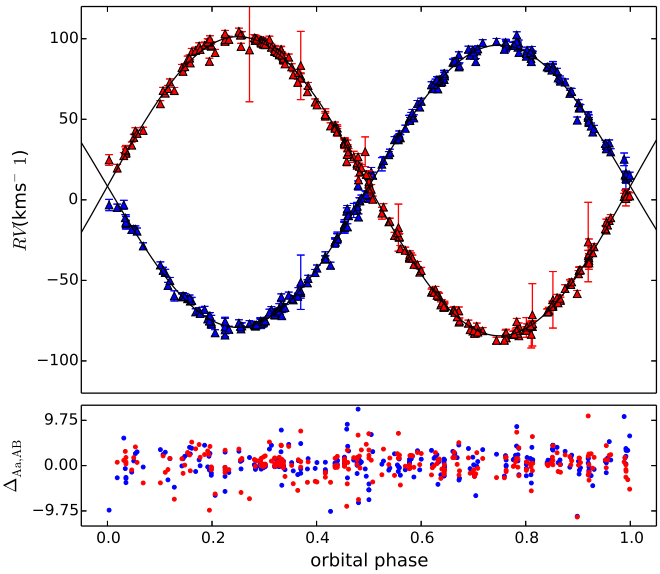

Fig. 3. RVs of components Aa (red), and Ab (blue) relative to the centre of gravity of the eclipsing binary against the best-fitting model (black) listed in Table 4. $\Delta_{\rm Aa,Ab}$ are residuals of the fit and components Aa, and Ab.

3.3. Spectra disentangling

We were only able to disentangle the spectra in the vicinity of four major spectral lines Hα, Hβ, He I 4471 Å, Mg II 4481 Å, and Hγ, since only these regions were available for both, the slit and echelle spectra. An attempt was made to disentangle the spectra of individual components using only the spectra from the three available echelle spectrographs. However, these disentangled spectra had strongly warped continua and were not helpful for further investigation.

The program KOREL (Hadrava 1995, 1997, 2009) (rel. 04-2004), which not only disentangles the spectra, but also fits the spectroscopic orbital elements, was used. This gave us the oppor-

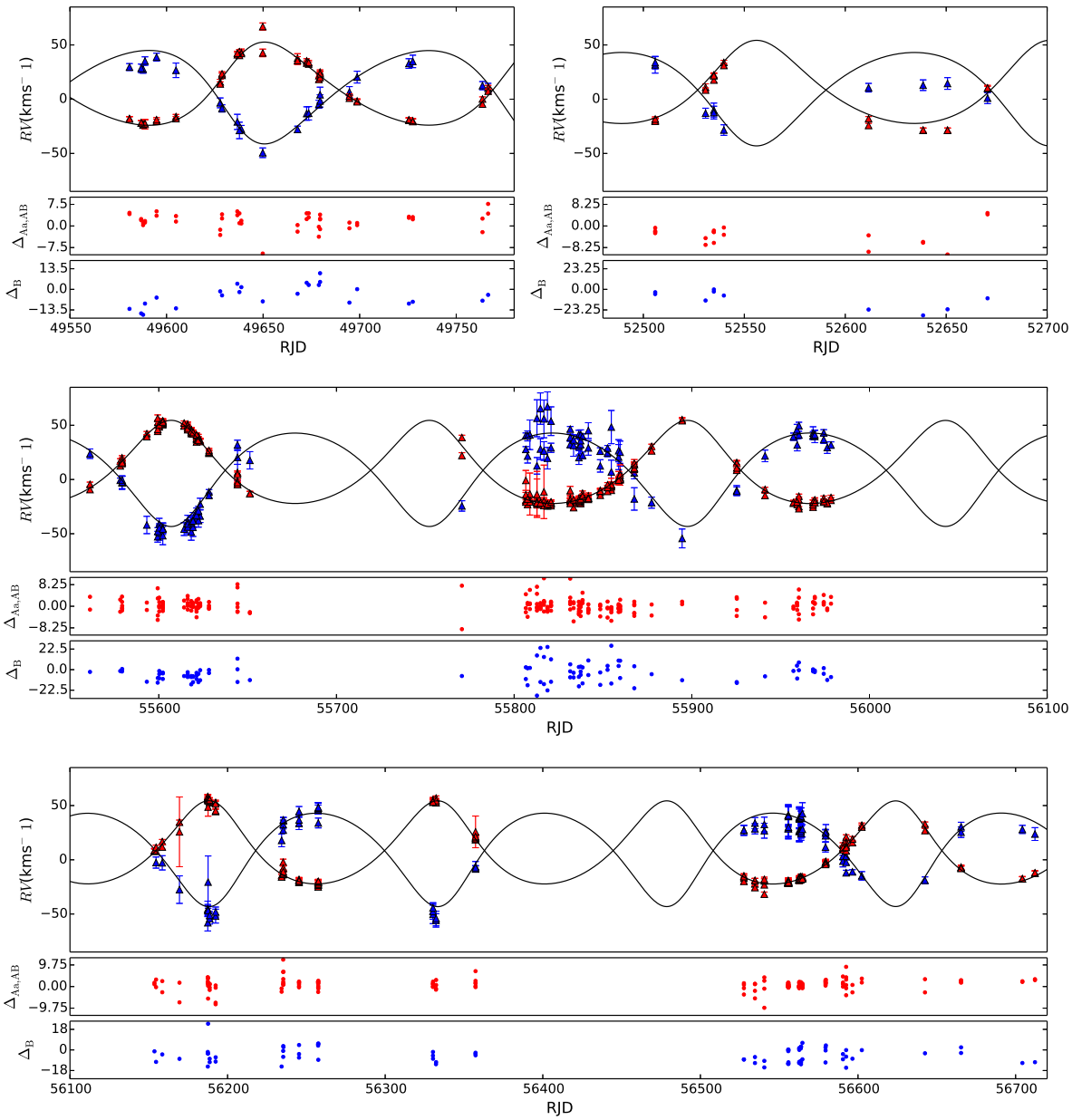

Fig. 2. RVs of the centre of gravity of the eclipsing binary (red triangles), and component B (blue triangles) against the best-fitting model (black) corresponding to parameters listed in Table 4. $\Delta_{\mathrm{Aa,Ab}}$ are residuals of the fit and RVs of the centre of gravity of the eclipsing binary, and Δ_{B} residuals of the fit and RVs of component B.

tunity to compare the orbital solution obtained directly from the measured RVs with the result of KOREL. Only components B, Aa, and Ab were fitted, since component C is not detectable. Relative luminosities of all three components were kept constant during the orbital motion. This assumption, although not exactly satisfied because of the presence of shallow eclipses of components Aa and Ab, was necessary for the stability of the disentangling.

The orbital elements presented in Table 4 served as the starting estimates for the minimisation. The spectroscopic orbital elements obtained with KOREL are in Table 5. The disentangled profiles from the considered spectral regions are shown in Figure A.1. KOREL does not provide the uncertainties of the fitted elements. Therefore a map of the χ^2 around the minimum found with the minimisation engine was drawn for every combination of two fitted parameters. The uncertainties, which are listed in

Table 5. Orbital elements obtained by KOREL (spectra disentangling) for all available spectra containing at least one of the studied regions. The orbital model consists of orbits 1 and 2.

Elem.	Unit		
Orbit		1	2
$P_{\rm AN}$	(d)	7.14664±0.00002	145.612±0.056
$T_{\rm min}$	(RJD-56220)	4.6963±0.0040	–
$T_{\rm p}$	(RJD-56000)	–	9.29±1.44
K	(km s^{-1})	87.52±0.59	37.55±0.57
e		0.000[1]	0.180±0.024
q		0.943±0.008	1.02±0.27
ω	(deg)	90.000[1]	8.52±4.1
$\dot{\omega}$	(deg.yr^{-1})	0.000[1]	3.032±0.38
$\chi^2_{\rm R}$		1.19	

Notes. [1]The parameter was fixed. K_1 refers to primary of the eclipsing binary $K^{\rm Aa}$, and K_2 to the centre of gravity of the eclipsing binary $K^{\rm Aa+Ab}$.

Table 5 correspond to 68% confidence intervals (roughly one σ) estimated from these maps.

An attempt was carried out to disentangle lines of component C in two spectral bands in the near infrared, $\Delta\lambda_{\rm IR} = \{7750-7800, 8570-8800\}$ Å. Spectrum of component C was not detected in either of these bands. It was probably caused by the relatively low S/N of the echelle spectra in the infrared region and their limited number.

We also note that we tried to use the disentangled profiles instead of synthetic ones to measure RVs with the PYTERPOL program written by JN. This worked well for components Aa, and Ab, but not for component B. We suspect that it is so because the shape of the disentangled spectral lines depends on the orbital elements, for which the spectra were disentangled and vice versa. Hence the disentangled spectra partially "remember" the orbital elements, for which they were obtained and if used for the RV measurements, they would give a fine RV curve described by a solution close to these elements. This becomes a problem when one or more orbital elements suffer from a large uncertainty, which was the case for ξ Tau in the mass ratio of orbit 2.

3.4. Comparison of observed and synthetic spectra

JN has developed a Python program PYTERPOL[2], which interpolates in a pre-calculated grid of synthetic spectra to obtain estimates of the radiative properties of the components of multiple systems. For ξ Tau these parameters were the effective temperature $T_{\rm eff}$, gravitational acceleration $\log g$, the projected rotational velocity $v \sin i$, RV, and the relative luminosity $L_{\rm R}$. The parameters of components Aa, Ab, and B were covered by the POLLUX grid (Palacios et al. 2010) and component C was searched for using the AMBRE grid (de Laverny et al. 2012). Solar metallicity was assumed.

The fit was carried out in four spectral regions, but only three relative luminosities were derived, since two of the regions are very close to each other and the luminosities $L_{\rm R}$ are likely almost the same.

The spectral regions were:

1) $\Delta\lambda_1 = [4280, 4495]$ Å,

2) $\Delta\lambda_2 = [4815, 4940]$ Å, and

3) $\Delta\lambda_3 = \{[6330, 6390]\,; [6660, 6695]\}$ Å.

The relative luminosities were assumed to be constant over each spectral region $\Delta\lambda_i$.

Two of regions contain a Balmer line, which constrains the gravitational acceleration of all three components, and a large number of metallic lines, which constrain the temperature, RVs, and the projected rotational velocities. 137 spectra from the Ondřejov Observatory were fitted together, since their normalisation is straightforward (a first order polynomial often suffices to fit the continuum), so that the Balmer lines are not affected by systematics often introduced by the rectification. The uncertainty of the relative flux was estimated from the continuum for each spectrum and set constant for each spectrum.

The bootstrap method was used to obtain optimal set of parameters. 137 spectra were randomly drawn from the pool of 137 Ondřejov spectra (meaning that one or more spectra can be present multiple times within the random sample) and fitted. The initial set of parameters was randomly chosen from intervals[3], which were established from the first trial fits. The initial RVs were estimated from the orbital solution presented in Nemravová et al. (2013) and randomly put slightly off (within 30 km s^{-1} vicinity of the estimate) to secure robustness of the final solution. The procedure was repeated five hundred times and the final set of parameters was estimated from the distribution of results. The shape of the distribution was Gaussian-like and could be described with a mean value and a standard deviation. The results are presented in Table 6.

A comparison of four spectral region with the model is shown in Fig. 4. The reduced χ^2 is lower than one, indicating that we have slightly overestimated the uncertainty of the relative flux of the observed spectra.

3.5. Verification of the results from the previous section via fit of the disentangled spectra by the interpolated synthetic ones

Disentangled spectra corresponding to the solution of Table 5 were fitted with the interpolated synthetic spectra to check on the results from the previous section. Program PYTERPOL was again used.

The following spectral regions were fitted:

$\Delta\lambda 1 = \{[4280, 4400]\,; [4455, 4495]\}$ Å,

$\Delta\lambda 2 = [4765, 4970]$ Å,

$\Delta\lambda 3 = \{[6325, 6395]\,; [6510, 6620]\,; [6655, 6695]\}$Å.

The optimal synthetic spectra correspond to: $T_{\rm eff}^{\rm B} = 14070 \pm 140$ K, $T_{\rm eff}^{\rm Aa} = 10260 \pm 140$ K, $T_{\rm eff}^{\rm Ab} = 10050 \pm 80$ K $\log g^{\rm B} = 3.99 \pm 0.04$, $\log g^{\rm Aa} = 4.06 \pm 0.09$, $\log g^{\rm Ab} = 4.02 \pm 0.04$, $v \sin i^{\rm B} = 253.6 \pm 1.6$ km s^{-1}, $v \sin i^{\rm Aa} = 18.6 \pm 1.2$ km s^{-1}, $v \sin i^{\rm Ab} = 10.20 \pm 0.8$ km s^{-1}, $L_{\rm R}^{\Delta\lambda_1,{\rm B}} = 0.758 \pm 0.008$, $L_{\rm R}^{\Delta\lambda_2,{\rm B}} = 0.711 \pm 0.006$, $L_{\rm R}^{\Delta\lambda_3,{\rm B}} = 0.686 \pm 0.007$, $L_{\rm R}^{\Delta\lambda_1,{\rm Aa}} = 0.168 \pm 0.003$, $L_{\rm R}^{\Delta\lambda_2,{\rm Aa}} = 0.191 \pm 0.005$, $L_{\rm R}^{\Delta\lambda_3,{\rm Aa}} = 0.188 \pm 0.004$, $L_{\rm R}^{\Delta\lambda_1,{\rm Ab}} = 0.150 \pm 0.007$, $L_{\rm R}^{\Delta\lambda_2,{\rm Ab}} = 0.149 \pm 0.003$, $L_{\rm R}^{\Delta\lambda_3,{\rm Ab}} = 0.161 \pm 0.007$, $Z^{\rm B} = Z^{\rm Aa} = Z^{\rm Ab} = 1.0\,{\rm Z}_\odot$. The radial velocity shift of disentangled spectra corresponds to the

[2] Its detailed description with a simple tutorial how to use it is at: https://github.com/chrysante87/pyterpol/wiki

[3] The intervals are following: $T_{\rm eff}^{\rm B} \in [13000, 14500]$ K, $T_{\rm eff}^{\rm Aa} \in [9000, 11500]$ K, $T_{\rm eff}^{\rm Ab} \in [9000, 11500]$ K, $\log g^{\rm B} \in [4.0, 5.0]$, $\log g^{\rm Aa} \in [3.5, 4.5]$, $\log g^{\rm Ab} \in [3.5, 4.5]$, $v \sin i^{\rm B} \in [200, 250]$ km s^{-1}, $v \sin i^{\rm Aa} \in [0, 40]$ km s^{-1}, $v \sin i^{\rm Ab} \in [0, 40]$ km s^{-1}, $L_{\rm R}^{\rm B} \in [0.55, 0.8]$, $L_{\rm R}^{\rm Aa} \in [0.10, 0.25]$, $L_{\rm R}^{\rm Ab} \in [0.10, 0.25]$.

Table 6. Parameters of the fit of the synthetic spectra to 137 observed Ondřejov spectra. The modelled spectral intervals are: $\Delta\lambda1 = [4280, 4495]$Å, $\Delta\lambda2 = [4815, 4940]$Å, $\Delta\lambda3 = \{[6330, 6390]\,; [6660, 6695]\}$Å.

Parameter	Unit	Value		
Component		B	Aa	Ab
$T_{\rm eff}$	(K)	14190±150	10700±160	10480±130
$\log g$	(cgs)	4.527±0.041	4.08±0.12	4.01±0.10
$v \sin i$	(km s^{-1})	229.2±1.7	12.6±2.6	14.3±3.1
$L_{\rm R}^{\Delta\lambda1}$		0.660±0.024	0.179±0.018	0.165±0.022
$L_{\rm R}^{\Delta\lambda2}$		0.688±0.026	0.162±0.024	0.155±0.027
$L_{\rm R}^{\Delta\lambda3}$		0.665±0.036	0.173±0.028	0.161±0.031
$\chi^2_{\rm R}$			0.87	

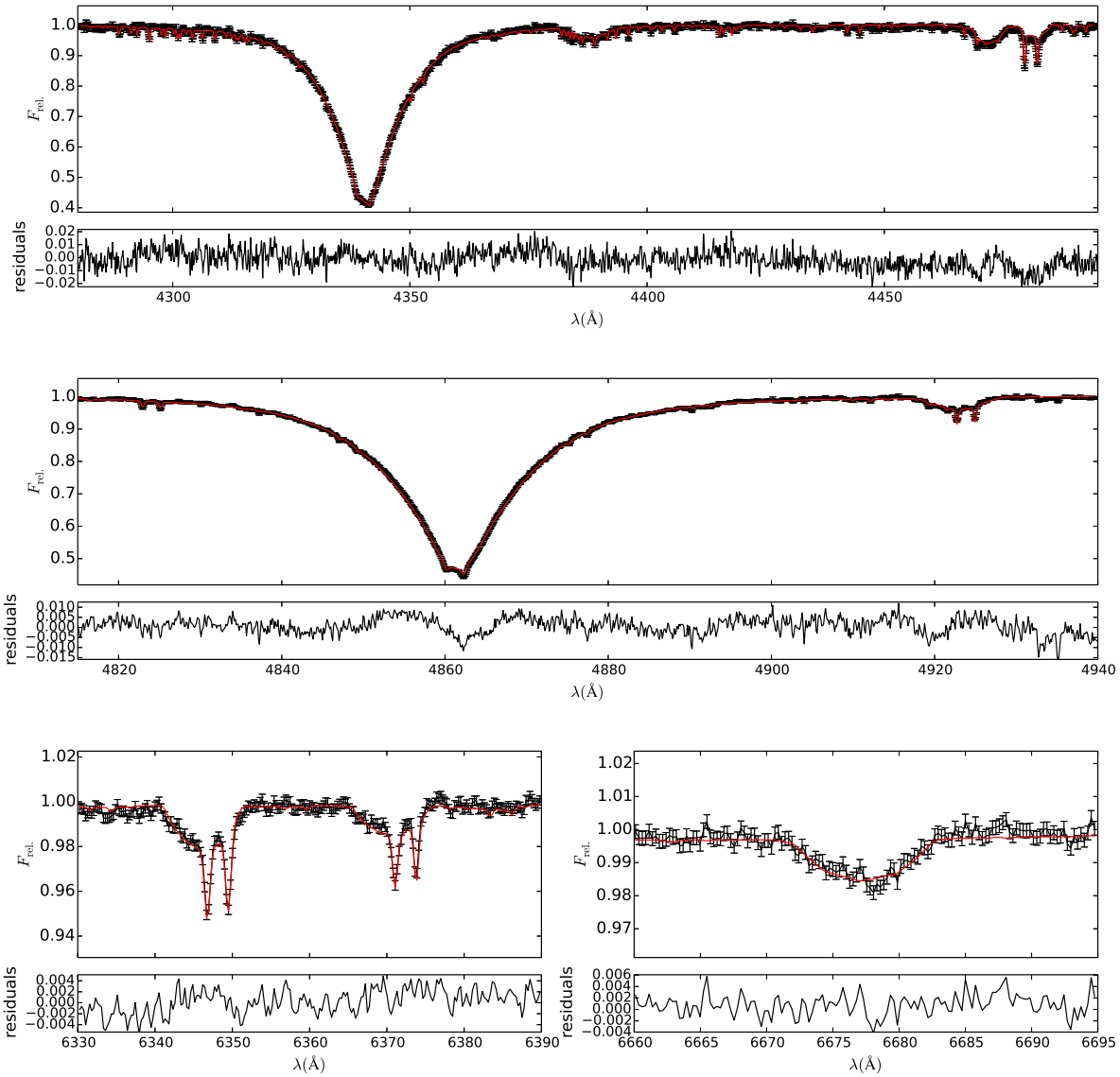

Fig. 4. Example of the fit of the synthetic spectra (red) to three observed ones (black) in spectral regions: 1) $\Delta\lambda1 = [4280, 4495]$ Å (top), 2) $\Delta\lambda2 = [4815, 4940]$ Å (middle), 3) $\Delta\lambda2 = [6330, 6390]$ Å (bottom, left), 4) $\Delta\lambda2 = [6330, 6390]$ Å (bottom, right). The synthetic spectra are given by parameters listed in Table. 6.

systemic velocity and was $\gamma = 8.1 \pm 2.7\,\mathrm{km\ s^{-1}}$. The reduced chi-square is $\chi^{\mathrm{R}} = 31.83$

The optimal parameters were estimated with MCMC simulation and the uncertainties reflect only the statistical part of the uncertainty. The systematic uncertainty — the warp in the continua and the need for its normalisation — cannot be easily quantified and is responsible for the extremely high reduced χ_{R} along with the very low SNR of the disentangled spectra.

This systematic corrupts the estimate of $\log g$ of all components, especially component B, where the warping was the most pronounced, this applies as well to the rotational velocity of component B. The rotational velocity of components Aa, and Ab is affected strongly by the choice of the instrumental broadening, which is very difficult to estimate for disentangled spectra and was set to $0.2\,$Å. The total light is also very likely affected by the re-normalisation, which (necessarily) changes depth of spectral lines (one can see that $L = \sum_{i=1}^{3} L_{\mathrm{R}}^{\Delta\lambda,i} \neq 1$ for all studied bands).

Bearing all this in mind, we state that this result does not contradict, but rather supports the one obtained by fitting of synthetic spectra to observed ones. A comparison of the synthetic spectra corresponding to parameters listed in this section, disentangled spectra and re-normalised disentangled spectra is in Figure A.1.

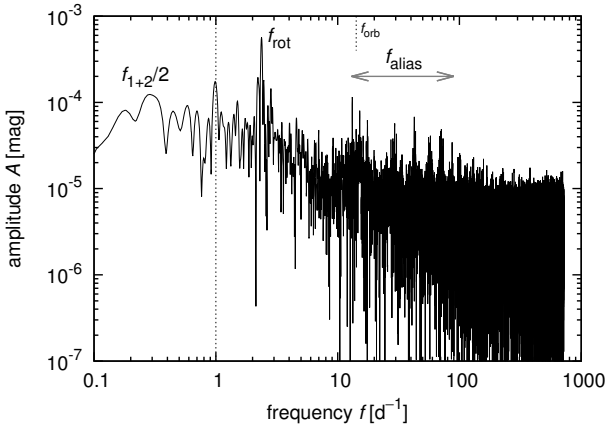

Fig. 5. The Fourier spectrum of the MOST light curve from Figure 6. One can see the basic (rotational) frequency f_{rot} of oscillations, a half of eclipsing binary orbital frequency f_{1+2}, the frequencies of $1\,\mathrm{d}^{-1}$ and $f_{\mathrm{orb}} = 14.2\,\mathrm{d}^{-1}$ are instrumental (i.e. the orbital frequency of the satellite). A number of additional modes, most prominent being $f_{\mathrm{alias}} =$ 13.1912, 15.1734, 17.5385, 28.3896, 42.5825, 56.7745, and 70.9720 seem to be either integer multiples of f_{orb} or its splittings with f_{rot} or $1\,\mathrm{d}^{-1}$. Remaining peaks, e.g. $f = 87.1609\,\mathrm{d}^{-1}$, have relatively low S/N ratios.

4. Photometry

The preliminary analysis published in Nemravová et al. (2013) has shown that the light variations can be attributed to the eclipses of components Aa and Ab of orbit 1. They partially eclipse each other and produce two very narrow and nearly identical minima, which are only $\approx 1\,$mag deep in the Johnson V passband.

In addition to the binary eclipses, our new, very precise MOST satellite observations unveiled persistent low-amplitude rapid cyclic light changes, which are likely to be associated with component B, since they remain to be present during both binary eclipses. The MOST light curve also allows the determination of very accurate radii of components Aa and Ab and the detection of variations of the mean motion of the eclipsing pair. The zoomed parts of both minima of the MOST light curve are shown in Figure 7.

4.1. The period analysis of the light curve

Our first goal in the analysis of the MOST light curve was to unveil the nature of the rapid cyclic low-amplitude changes. Two different methods were used to construct and investigate periodogram of the light curve. The first one is based on the Fourier transform (FT hereafter), and is implemented in the program `PERIOD04` (Lenz & Breger 2004). The second one uses the phase dispersion minimisation technique (PDM) (Stellingwerf 1978) and is implemented in the program `HEC27`[4]. The periodogram of the whole light curve is dominated by the orbital period of the eclipsing binary $P_1 \approx 7.147\,$d. In order to study the rapid low-amplitude oscillation we removed the eclipses (see Figure 6, top).

The periodogram of the rapid oscillations (see Figure 5) shows a basic frequency of $f_0 = 2.38\,\mathrm{d}^{-1}$, most likely due to rotation of component B, the first harmonics of the eclipsing binary orbital frequency $f_1 = 2/P_1 = 0.279\,\mathrm{d}^{-1}$, the frequencies of $f_{\mathrm{d}} = 1.002738\,\mathrm{d}^{-1}$ and $f_{\mathrm{MOSTorbit}} = 14.2\,\mathrm{d}^{-1}$ are instrumental (i.e. the orbital frequency of the satellite). The remaining prominent frequencies $f_{\mathrm{alias}} = \{15.1734, 17.5385, 28.3896, 42.5825, 56.7745, 70.9720\}\,\mathrm{d}^{-1}$. seem to be either integer multiples of f_{orb} or its splittings with f_0 or f_{d}. Remaining peaks (e.g. $f = 87.1609\,\mathrm{d}^{-1}$) have relatively low S/N ratios. We are not aware of any instrumental effect, which would induce oscillations at $f_0 = 2.38\,\mathrm{d}^{-1}$, hence the low-amplitude variations arise from a physical process in ξ Tau.

A closer look at Figure 6 shows that the amplitude of the curve varies. To quantify these changes a harmonic function $f(t) = 1 + C_0 + A_0 \sin[2\pi(t - T_0)f_0 + \phi_0]$ was sequentially fitted to segments of the light curve $\Delta t_1 = P_1/2\,$d wide, and shifted with a step $\Delta t_2 = P_1/20$, where P_1 is the period of the eclipsing binary. The scan revealed that both the basic frequency f_0 and its amplitude A_0 vary on the time-span of two orbital periods of the eclipsing binary (see Figure 6, middle and bottom panels).

4.2. On the nature of quasiperiodic oscillations

The quasiperiodic oscillations clearly visible in MOST light curve — with an approximate period $P_0 \simeq (0.42 \pm 0.01)\,$d and an amplitude $A_0 = (0.00060 \pm 0.00015)\,$mag — exhibit both a frequency (FM) and an amplitude modulation (AM) on the time-span of about two shortest orbital periods P_{1+2} (see Figure 6). We can think of several possibilities regarding their origin: (i) an instrumental effect, (ii) a 5th component and ellipsoidal variations, (iii) rotation with spots, (iv) rotation and pulsations.

The option (i) does not seem very likely thought, because we do not know about any instrumental period of $0.42\,$d (like 1 day, or satellite orbital period 0.07042 d in this case).

A hypothetical 5th component (option ii) orbiting either B star, Aa or Ab star with a period $2P_0$ can induce ellipsoidal variations of the order of A_0, but they should be pretty regular (without large AM, FM) and moreover manifest itself in one of the RV curves too, which is not the case. We do not see any

[4] The program and a short user's guide are available at *http://astro.troja.mff.cuni.cz/ftp/hec/HEC27.*

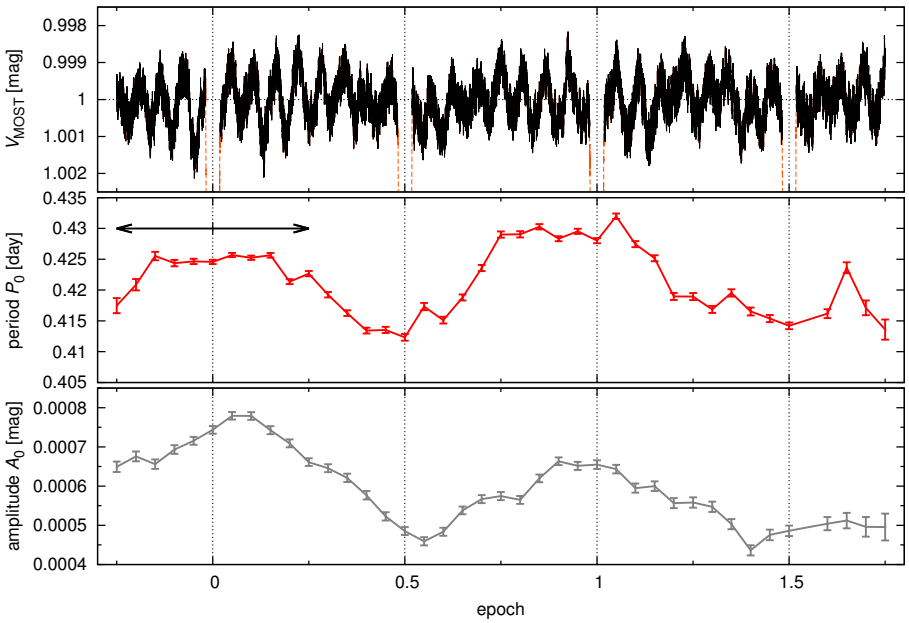

Fig. 6. The normalised light curve as reduced from MOST photometry, but without intervals of primary and secondary eclipses (top panel), together with the corresponding period P_0 (middle) and amplitude A_0 (bottom) of the harmonic function $f(t) = 1 + C_0 + A_0 \sin[2\pi(t - T_0)/P_0 + \phi_0]$, which was sequentially fitted to the light curve, always in limited intervals $\Delta E_1 = 0.5$ of the epoch (indicated by the black double arrow), shifted with a step $\Delta E_2 = 0.05$. We can see that the oscillations exhibit both frequency and amplitude modulations, with periods spanning $P_0 = (0.42 \pm 0.01)$ d and amplitudes $A_0 = (0.00060 \pm 0.00015)$ mag. It seems that the longest P_0 and the largest A_0 are observed at around primary eclipses and *vice versa*.

peak in the Fourier spectrum at $f_0 = 1/P_0 = 2.38\,\mathrm{d}^{-1}$, even though the Nyquist frequency for our spectroscopic dataset is $f_{\rm Ny} = 7.1\,\mathrm{d}^{-1}$. Nevertheless, the coverage and cadence are not uniform at all and the expected amplitude is small ($5\,\mathrm{km\,s}^{-1}$), which makes this particular argument weak. We would also expect to see some frequency modulation due the (classical) Doppler effect, $P'_{\rm obs} = (1 - \frac{v}{c})\gamma P_{\rm src}$, with $v \simeq 2v_{\rm kepl}$. However, for 0.423 d we would only get a change by 0.001 d, which is one order of magnitude smaller than the observed total variation.

Regarding the rotation, the lower limit for its period is the critical rotation, $P_{\rm min} = 2\pi(GM/R^3)^{-1/2}$, and the upper limit is determined by rotational broadening, $P_{\rm max} = 2\pi R/(v \sin i)$ (cf. Table 8). For Aa or Ab stars the admissible range is from about $P_{\rm rot} = 0.180$ d to 3.85 d; for B star 0.325 to 0.634 d. The observed oscillations are within both ranges, so that we cannot distinguish the source component at this point. One can argue that small axial i for Aa, Ab stars is unlikely when their orbital i is large, so that their true $P_{\rm rot} > P_0$. We thus prefer to attribute these oscillations to star B. Additionally, this star is relatively brighter so that it is 'easier' to induce the oscillations of given amplitude A_0.

It seems difficult to distinguish between spots and pulsations (options iii and iv; as in Degroote et al. 2011). Especially for early-type stars, spots are not that common, unless a star is chemically peculiar or magnetically active (Bp), but we have no observations and analyses at disposal which could prove or disprove this for ξ Tau.

Pulsating B stars (like β Cep, SPB) always exhibit a low-frequency signal corresponding to the rotation and then a series of pulsation modes, either pressure (high-frequency) or gravity (low-frequency). The cadence of MOST photometric observations allows us to compute the Fourier spectrum up to $f_{\rm Ny} = 719\,\mathrm{d}^{-1}$, corresponding to 0.00139 d = 2 min (Figure 5). Unfortunately, apart from the basic rotational period, its aliases with the orbital period P_{1+2} of the eclipsing binary, 1-day and $P_{\rm orb}$ instrumental periods, we cannot unambiguously detect any pulsation modes with signal-to-noise ≥ 5, to say nothing about rotational splittings which would be conclusive.

4.3. Eclipse timing variations

The orbital period of the eclipsing binary P_1 =7.14664 d introduces a small but clearly detectable shift $\Delta_{\rm PHASE} \approx 0.0003$ between the two minima recorded with the satellite MOST. The shift disappears if the orbital period and the eccentricity are optimised. The local period and eccentricity, which do not cause the phase shift, are P_1 =7.14466 d, $e_1 \simeq 0.002$. The problem is illustrated in Figure 7, where the comparison of an eccentric model with local value of the orbital period and a global circular model is shown. Even larger phase shift $\Delta p \sim 0.004$ was detected when similar analysis was carried out for all photometric observations.

This led us to investigate the eclipse timing variations (ETVs) in all available photometry, divided into subsets covering time intervals shorter than $P_2/4$ (individual minima are shown in Figures B.1, and B.2). The ETVs are very noisy and the delays themselves have an amplitude $\Delta t_{\rm OBS} \approx 0.025 \pm 0.01$ d, which cannot be explained by LITE ($\Delta t_{\rm LITE} \approx 0.006$ d). Moreover, they seem to vary on a time scale comparable to the orbital period P_2. Hence we suspected the dynamical interaction between orbits 1 and 2 to be the reason for these delays. The first order model of the physical delay (Eq. 8 from Rappaport et al. 2013), which is only a part of the total ETV, arising from dynamical interaction of two orbits in hierarchical triple systems gives an estimate of the amplitude of the effect $\Delta t_{\rm MODEL} \approx 0.02$ d, (i.e. in rough agreement with the detected value). This is another proof of the dynamical interaction in ξ Tau (the first is the apsidal motion reported by Nemravová et al. 2013) and led us to

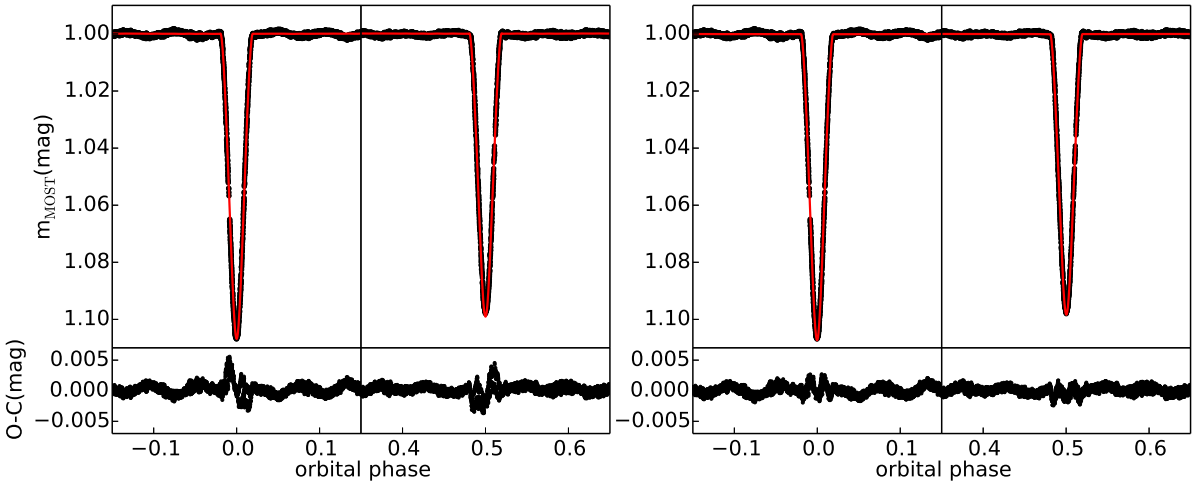

Fig. 7. Fit of the light curve from the satellite MOST. Only the light curve minima and their surroundings are shown. The primary (secondary) minimum is on the left (right) on each panel. The left panel corresponds to the global circular solution $e_1 = 0.0$ and to orbital period $P_1 = 7.14664$ d. The right panel corresponds to a local solution, where small adjustment of the eccentricity and the orbital period was allowed.

development of a N-body model (see section 8.1) and a perturbation theory (see section 9).

4.4. A global orbital model for all light curves

The program PHOEBE 1.0 (Prša & Zwitter 2005, 2006) was used to derive the light-curve solution. The mass ratio q_1 was taken from the analysis of the RVs (see Table 4), because only light curves were modelled and those do not constrain the mass ratio for a detached system. The eccentricity was assumed to be $e_1 = 0.0$ (although sections 8.1 and 9 show that the orbit 1 is slightly eccentric). The value of the semi-major axis a was adjusted after each iteration based on $a_1 \sin i$ given by the fit of the directly measured RVs (see Table 4). The linear limb-darkening law was adopted and the coefficients were interpolated in a precalculated grid distributed along with PHOEBE. The bolometric albedos were taken from Claret (2001) and the gravity brightening coefficients from Claret (1998) for the corresponding temperatures of components of the eclipsing binary. The spin-orbit synchronisation, i.e. the synchronicity ratios $F^{\rm Aa} = F^{\rm Ab} = 1$, were assumed[5]. The primary effective temperature $T_{\rm eff}^{\rm Aa}$ was set to value found through a comparison of synthetic and observed spectra.

The orbital inclination i_1, the surface potential of components $\Omega^{\rm Aa}, \Omega^{\rm Ab}$, and the epoch of the primary minimum $T_{\rm min,1}$, the secondary temperature $T_{\rm eff}^{\rm Aa}$, and the relative luminosity of component B $L^{\rm B}$ in each spectral band were optimised. Initial estimates of these parameters were taken from (Nemravová et al. 2013), initial relative luminosities $L^{\rm B}$ of component B were estimated from the comparison of synthetic and observed profiles (Table 6). The primary luminosities $L^{\rm Ab}$ were adjusted after each iteration.

The fitting was carried out in the Python environment of PHOEBE and the minimum was searched with the differential evolution algorithm (Storn & Price 1997). A large portion of the parameter space was searched[6] The parametric space was densely sampled with models during the fitting (≈ 300000 light curve models were computed). It has shown that the relative luminosity of component B $L^{\rm B}$ is poorly constrained. The high uncertainty of the relative luminosity in the R band is a consequence of a low number of observations, none of them being obtained during the eclipses.

The parameters corresponding to the best-fitting model are listed in Table 7. Note that our model is unable to account for either the rapid light oscillations or the ETVs, therefore we raised the uncertainty of observations from the satellite MOST to deal with the former ($\Delta m_{\rm MOST} = 0.006$ given by the sinusoidal fit). The uncertainties of parameters are estimated as 68 % confidence intervals computed from a scaled χ^2 (scaled to an ideal situation, where the reduced chi-square $\chi^2_{\rm R} = 1$), although in this case the scaling was almost unnecessary, since the reduced chi-square of the best solution is $\chi^2_{\rm R} = 1.16$.

5. Astrometry of orbit 3

We used the existing astrometric positions listed in the WDS catalogue (see Mason et al. 1999, and references therein) to improve the orbital elements of orbit 3 published by Rica Romero (2010). The solution was carried out with the help of the program written by PZ (see Zasche & Wolf 2007, and references therein). The solution is in Table 8 and the orbit is shown in Fig. 8.

6. Spectro-interferometry

In this section we present an orbital analytic model of the ξ Tau system, which we fit to spectro-interferometric observations to estimate orbital elements, radii, and fractional luminosities of ξ Tau.

[5] The radii $R^{\rm Aa}$ and $R^{\rm Ab}$ from Nemravová et al. (2013) and rotational velocities from Table 6 give synchronicity ratios $F^{\rm Aa} = 1.12 \pm 0.26$, and $F^{\rm Ab} = 0.74 \pm 0.20$, the deviations from the corotation are small and probably arise from an incorrect determination of the radii.

[6] Following parametric space was searched: $T_{\rm min,1} \in [56224.68, 56224.78]$ HJD, $i_1 \in [84, 90]$ deg, $\Omega_1 \in [11, 20]$, $\Omega_2 \in [11, 20]$, $T_{\rm eff}^{Ab} \in [10000, 10700]$ K, $L^{\rm B} \in [0.58, 0.78]$. The last interval applies to each studied spectral filter (U, B, V, R, MOST).

Table 7. Parameters of the best-fitting circular orbital model obtained with the program PHOEBE 1.0. All available photometric observations were fitted. Here Ω denotes the Kopal surface potential, and L the relative luminosity in the filter given by the subscript. U, B, V, R denote Johnson filters, MO denotes the broad-band filter at the satellite MOST.

Element	Unit	Value	
		Orbital properties	
P	(d)	7.14664±0.00010	
$T_{\rm p}$	(RJD)	56224.72502±0.00022	
a	($R_\odot$)	25.552±0.097	
q		0.9439[1]	
e		0.0[1]	
i	(deg)	86.76±0.16	
ω	(deg)	90	
		Component properties	
Comp.		Aa	Ab
$T_{\rm eff}$	(K)	10700[1]	10378±22
Ω		15.66±0.53	16.14±0.63
$L_{\rm V}$		0.205±0.013	0.160±0.010
$L_{\rm B}$		0.190±0.019	0.146±0.014
$L_{\rm U}$		0.162±0.016	0.122±0.012
$L_{\rm R}$		0.166±0.063	0.130±0.049
$L_{\rm M}$		0.212±0.014	0.164±0.011
		Passband luminosity of component B	
$L^B_{\rm V}$		0.635±0.023	
$L^B_{\rm B}$		0.664±0.033	
$L^B_{\rm U}$		0.716±0.028	
$L^B_{\rm R}$		0.595±0.089	
$L^B_{\rm MO}$		0.624±0.020	
$\chi^2_{\rm R}$		1.16	

Notes. [1] The parameter was kept fixed.

Table 8. Orbital elements of orbit 3 based on a fit to astrometric measurements published in WDS. The listed parameters are the orbital period P, the periastron epoch $T_{\rm p}$, the eccentricity e, the semimajor axis a, the inclination i, the argument of the periastron ω, the position angle of the nodal line Ω.

Element	Unit	Value
P	(yr)	51.01±0.78
$T_{\rm p}$	(RJD)	54615±251
e		0.5728±0.0028
a	(mas)	441.5±2.4
i	(deg)	25.4±7.7
ω	(deg)	10.6±8.9
Ω	(deg)	106.4±2.2

6.1. A global model for all available spectro-interferometric observations

The calibrated visibilities from VEGA/CHARA were fitted night-by-night with a model consisting of three uniform disks using the tool LitPro (Tallon-Bosc et al. 2008). The observations obtained during each single night were not numerous enough to safely estimate the positions and radii of components Aa, Ab, and B on the celestial sphere[7]

[7] In contrast to it, the NPOI observations are numerous enough to provide good estimates of the relative position of component B and the photocentre of the eclipsing binary for each night. They are presented in Table C.1 along with details on their acquisition – see Appendix C.

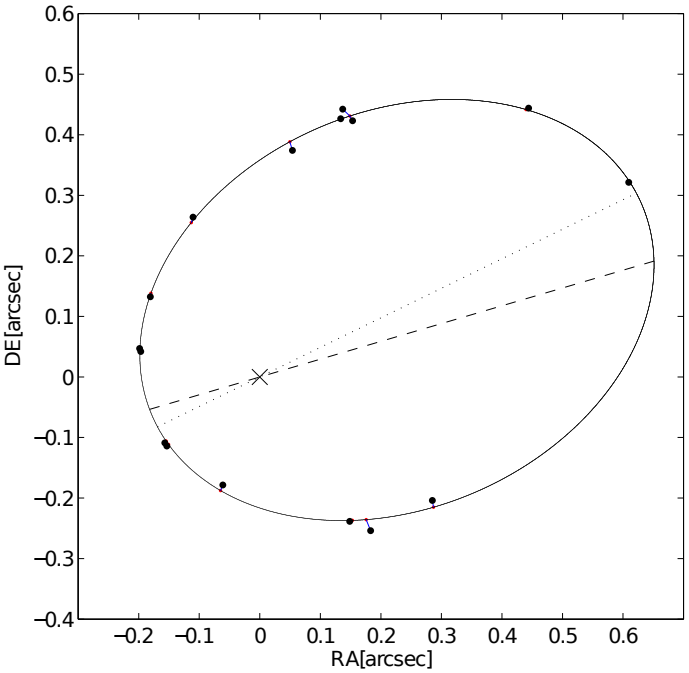

Fig. 8. The speckle-interferometric outer orbit 3 corresponding to solution of Tab. 8.

To circumvent the problem we created a global orbital model, which computes instantaneous positions of components B, Aa, and Ab with following formulæ:

$$\alpha_i(t) = \arctan\left(\tan\left(v_i(t)+\omega_i(t)\right)\cos i_i\right)+\Omega_i, \quad (5)$$

$$\rho_i(t) = a_i\frac{1-e_i^2}{1+e_i\cos v_i(t)}\frac{\cos\left(\omega_i(t)+v_i(t)\right)}{\cos\left(\alpha_i(t)-\Omega_i\right)}, \quad (6)$$

$$x_i = \rho_i\sin\alpha_i, \quad (7)$$

$$y_i = \rho_i\cos\alpha_i, \quad (8)$$

where index i denotes component of a binary, v is the true anomaly, ω the argument of periastron, i the orbital inclination with respect to the celestial sphere, Ω is the position angle of the nodal line, a the angular semimajor axis, e the eccentricity. The position angle α_i is measured from the North-South direction and ρ_i is the angular separation of a component and the centre of mass, (x_i, y_i) is the same in Cartesian coordinates. The instantaneous value of the argument of periastron is given as follows: $\omega(t) = \omega_0 + \dot{\omega}\,(t - T_{\rm p})$, where $T_{\rm p}$ is the reference periastron epoch and ω_0 is the value of the periastron argument at the reference epoch. Instead of computing the semimajor axis for each component of a binary, the semimajor axis a and the mass ratio $q = M_1/M_2$ are used; the semimajor axes of primary and secondary can be computed with following formulæ: $a_1 = aq/\,(1+q)$, $a_2 = a/\,(1+q)$. The periastron argument of the secondary is $\omega_2 = \omega_1 + \pi$.

In our application of Eqs (5) component B is fixed at the beginning of the coordinate system, because the squared visibility is sensitive to relative positions of the stars only, not the system as whole.

Once positions of all three components are known, objects representing each component can be placed at these positions. The uniform disk was chosen, because all three components are detached and so only minor departures from the spherical symmetry can be expected. The visibility for such model can be com-

puted analytically with the following formula:

$$|V_k(u,v)|^2 = \left| \frac{\sum_{j=1}^{N} L_{j,k} \frac{2J_1(\pi\theta_j B/\lambda_k)}{\pi\theta_j B/\lambda_k} e^{-2\pi i(ux_j+vy_j)}}{\sum_{j=1}^{N} L_{j,k}} \right|^2, \quad (9)$$

where index j denotes a component of the triple system, k the spectral band, V the visibility, (u, v) the spatial frequency, L the luminosity fraction, B the length of the baseline, θ the diameter of the uniform disk, λ the effective wavelength (the central wavelength of the spectral band), J_1 the first-order Bessel function, (x_j, y_j) the Cartesian coordinates of a component computed with the Eq. (5), and N the total number of components in the system. The uniform disk diameter θ is also a wavelength-dependent quantity, so a different radius should be derived for each spectral band. Nonetheless the dependency is very weak (order of 10^{-3} for the whole wavelength span of our data).

6.2. An orbital solution for all available V^2

The model given by Eqs. (9), (5) was fitted to calibrated squared visibilities from all three instruments, i.e. CHARA/VEGA, NPOI, MARK III. The optimal set of parameters was searched using the least squares method, i.e. by minimising the following chi-square:

$$\chi^2 = \sum_{k=1}^{N_\mathrm{F}} \sum_{j=1}^{N_\mathrm{O}} \left| \frac{V_k^2(u_j,v_j) - V^2_{\mathrm{MODEL},k}(u_j,v_j)}{\sigma_k(u_j,v_j)} \right|^2, \quad (10)$$

where V^2 is the observed squared visibility, V^2_MODEL the synthetic squared visibility computed with Eq. (9), (u, v) the spatial frequency, σ the standard deviation of the observed squared visibility, N_O the total number of observations of the squared visibility, and the N_F the total number of the spectral bands.

The phase coverage of the inner and the outer orbits is good enough (see Figure 1) to allow fitting of all orbital elements. Our strategy was to keep as many parameters free as possible, since this model is independent of the ones presented in sections 3, and 4. However, some elements are better constrained from the spectroscopy and/or photometry, which are available over much longer time intervals than the spectro-interferometry. Those are especially the orbital periods of the inner orbit P_1 and of the outer orbit P_2, which were kept fixed. Eccentricity of the orbit 1 was set to zero (see Table 4). And epoch of the primary minimum of the eclipsing binary was set as the reference epoch for the orbit 1.

The global minimum of Eq. 10 was searched with the differential evolution algorithm (Storn & Price 1997) and locally optimised with sequential least squares technique (Kraft 1988). The parameters of the best-fitting model are listed in Table 9. Large portion of the parametric space was searched.[8] The initial parametric space was equally sampled with the initial population which consisted of 1500 members. The population evolved until the mean energy of the population (i.e. the mean chi-square divided by its standard deviation and multiplied by the tolerance) was greater than one. The tolerance was set to 10^{-3} and the procedure took from 50 to 100 iterations to finish.

[8] The investigated parametric space is given by following ranges: $\theta_\mathrm{B} \in [0.0, 1.0]$ mas; $L_\mathrm{B} \in [0.4, 0.8]$; $L_\mathrm{Aa} \in [0.1, 0.3]$; $T_{\mathrm{p},2} \in [55600.0, 55620.0]$ RJD; $a_2 \in [13, 18]$ mas; $e_2 \in [0.1, 0.3]$; $i_2 \in [50, 130]$ deg; $\omega_2 \in [0, 180]$ deg; $\Omega_2 \in [0, 360]$ deg; $\dot{\omega}_2 \in [1.5, 4.0]$ deg yr^{-1}; $T_{\mathrm{min},1} \in [56224.0, 56224.5]$ RJD; $a_1 \in [1.0, 3.0]$ mas; $q_1 \in [0.8, 1.2]$; $i_1 \in [80, 100]$ deg; $\Omega_1 \in [0, 360]$ deg;

The final reduced $\chi^\mathrm{R} \approx 6.7$ is caused by: 1) underestimation of the true uncertainty of the V^2 derived with the reduction pipeline, because the high χ^2_R is given mainly by data, which were acquired at low spatial resolution and should be easiest to reduce, and 2) imperfections of the model — we had to accept several simplifications in order to stabilise the fit. Uncertainties of the best-fit parameters were estimated as 68 % confidence intervals from the scaled χ^2_R. Qualitative agreement of the best fitting model shown in Figures C.1 – C.6, that the model qualitatively fits very well the variations of the V^2 (i.e. the curvature of the model data agrees with the curvature of the observed V^2) for all spectro-interferometric data.

Several attempts have shown that we are insensitive to diameters of components Aa and Ab, because we lack enough observations at very long baselines (reaching up to 300 m). If they were set free, the solution then converged to unrealistic values ($\gtrsim 1.0$ mas), so they had to be fixed at values given by the parallax of the system and the light curve solution (see Table 7). Convergence of orbital parameters of orbit 1 was in general slow, because the bulk of observations (practically all NPOI observations) were taken at low spatial resolution, at which this orbit is almost unresolved, and so the solution relied only on observations from VEGA/CHARA.

Our model allows fitting of separate sets of relative luminosities L_R for each passband, because the observations were taken in two (sixteen) passbands for CHARA/VEGA (for NPOI). Unfortunately we did not find it possible to derive a independent set of relative luminosities for each passband. Even if the data were split only into two passbands, the relative luminosities for the short-wavelength one were not well-constrained and often converged to implausible values, because of the low number of observations for the passband. Therefore only one set of relative luminosities was fitted for all observations. It should not be a serious problem, since the relative luminosities do not vary too much in the visible (see Tables 6, 9).

7. Summary of analyses based on simple analytic models

Here the results of individual observational methods are critically compared and the properties of the system are derived.

7.1. Performance of different observational methods

Despite the headline, the individual models, which were used to evaluate different observational methods, were not completely independent, since the results from one method often served as a starting point for another one. In some cases it was mandatory to take a parameter value from another model to stabilise the convergence to a steady solution. In following paragraphs we discuss the outcome of different methods and their accuracy. An overview of all fitted parameters is given in Table 10 obtained through different methods (i.e. more values are given for some parameters). Corresponding properties of the orbits and stars are also listed. Properties of component C and orbit 3 are not listed, since their properties were constrained only by astrometry, presented separately in Table 8.

– **The spectroscopic elements:** Elements (K, e, T_p, P, ω, $\dot{\omega}$) of both orbits are estimated better from the fit of directly measured RVs with an analytic model (see Tab 4, Eqs. 2, 3). The spectral disentangling is more complex and the resulting orbital elements depend on the shape of disentangled profiles (and vice-versa), which come out warped (the degree of the

Table 9. Parameters corresponding to the best-fit of all available interferometric observations with the model defined by Eqs (5), and (9). θ denotes the angular (uniform-disk) diameter.

Elements	Units	Values		
		Component properties		
Component		B	Aa	Ab
θ	(mas)	0.363±0.028	0.252[1,2]	0.231[1,2]
$L_{\rm R}$		0.617±0.010	0.184±0.014	0.199±0.017
		Orbital properties		
Orbit		2		1
$P_{\rm anomal.}$	(d)	145.598[1]		7.14664[1]
$T_{\rm periastr.}$	(RJD)	55610.16±0.43		–
$T_{\rm min.I}$		–		56224.7249[1]
a	(mas)	15.778±0.078		1.711±0.082
e		0.219±0.003		0.0[1]
q		–		0.914±0.095
i	(deg)	86.69±0.10		90.5±3.8
ω	(deg)	10.5±1.2		90.0[1]
Ω	(deg)	328.488±0.073		326.3±1.3
$\dot{\omega}$	(deg yr^{-1})	2.589±0.073		0.0[1]
$\chi^2_{\rm R}$		5.699		

Notes. [1]The parameter was kept fixed. [2]Estimated from the solution from Table 7 and the Hipparcos parallax.

warp is shown by grey line in Fig A.1). The warp is the most pronounced for component B meaning that especially mass ratio q_2 coming from the method cannot be trusted. On the other hand, the thin lines of components Aa and Ab constrain the RVs very well even if the disentangled spectrum is not perfect, and so for the remaining orbital parameters the disentangling provides values, which agree with fit of directly measured RVs.

– **The ephemeris of orbit 1:** The photometric solution presented in Table 7 yields the best ephemeris ($T_{\rm min,1}$, P_1) of orbit 1 especially thanks to high precision observations from the satellite MOST. The solution obtained from the RV curve is in agreement within error bars.
– **The eccentricity of orbit 1:** It is at the order of 10^{-3} as shows the analysis of the light curve from the satellite MOST. The precision of the remaining data is too low for detection of such small eccentricity. The N-body model, which will be presented in section 8.1 accounts for this effect. The oscillations of the eccentricity introduce a "jitter" of relative position of primary and secondary minimum and consequently increase the uncertainty of the light curve solution - especially the Kopal surface potentials $\Omega_{\rm Aa}$, $\Omega_{\rm Ab}$ and consequently the radii.
– **The inclination of orbit 1:** It is determined better from the light curve analysis presented in Table 7, than from the analysis of spectro-interferometric observations, because the majority of the observations were taken at low spatial resolution. Still the values predicted by the two models agree with each other within their uncertainties.
– **The longitude of the ascending node:** The longitude of the ascending node of orbits 1, and 2 has a mirror solution $\Omega_1, 2 = \Omega_1, 2 + 180$ deg withe the same value of the $\chi^2_{\rm R}$, but their relative position is constrained by our data. A solution, where either to Ω_1 or Ω_2 180 deg is added (while the other remains unchanged), has higher $\chi^2_{\rm R} = 6.69$.
– **The relative luminosities:** They were determined from: 1) the light curve solution, 2) the comparison of synthetic and observed spectra, and 3) the interferometric solution.
  - The light curve solution gives the best description of their variations with the wavelength, but the values suffer from large uncertainties, because of correlations between the fitted parameters.
  - The fit of synthetic spectra to observed ones turned to be quite insensitive to relative luminosities, but it is so only because small parts of red spectra, containing only three spectral lines, were fitted. The relative luminosities obtained in the regions around $H\gamma$, and $H\beta$ roughly agree with the values obtained for the B band from the light-curve solution.
  - The bulk of the interferometric observations falls somewhere between the V and R bands. Therefore the relative luminosities detected with the spectro-interferometry are slightly bellow the estimate of the V band value obtained from the light-curve solution.
– **The effective temperatures:** They are given better by the fits of observed spectra to synthetic ones, because the fitted region contain many spectral lines (especially the region $\Delta\lambda = [4280, 4495]$ Å), where the photometry relies on four broad-band filters only. Also Prša & Zwitter (2006) stated that it is not possible to obtain accurate effective temperatures of both components of an eclipsing binary from the light-curve solution, unless the colour-constraining method (described by them) is employed. According to the authors the problem is even more pronounced if the two components are alike. Therefore we fixed the primary temperature and optimised the secondary one only. The result is in agreement with the one obtained from the comparison of observed and synthetic profiles within the respective errors. The spectral types corresponding to these temperatures are B9 for components Aa and Ab, and B5-6 for component B.
– **The semimajor axes and masses:** The physical size of semimajor axes derived from the spectro-interferometry and the Hipparcos parallax (orbits 1, and 2) and those derived from the spectroscopy and photometry (orbit 1) and spectroscopy and spectro-interferometry (orbit 2) agree with each other within their uncertainties. The same applies to masses, which seem to fall within the limits of normal main-sequence (MS hereafter) masses corresponding to the respective spectral types (Harmanec 1988, cf.[[) – $M^{\rm Aa} = 2.25 \pm 0.03 \in$

$[1.71, 2.41]\,\mathrm{M}_\odot$, $M^{\mathrm{Ab}} = 2.13 \pm 0.03 \in [1.71, 2.41]\,\mathrm{M}_\odot$, $M^{\mathrm{B}} = 3.9 \pm 0.4 \in [3.63, 4.6]\,\mathrm{M}_\odot$.

- **Total mass of the system from the astrometry:** Using the Hipparcos parallax and the solution presented in Table 8 one can estimate the total mass of the system $M^{\mathrm{Aa+Ab+B+C}} = 8.7 \pm 1.7\,\mathrm{M}_\odot$. A comparison with the previous paragraph gives a range of plausible mass of the fourth component C $M^{\mathrm{C}} = 0.4 \pm 1.7\mathrm{M}_\odot$.
- **The component radii:** All components seem to have normal radii for their respective spectral type (again checked against Harmanec 1988) — $R^{\mathrm{Aa}} = 1.74 \pm 0.07 \in [1.40, 2.06]\,\mathrm{R}_\odot$, $R^{\mathrm{Ab}} = 1.60 \pm 0.07 \in [1.40, 2.06]\,\mathrm{R}_\odot$, $R^{\mathrm{B}} = 2.5 \pm 0.3 \in [2.13, 2.85]\,\mathrm{R}_\odot$.
- **The deredened colour index B-V:** Although they are derived with high level of uncertainty, because of high uncertainty of the luminosity ratios in different bands and the uncertainty of bolometric magnitudes. We compared the deredened colour indices against tables computed by Flower (1996) —
$T^{\mathrm{B}}_{\mathrm{teff,FLOWER}}(B_0 - V_0)$,
$T^{\mathrm{B}}_{\mathrm{teff,FLOWER}}(-0.137) = 13069\,\mathrm{K}$,
$T^{\mathrm{Aa}}_{\mathrm{teff,FLOWER}}(-0.050) = 10396\,\mathrm{K}$,
$T^{\mathrm{Aa}}_{\mathrm{teff,FLOWER}}(-0.047) = 10335\,\mathrm{K}$,
— which are in a rough agreement with the values found by the comparison of the observed and synthetic spectra. Note that the uncertainty bars of the colour indices are very "generous" and match a wide range of temperatures. Important is that the mean values agree quite well with our predictions.
- **The distance:** The number of applied observational methods allow us to estimate distance of ξ Tau: 1) from the ratio of the physical and angular size of the semimajor axes, 2) from the distance modulus. The former seems to prefer parallax, which is slightly lower than the Hipparcos parallax (but still within error bars), the latter is in agreement with the Hipparcos parallax, but suffers from large uncertainty. The parallax estimated from the ratio of the physical and angular size of semimajor axis of the outer orbit yields the most precise parallax $\pi_{\mathrm{a}_2} = 14.81 \pm 0.89\,\mathrm{mas}$.

7.2. Conclusion of the analytic models

The spectroscopy, the photometry, and the interferometry were studied with traditional analytic models. We found, that results obtained from different methods are consistent with each other, although some of them give better estimates of particular set of parameters than the others. We took advantage of this differential sensitivity and compiled a resulting set of fundamental properties of the system.

During the analyses described in previous sections we noticed two effects pointing at the dynamical interaction in ξ Tau : (i) the advance of the apsidal line of the orbit 2, and (ii) the eclipse timing variations (ETVs) in the system 1. The first effect was explicitly taken into account, because omitting it would cause significant inconsistency between the observations and the model. The latter effect was "almost overlooked", if not for its hint in the very accurate photometric data of the MOST spacecraft. However, the analytic models above give only limited insights into dynamical effects in the four-body system such as ξ Tau. Nonetheless, we find they provide results that are very good, and also needed, starting point for a more sophisticated solution based on approach that includes dynamical evolution in a more complete way. We proceed in two steps.

In Sec. 8 we try to take the bull by horns and develop a numerical model which takes into account gravitational interaction of all stars in the ξ Tau consistently. We use a fully numerical implementation, basically a standard N-body integrator which we extended by subroutines allowing us to model several types of observables relevant for the ξ Tau dataset.

Next, in Sec. 9, we summarize relevant analytic formulæ obtained by methods of perturbation theory, which provide insights into results from the fully numerical approach in Sec. 8. Despite their limitations, we find the analytic formulation of the most important orbital perturbations useful. Not only it allows us understand basic features in the numerical integrations, but its also readily provides the parametric dependencies.

8. N-body model of ξ Tauri with mutual interactions

Given the quadruple nature of ξ Tauri, and its relatively compact packing, it is necessary to proceed with an advanced N-body model which would account for mutual gravitational interactions of *all* four components. To this point, we shall now describe our numerical integrator, a definition of a suitable χ^2 metric, and overall results of our fitting procedure.

8.1. Numerical integrator and χ^2 metric

We use a standard Bulirsch–Stöer N-body numerical integrator from the SWIFT package (Levison & Duncan 1994). Our method is quite general – we can model classical Keplerian orbits, of course, but also non-Keplerian ones (involving N-body interactions). We treat all the stars as point masses only thought; we have no higher-order gravitational terms and no tides in our model.

As explained below, this is a significant improvement of our previous application in Brož et al. (2010), because we can now account not only for the light-time effect but for complete eclipse timing variations (ETVs) of the inner binary, arising from both direct and indirect gravitational perturbations. At the same time, we do not use the simplification of Brož et al. (2010) and we consider all the components separately, because the equivalent gravitational moment:

$$J_2 \simeq \frac{1}{2}\left(\frac{a_1}{r}\right)^2 \frac{m_{\mathrm{Aa}} m_{\mathrm{Ab}}}{(m_{\mathrm{Aa}} + m_{\mathrm{Ab}})^2} \doteq 2 \times 10^{-3} \tag{11}$$

of the inner eclipsing binary Aa+Ab is large at the distance of the component B.

We are forced to use five different coordinate systems: (i) Aa-centric (usually, for a specification of initial conditions and eclipse detection); (ii) barycentric (for the numerical integration itself); (iii) Aa+Ab photocentric (for a comparison with interferometric observations of the component B); (iv) Aa+Ab+B photocentric (dtto for the component C); (v) Jacobian (for computations of hierarchical orbital elements).

Initial conditions at a given epoch T_0 can be specified either in Cartesian coordinates – with x, y in the sky plane and z in the radial direction – or in *osculating* orbital elements. This very choice has a substantial role, because the outcome of the fitting procedure will be generally (slightly) different. The orbital elements can be considered less correlated quantities than Aa-centric Cartesian coordinates.

Table 11. Notation used for various coordinates, velocities and uncertainties, which we use in our N-body model.

x, y, z	Aa-centric coordinates
v_x, v_y, v_z	Aa-centric velocities
$x_{\rm pB}, y_{\rm pB}$	Aa+Ab photocentric sky-plane coordinates (of B component)
$x_{\rm pC}, y_{\rm pC}$	Aa+Ab+B photocentric coordinates (of C component)
$v_{z\rm b}$	barycentric radial velocity
γ	systemic velocity
$v_{\rm rad}$	observed radial velocity
$t_{\rm A}$	mid-epoch of an eclipse of Aa+Ab pair
$\epsilon_{\rm A}$	eclipse duration
$\sigma_{\rm rv}$	uncertainty of the radial velocity
$\sigma_{\rm etv}$	uncertainty of the eclipse mid-epoch timing
$\sigma_{\rm edv}$	uncertainty of the eclipse duration
$\sigma_{\rm sky\,major,\,minor}$	uncertainty of the astrometric position, angular sizes of the uncertainty ellipse
$\phi_{\rm ellipse}$	position angle of the ellipse
$\mathbf{R}(\dots)$	the corresponding 2×2 rotation matrix

We try to account for as much observational data as we can using the following joint metric:[9]

$$\chi^2 = \chi^2_{\rm rv} + \chi^2_{\rm etv} + \chi^2_{\rm edv} + \chi^2_{\rm sky}\,, \tag{12}$$

$$\chi^2_{\rm rv} = \sum_{j=1}^{4}\sum_{i=1}^{N_{{\rm rv}\,j}} \frac{\left(v'_{z{\rm b}\,ji} + \gamma - v_{{\rm rad}\,ji}\right)^2}{\sigma^2_{{\rm rv}\,ji}}\,, \tag{13}$$

$$\chi^2_{\rm etv} = \sum_{i=1}^{N_{\rm etv}} \frac{\left(t'_{{\rm A}i} - t_{{\rm A}i}\right)^2}{\sigma^2_{{\rm etv}\,i}}\,, \tag{14}$$

$$\chi^2_{\rm edv} = \sum_{i=1}^{N_{\rm edv}} \frac{\left(\epsilon'_{{\rm A}i} - \epsilon_{{\rm A}i}\right)^2}{\sigma^2_{{\rm edv}\,i}}\,, \tag{15}$$

$$(\Delta x_{ji}, \Delta y_{ji}) = \mathbf{R}\left(-\phi_{\rm ellipse} - \frac{\pi}{2}\right) \times \begin{pmatrix} x'_{{\rm p}\,ji} - x_{{\rm p}\,ji} \\ y'_{{\rm p}\,ji} - y_{{\rm p}\,ji} \end{pmatrix}\,, \tag{16}$$

$$\chi^2_{\rm sky} = \sum_{j=3}^{4}\sum_{i=1}^{N_{{\rm sky}\,j}} \left\{ \frac{(\Delta x_{ji})^2}{\sigma^2_{{\rm sky\,major}ji}} + \frac{(\Delta y_{ji})^2}{\sigma^2_{{\rm sky\,minor}ji}} \right\}\,, \tag{17}$$

where the notation is briefly described in Table 11. The dashed quantities are the model values linearly interpolated to the exact times t_i of observations. The index j goes over the list of components Aa, Ab, B, C (i.e. $j = 1 = {\rm Aa}, \dots$), while the index i corresponds to the observational data.

Regarding the observational data, we have radial-velocity measurements for the three components (Aa, Ab, B), altogether $N_{\rm rv} = 843$, minima timings for the eclipses in the inner binary (Aa+Ab), $N_{\rm etv} = 35$, and astrometric observations for components B and C, $N_{\rm sky} = 49$. The latter is a subset of measurements from NPOI and WDS, for which it was possible to convert fringe visibilities (averaged over one night) to distance–angle values.[10] The individual uncertainties of the observations used in this section were modified as follows: $\sigma_{\rm rv} \geq 2\,{\rm km\,s^{-1}}$ due to calibration uncertainties, $\sigma_{\rm etv} \geq 0.001\,{\rm d} = 1.5\,{\rm min}$, because the quasi-periodic oscillations visible in the MOST light curve shift minima timings in a random fashion, and $\sigma_{\rm sky} = 3\,{\rm mas}$ (as in Tokovinin et al. 2015) or $5\,{\rm mas}$ if not reported in WDS.

We assumed the nominal distance $d = 64.1\,{\rm pc}$ for ξ Tau. The stellar radii for an eclipse detection were $R^{\rm Aa} = 1.752\,R_\odot$ and $R^{\rm Ab} = 1.542\,R_\odot$, in accord with the photometric inversion. Note that a to-be-expected correlation between $R^{\rm Aa}$, $R^{\rm Ab}$, eclipse depth, eclipse duration and third light contribution is removed to some extent thanks to spectroscopic observations (cf. Table 7).

The synthetic minimum distance Δ' between the components Aa and Ab in the sky plane was determined analytically as the distance of the piece-wise straight line $(x_{\rm Ab}, y_{\rm Ab})$ from the origin in the Aa-centric coordinates, as provided by the numerical integration. The condition for an eclipse is then simply $\Delta' \leq R^{\rm Aa} + R^{\rm Ab}$ and the corresponding time $t'_{\rm A}$ is linearly interpolated from neighbouring points. The eclipse duration is then given by a simple geometry, $\epsilon'_{\rm A} = 2\sqrt{(R^{\rm Aa} + R^{\rm Ab})^2 - \Delta'^2}/\bar{v}$, where $\bar{v}$ denotes the average velocity between the points. We thus straightforwardly account for disappearing eclipses and their durations, but we do not model (possible) eclipse depth variations at this stage.

In order to remove minor systematics in minima timings and eclipse duration, we attempted to suppress quasi-periodic oscillations visible in the MOST light curve by subtracting a function of the following form:

$$\begin{aligned} f(t) \;=\; & C_0 + C_1(t - T_1) \;- \\ & - \left[A_0 + A_1(t - T_1)\right] \sin\left[\frac{2\pi(t - T_1)}{P_0 + P_1(t - T_1)}\right]\,; \end{aligned} \tag{18}$$

its coefficients $(C_0, C_1, T_1, A_0, A_1, P_0, P_1)$ were always determined by a *local* fit in the surroundings of the given minimum. The resulting data are reported in Table 12.

The relative luminosities for photocentre computations were set $L^{\rm Aa} = 0.1362$, $L^{\rm Ab} = 0.1067$, and $L^{\rm B} = 0.7571$ – again, in accord with photometric observations.

There are also mass constraints arising from the spectroscopic classification of ξ Tau components (A9 V, A9 V, B5 V, and F V). We can easily enforce reasonable limits for the component masses with the following artificial term:

$$\chi^2_{\rm mass} = \sum_{j=1}^{4}\left[\left(m_j - \frac{m_{j\,\rm min} + m_{j\,\rm max}}{2}\right)\frac{2}{m_{j\,\rm max} - m_{j\,\rm min}}\right]^{100}\,, \tag{19}$$

where we used $m_{\rm Aa}$ and $m_{\rm Ab} \in (0.9, 3.0)\,M_\odot$, $m_{\rm B} \in (3.5, 3.9)\,M_\odot$, $m_{\rm C} \in (0.9, 2.0)\,M_\odot$ as the limits; the exponent is rather arbitrary.

Table 12. A subset of minima timings $t_{\rm A}$ and eclipse durations $\epsilon_{\rm A}$ determined from MOST light curves, which were corrected for quasi-periodic oscillations by means of Eq. (18), and corresponding uncertainties $\sigma_{\rm etv}$ and $\sigma_{\rm edv}$.

$t_{\rm A}$ JD	$\sigma_{\rm etv}$ day	$\epsilon_{\rm A}$ day	$\sigma_{\rm edv}$ day
2456224.724205	0.0010	0.2656	0.0069
2456228.301662	0.0012	0.2611	0.0035
2456231.868584	0.0010	0.2678	0.0069
2456235.445218	0.0010	0.2573	0.0035

[9] The program used for these computations, including sources and all input data, is available at `http://sirrah.troja.mff.cuni.cz/~mira/xitau/`.

[10] To be crystal clear, in our N-body model we do *not* fit the observed spectra using synthetic ones, individual light curve points, or interferometric fringes. We use higher-level observational data instead which were reduced and derived in previous sections.

The integrator and its *internal* time step was controlled by the parameter $\epsilon_{\rm BS} = 10^{-8}$ (unitless) which ensures a sufficient accuracy. The integration time span was 1000 d forward and 11000 d backward, the output timestep $\Delta t = 0.5\,{\rm d}$ for initial runs. We verified that this sampling is sufficient even for the trajectory with the largest curvature and all necessary interpolations to the times of observations. For the final optimisation we decreased the value further down to $\Delta t = 0.1\,{\rm d}$ to suppress interpolation errors.

We use a standard simplex algorithm (Press et al. 1993) to search for local minima of χ^2. We have 23 of potentially free parameters – masses m_j, coordinates x_j, y_j, z_j, velocities v_{xj}, v_{yj}, v_{zj} in Aa-centric frame – or, alternatively, masses m_j and three sets of orbital elements $a_j, e_j, I_j, \Omega_j, \omega_j, M_j$ in Jacobian coordinates, and the systemic velocity γ. The convergence tolerance for χ^2 was set $\epsilon_{\rm tol} = 10^{-6}$, the maximum number of iterations $10,000$ or as low as 300 for extended surveys of the parameter space. We verified that this low number is sufficient to quickly detect local minima or to exclude their existence.

The initial epoch $T_0 = 2456224.724705$ is very close to the first precise minimum of the MOST light curve. We can thus (almost) fix $x_{\rm Ab} \doteq y_{\rm Ab} \doteq 0$. At the same time, it is possible to (approximately) fix positions $x_{\rm pB}, y_{\rm pB}$ and $x_{\rm pC}, y_{\rm pC}$, derived by interferometry for an epoch close to T_0.

8.2. Resulting best fits

As expected, the 23-dimensional parameter space is vast and full of local minima, even at high χ^2. In order to be safe from headache, we proceeded sequentially and we used: (i) 2012 data only, (ii) 2011–2013, and (iii) all observational data. Next we performed: (iv) a survey of the parameter space (to be sure we did not miss an obvious global minimum), (v) an optimisation of individual orbits (2 and 3), (vi) the mutual inclination of orbit 1 and 2, (vii) we switched from Cartesian coordinates to orbital elements, (viii) we let all parameters to be free. The optimisation means that we started simplex from scratch many times (with different initialization) and let it converge (for a limited number of iterations). Our largest survey consisted of 10^5 simplex runs, 300 steps each, i.e. 3×10^7 models in total, so that we can be pretty sure there is no other "hidden" minimum, at least within the ranges searched so far.[11]

We are aware of *three* mirror solutions (and 2^3 combinations), namely the inner binary can orbit in a retrograde or prograde sense with respect to orbit 2, so that $i_1' = 180^\circ - i_1$. Moreover, its node can be shifted by 180°, $\Omega_1' = \Omega_1 + 180^\circ$. Last but not least, orbit 3 can have the opposite inclination, $i_3' = -i_3$ (we have no direct RV measurements). The total χ^2 values will be generally similar for these mirror configurations, unless…(see below).

Our best fit is presented in Figure 9 and Table 13. Note this is *not* the only fit which seems reasonable, there are many more available in the surroundings. This can be barely seen in Figure 10 where 1-dimensional χ^2 maps exhibit relatively broad minima of the respective parameters. Consequently, if we would use simplex within these ranges, we can surely find a different minimum with slightly larger χ^2 (or even slightly smaller).

We clearly see that the value of $\chi^2 = 2,578$ is still about three times larger than the number of degrees of freedom, $\nu = N_{\rm data} - M_{\rm free} = 931 - 23 = 908$, and formally speaking we should be ready to admit that our model is plainly wrong. Nevertheless, the residua seem to be distributed normally and realistic uncertainties (including some systematics) may be larger than expected. In order to obtain $\chi^2 \simeq \nu$ we would need measurement uncertainties as large as $\sigma_{\rm rv} \simeq 3.5\,{\rm km\,s^{-1}}$, $\sigma_{\rm etv} \simeq 10\,{\rm min}$, $\sigma_{\rm sky} \simeq 1\,{\rm mas}$ (for B component) or $10\,{\rm mas}$ (for C component). We consider these numbers to be quite realistic given the heterogeneous data set we have. We can also imagine additional problems that may contribute to the error budget, e.g. night and night-to-night variations of dispersion relations, unaccounted blending of spectral lines, systematics due to rectification procedure and disentangling, or photocentre motions of the inner binary affecting astrometric positions.

8.3. Differences between traditional and N-body models

Most importantly, orbital elements do change in the course of time; especially $i_1, \Omega_1, \omega_1, \Omega_2, \omega_2$ seem to be critical in the case of ξ Tauri (see Figure 11). While the precession of ω_2 was already accounted for, the remaining terms were not. The precession of nodes Ω_1, Ω_2 about the total angular momentum axis occurs with a $\simeq 19$ year period. In the Laplace plane, it would cause a circulation of Ω's from 0° to 360°, but we can only see an oscillation, at most 3.5° — due to the purely geometrical projection to the plane of sky. There are also inevitable *coupled* oscillations of inclinations, with i_1 ranging from 84.5° to 88.2°. All these rather expected secular effects are discussed in much more detail in Section 9.1.

Additionally, there are short-periodic oscillations not described by the secular theory. While a_1, a_2 only oscillate about constant mean values, there seem to be a 'mid-term' evolution of both e_1, e_2, with amplitudes reaching 0.008 which is btw. larger than the uncertainty of their initial values, e.g. $e_2 = 0.1974^{+0.0009}_{-0.0010}$. In this particular case, it is related to the periastron passage of the component C.

Let us emphasize, it is absolutely necessary to use an N-body model (like ours), otherwise traditional methods assuming *constant* orbital elements (or precessing ω's only) may result in systematic discrepancies or artefacts. If we compare parameters reported in Table 13 to those derived by classical models (Table 10), we see there is a rough agreement between the elements, but their uncertainty intervals do not always overlap. Well, this is probably not surprising, as we compare (osculating) apples and (fixed) oranges.

An outstanding example, how classical methods may fail, is a detailed analysis of MOST lightcurves and the corresponding minima timings from 2012. At first, we thought that the uneven spacing of minima indicates a non-zero eccentricity of the inner orbit, $e_1 \simeq 0.002$. However, this is in a stark contrast with past RV measurements, which constrain forcing of $e_1(t)$ due to perturbations by B component and require $e_1(t = T_0) \to 0$. Looking carefully at Figure 12, we realized that the oscillation of the semimajor axis a_1 has a period 3.76 days, which is an *half* of the synodic period $P_{\rm syn1}$ of orbit 1, in a system which corotates with orbit 2. Moreover, its amplitude slightly decreases, as the component B moves further away. These tiny perturbations are the *real* cause of the observed eclipse timing variations. They also allow us to discard mirror models with $\Omega_1' \neq \Omega_2$ and prefer those with $\Omega_1 \doteq \Omega_2$, because the resulting $\chi^2_{\rm etv} = 390$ vs 150 is

[11] The ranges expressed in Cartesian coordinates were: $z_{\rm Ab} \in (-0.148, -0.088)\,{\rm au}$, $z_{\rm B} \in (-1.47, -0.87)\,{\rm au}$, $z_{\rm C} \in (-8.72, -2.72)\,{\rm au}$, $v_{x{\rm Ab}} \in (-0.092, -0.032)\,{\rm au\,d^{-1}}$, $v_{y{\rm Ab}} \in (0.050, 0.110)\,{\rm au\,d^{-1}}$, $v_{x{\rm B}} \in (-0.078, -0.018)\,{\rm au\,d^{-1}}$, $v_{y{\rm B}} \in (0.042, 0.102)\,{\rm au\,d^{-1}}$, $v_{z{\rm B}} \in (-0.022, 0.038)\,{\rm au\,d^{-1}}$, $v_{x{\rm C}} \in (-0.082, -0.022)\,{\rm au\,d^{-1}}$, $v_{y{\rm C}} \in (0.025, 0.085)\,{\rm au\,d^{-1}}$, and $v_{z{\rm C}} \in (-0.030, 0.030)\,{\rm au\,d^{-1}}$.

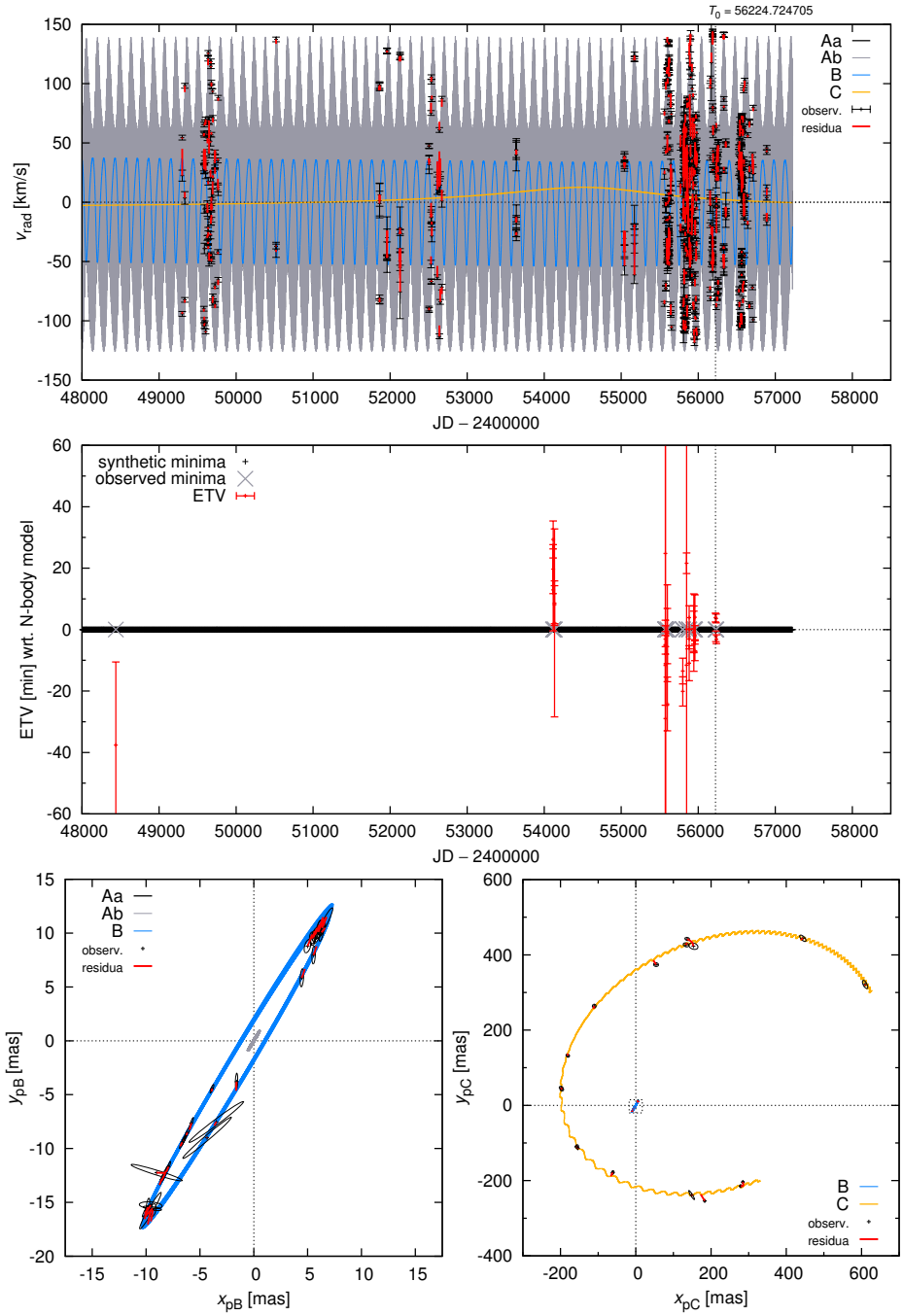

Fig. 9. One of the best-fit solutions for ξ Tau system with our N-body model and using all available observational data. In this case, the resulting total χ^2 is $2,578$, while the number of degrees of freedom $\nu = 908$. Top: Radial velocities $v_{z\mathrm{bAa}}$, $v_{z\mathrm{bAb}}$, $v_{z\mathrm{bB}}$, $v_{z\mathrm{bC}}$ of the individual components; model values are denoted by lines (component Aa is black, actually not clearly visible, Ab grey, B blue, and C orange), observations by black error bars and residuals by thick red lines. Middle: $O-C$ values for both primary and secondary minima timings; model timings are denoted by black points (very densely packed), observations by grey crosses and $O-C$ with its uncertainty by red error bars. Bottom left: Interferometry of component B measured by NPOI; model orbit x_{pB}, y_{pB} with respect to photocentre Aa+Ab (i.e. not wrt. B, as usually) is again denoted by a blue line, observations by black error bars and residuals by thick red lines. Beware the orbit is *not* a single ellipse, but rather a complex trajectory which is quickly precessing and moreover affected by (slight) photocentre motions. Bottom right: Similarly, low-resolution interferometry of the distant component C x_{pC}, y_{pC} with respect to Aa+Ab+B photocentre is denoted by orange line. The component B is relatively luminous what makes the orbit in these photocentric coordinates a bit "jaggy".

significantly different, indeed. Again, the eclipse variations are explained in more detail in Section 9.2.

8.4. A model with closure phases to resolve mirror solutions

The admissible solutions presented in Table 13 are degenerate in a sense that we cannot distinguish among several mirror models (in particular i'_1, i'_3). In order to resolve this degeneracy, hereinafter, we construct an N-body model which accounts for in-

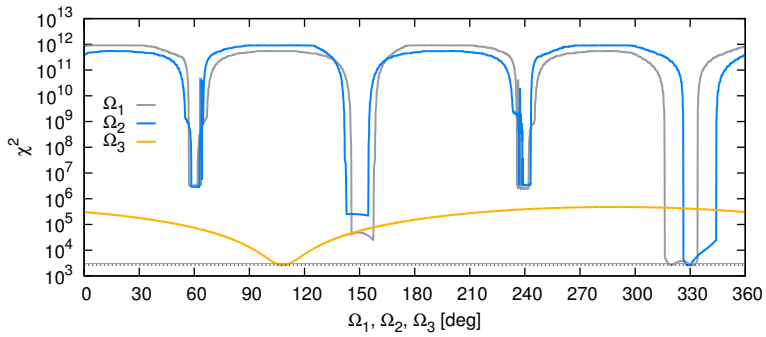

Fig. 10. An example of a 1-dimensional χ^2 mapping used to derive uncertainties of orbital elements for ξ Tau system. The dependencies of χ^2 value on the three nodes $\Omega_1, \Omega_2, \Omega_3$ are shown, while the remaining elements correspond to the best-fit values from Table 13. One can clearly see the preferred solution for $\Omega_1 \doteq 331^\circ$, with $\chi^2 = 2,578$, and a hint of a mirror solution at $\Omega_1 \doteq 151^\circ$. If the latter is optimised separately, one would obtain χ^2 as low as $2,749$. The sudden increase of $\chi^2_{\rm etv}$ corresponds to the disappearance of eclipses of the inner binary which naturally results in extreme $O-C$'s.

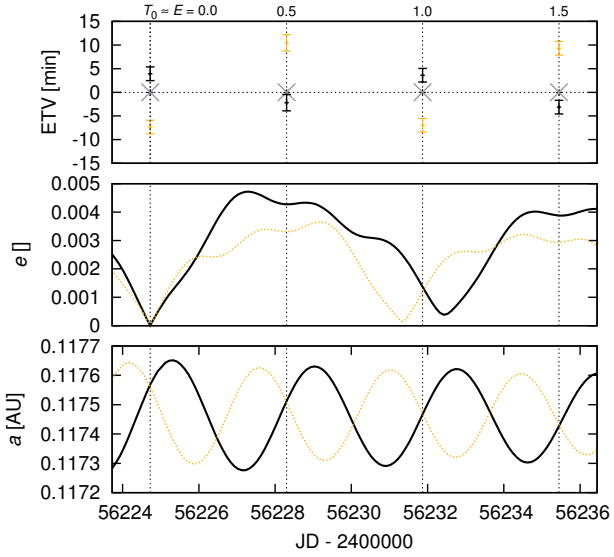

Fig. 12. A comparison of the osculating semimajor axis a_1 (bottom) and eccentricity e_1 evolution (middle) as computed by our N-body model for two mirror solutions with $\Omega_1 \doteq 331^\circ$ (bold solid) and $\Omega'_1 \doteq 151^\circ$ (red dashed). Only a short time span of 12 days is shown, close to the epoch T_0. The corresponding ETVs of minima observed by MOST are also shown at the top. The former solution $\Omega_1 \simeq 331^\circ$ has the corresponding $\chi^2_{\rm etv}$ (for all $N_{\rm etv} = 35$ measurements) significantly lower than the latter, 150 vs 390, so that we consider it as a preferred one.

terferometric visibilities and closure phases. The latter are especially suitable to detect any asymmetries, while the former are necessary to get (symmetric) angular positions and separations right.

Apart from Eqs. (13) to (17) we have a few more:

$$V'(u,v) = \frac{1}{L_{\rm tot}} \sum_{j=1}^{4} L_{ij}\, 2\frac{J_1\left(\pi\theta_j\sqrt{u^2+v^2}\right)}{\pi\theta_j\sqrt{u^2+v^2}}\, \mathrm{e}^{-2\pi\mathrm{i}(ux'_{{\rm a}j}+vy'_{{\rm a}j})}\,, \tag{20}$$

$$L_{ij}(T_{{\rm eff}\,j}, R_j) \doteq \int_{\lambda_i-\Delta\lambda_i/2}^{\lambda_i+\Delta\lambda_i/2} 4\pi R_j^2\, \pi B_\lambda(T_{{\rm eff}\,j})\,\mathrm{d}\lambda\,, \tag{21}$$

$$\chi^2_{\rm vis} = \sum_{i=1}^{N_{\rm vis}} \frac{\left(|V'(u_i,v_i)|^2 - |V|^2_i\right)^2}{\sigma^2_{{\rm vis}\,i}}\,, \tag{22}$$

Table 14. Notation used for additional coordinates and quantities needed in our extended N-body model.

$x_{\rm a}, y_{\rm a}$	Aa-centric coordinates in an angular measure
V	complex visibility, squared visibility is $\|V\|^2$
T_3	complex triple product, closure phase is $\arg T_3$
u, v	projected baselines (expressed in cycles, $\frac{B}{\lambda}$)
$\theta = \frac{2R}{d}$	angular diameter
d	distance to the system
$L, L_{\rm tot}$	component luminosity and the total one
$T_{\rm eff}$	effective temperature
R	stellar radius (uniform-disk)
λ, $\Delta\lambda$	effective wavelength and bandwidth
$B_\lambda(T)$	the Planck function
$\sigma_{\rm vis}$	uncertainty of the squared visibility
$\sigma_{\rm clo}$	uncertainty of the closure phase

$$T'_3 = V'(u_1,v_1)V'(u_2,v_2)V'(-(u_1+u_2),-(v_1+v_2))\,, \tag{23}$$

$$\chi^2_{\rm clo} = \sum_{i=1}^{N_{\rm clo}} \frac{\left(\arg T'_3 - \arg T_{3i}\right)^2}{\sigma^2_{{\rm clo}\,i}}\,, \tag{24}$$

with the notation described in Table 14. The complex visibilities V' and their triple products T'_3 are computed assuming uniform disks for individual components. Relative luminosities L_{ij} at a given effective wavelength λ are computed by a black-body approximation.

This extended model minimizes $\chi^2 = \chi^2_{\rm rv} + \chi^2_{\rm etv} + \chi^2_{\rm edv} + \chi^2_{\rm sky} + \chi^2_{\rm vis} + \chi^2_{\rm clo}$ and has 9 additional free parameters: distance d to ξ Tau, uniform-disk radii R_j, and effective temperatures $T_{{\rm eff}\,j}$ of all the components, even though the contribution of C component is only minor (less than 5 % at the longest wavelength, $\lambda = 860\,$nm).

We use all observational data from MARKIII, NPOI and CHARA/VEGA spectro-interferometers, with $N_{\rm vis} = 15,777$ measurements of the squared visibility $|V|^2$ and $N_{\rm clo} = 4,136$ measurements of the closure phase $\arg T_3$ (from NPOI). The total number of degrees of freedom is thus $\nu = N_{\rm data} - M_{\rm free} = 24,965 - 32 = 24,933$. At the same time we do *not* use astrometric positions ($\chi^2_{\rm sky}$) of B component, because they are not independent; all the information should be contained in $|V|^2$ and $\arg T_3$ measurements.

Initially, we used nominal uncertainties and weights $w_{\rm vis} = 1$, $w_{\rm clo} = 1$, but the resulting $\chi^2_{\rm vis} + \chi^2_{\rm clo}$ value was too large

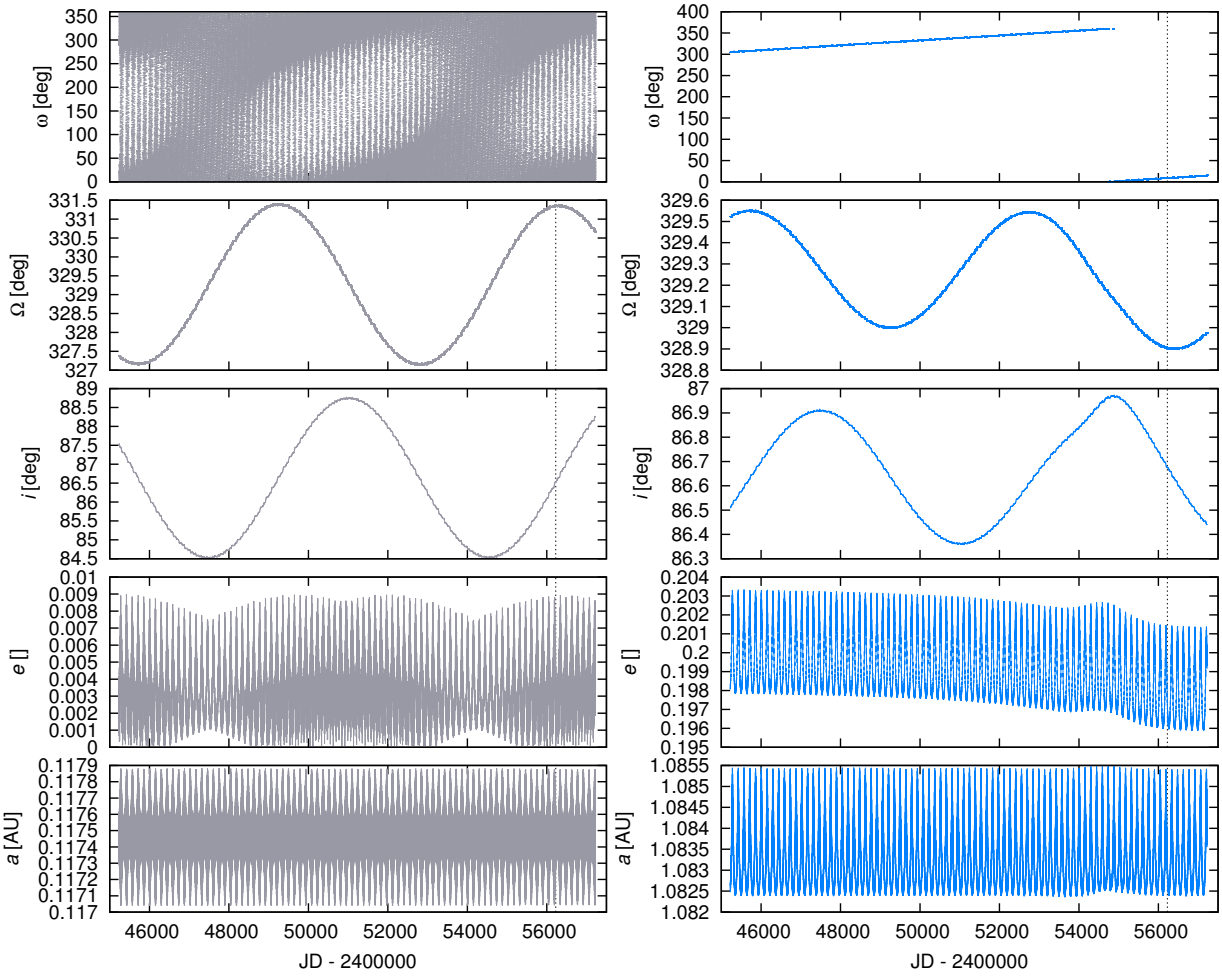

Fig. 11. Time evolution of the osculating orbital elements over a time span -11000 to $+1000$ days from the epoch $T_0 = 2456224.724705$, covered by observations of ξ Tau. Left: The semimajor axis a_1, eccentricity e_1, inclination i_1, longitude of ascending node Ω_1, and the argument of pericentre ω_1 (poorly defined because $e_1 \to 0$) of the inner, eclipsing binary orbit (components Aa and Ab). Right: The same parameters $a_2, e_2, i_2, \Omega_2, \omega_2$ for the orbit 2 (i.e. components (Aa+Ab) and B). All these plots correspond to the simulation with $\chi^2 = 2,578$, presented in Fig. 9. Variations in the inclination i_1 and argument of pericenter ω_2 are of major interest, since they result in observable effects. On the other hand, the distant orbit 3 (not shown here) exhibits only minor variations of its elements. The "bump" in the osculation elements of orbit 2 at JD ≈ 2455500 is related to the passage of C component through its pericenter.

(10^5), even for our best-fit models (cf. Figure 13). The most likely reason is that we did not account properly for all calibration uncertainties. To resolve this issue an internal recalibration would be necessary. Another possibility is that there were quickly changing observational conditions. For example, CHARA/VEGA interferometry from Sep 29th 2011 exhibits unrealistically quick changes of $|V|^2$ at an almost constant baseline $B/\lambda \doteq 1.3$ to 1.4×10^8 cycles (see Figure C.6). In our case, we simply decreased the weight $w_{\rm vis} = 0.1$ in order not to 'slam' other χ^2 contributions. Otherwise, $\chi^2_{\rm vis}$ would completely hinder, e.g., tiny eclipse timing variations.

We focused on a limited set of 7 mirror models, always with one or two modified orbital elements (see Table 15). For each of them, we performed one simplex or simulated annealing[12] run — so that *other* free parameters can adapt themselves to a new situation — and we computed χ^2's, which are reported in the same table. If the final value remains relatively large, it means the model is not compatible with the respective interferometric data.

[12] with the initial "temperature" 100 000 "kelvin", schedule $T^{i+1} = 0.99T^i$ and 100 iterations at given T^i

Clearly, we are sufficiently sensitive to resolve Ω_2 and i_2, i.e. the longitude of the ascending node and the inclination of B component (see Figure 14). but not directly to Ω_1, i_1, or i_3 elements. Consequently, we can discard Ω_2', i_2' and prefer $\Omega_2 \doteq 331°$, $i_2 \doteq 86°$ solution on the basis of the closure phase measurements alone.

Moreover, because our N-body model is all the time constrained by RV, ETV, ETD and astrometric data, which prevent a convergence to unrealistic values of all the parameters, we can spot (in Table 15) that the squared visibility measurements are not compatible with Ω_1' and i_1', so they are discarded too and $\Omega_1 \doteq 329°$, $i_1 \doteq 86°$ solution is preferred.

Finally, as already demonstrated in Section 8.3, the N-body dynamics and ETV measurements allow us to safely discard any $\Omega_1 \neq \Omega_2$, so we definitely prefer $\Omega_1 = 329°$. The only remaining ambiguity is thus the inclination i_3 vs i_3'. To conclude this section, a combination of more-or-less orthogonal measurements (RV, ETV, ETD, $|V|^2$, $\arg T_3$) leads to interesting and solid results, which is *not* surprising at all.

Let us also comment on the fact that even this kind of model may be actually insufficient. There exist other physical effects we did not account for, e.g. tidal interactions of

Table 15. Summary of $\chi^2_{\rm vis}$ and $\chi^2_{\rm clo}$ values for squared visibility $|V|^2$ and closure phase $\arg T_3$ measurements. Only a limited set of mirror models is shown — with respect to the nominal one ($\Omega_1 \doteq 331°$, $\Omega_2 \doteq 329°$, $\Omega_3 \doteq 110°$, $i_1 \doteq 86°$, $i_2 \doteq 86°$, $i_3 \doteq -24°$). The closure phase measurements allow us to discard some of them, namely those with Ω'_2 and i'_2, because the 3-σ level corresponds to a relative increase by 1.054, i.e. $\chi^2_{\rm clo} \simeq 19,316$. Moreover, the $|V|^2$ measurements do not favour Ω'_1 and i'_1 (3σ is at 1.030, $\chi^2_{\rm vis} \simeq 120,913$). The symbol $\times$ in the last column indicates we discard this possibility.

Orbital elements	$\chi^2_{\rm vis}$	$\chi^2_{\rm clo}$	Note
nominal	117,449	18,323	
$\Omega'_1 = \Omega_1 + 180° \doteq 151°$	**134,968**	18,875	$\times$
$\Omega'_2 = \Omega_2 + 180° \doteq 149°$	308,122	**82,087**	$\times$
(Ω'_1, Ω'_2)	307,970	**80,255**	$\times$
$i'_1 = 180° - i_1 \doteq 94°$	**135,991**	18,161	$\times$
$i'_2 = 180° - i_2 \doteq 94°$	514,960	**31,073**	$\times$
$i'_3 = -i_3 \doteq 24°$	117,218	18,193	
(i'_1, i'_2)	623,137	**38,317**	$\times$

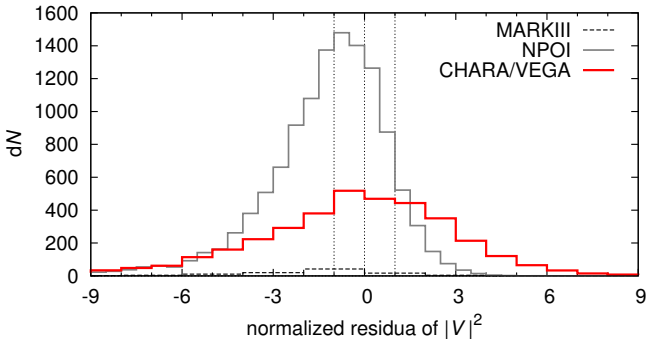

Fig. 13. Distributions of normalized residua $(|V'|^2 - |V|^2_i)/\sigma_{{\rm vis}\,i}$ of the squared visibility for our 'best-fit' model with $\chi^2_{\rm vis} = 121,763$, while the total number of measurements is $N_{\rm vis} = 15,777$. Three separate datasets are shown, corresponding to MARKIII, NPOI and CHARA/VEGA interferometers. Note the distributions are not perfectly symmetric about zero and the one for CHARA/VEGA data is significantly wider, probably due to unaccounted calibration uncertainties.

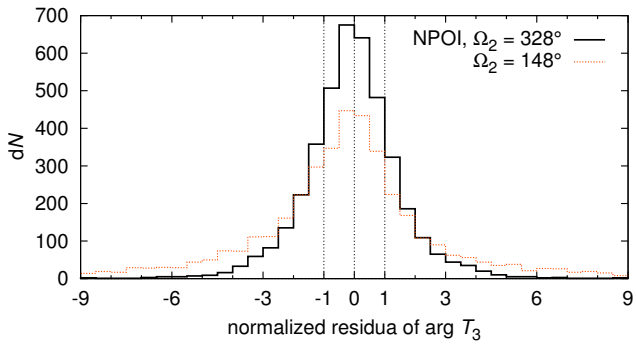

Fig. 14. Distributions of normalized residua $(\arg T'_3 - \arg T_{3i})/\sigma_{{\rm clo}\,i}$ of the closure phase for two 'best-fit' models with different values of the longitude of the ascending node $\Omega_2 = 329°$ and $\Omega'_2 = 149°$. Both distributions seem symmetric about origin, indicating there are no serious systematics in $\arg T_3$ measurements. However, the former distribution is substantially narrower that the latter, so that the mirror solution Ω'_2 can be discarded.

non-spherical stars, spin–orbital coupling, various magneto-hydrodynamic phenomena, or pulsations of (all) components. Their importance for the dynamics of ξ Tau is yet to be assessed.

9. Dynamical evolution of the 1-2 subsystem

Osculating orbital elements shown in Fig. 11 exhibit many variations over different timescales, from the very short period of the the inner eclipsing binary, to the intermediate period of the orbital motion of the star B with respect to the system A, up to very long periods of tens to hundreds of years. Could we understand some of these terms, including their amplitude and determine their parametric dependence on stellar masses and periods of the orbits 1 and 2? To do so we need to turn to the perturbation theory. In this section, we neglect dynamical effects of the distance star C and focus on the triple system A+B.

The hierarchy of the ξ Tau system implies a preferential choice of Jacobi coordinates for description of its dynamics, in which (i) the first $\mathbf{r}$ is the relative position of Ab with respect to Aa, and (ii) the second $\mathbf{R}$ is the relative position of component B with respect to the barycentre of the orbit 1. The conjugate momenta involve reduced masses $m'_1 = m^{\rm Aa}m^{\rm Ab}/M^{\rm A}$ and $m'_2 = m^{\rm B}M^{\rm A}/M^{\rm AB}$ of the 1 and 2 orbits, with $M_1 = m^{\rm Aa}+m^{\rm Ab}$ and $M_2 = M^{\rm A} + m^{\rm B}$. At the zero order of approximation, both systems evolve on Keplerian orbits, but their interaction introduces a perturbation that makes $\mathbf{r}$ and $\mathbf{R}$ to follow more complicated trajectories as described by numerical integration in Sec. 8. The elliptical approximation may be only applicable to a certain interval of time. The latter becomes short especially for compact systems, when for instance the third component is not too distant to the inner binary; ξ Tau is a good representative of this class.

In the world of the perturbation theory, both A and B system are represented using a set of osculating orbital elements that evolve in time due to their mutual interaction. From a plethora of perturbations described in this way, we recall two results relevant for the observed features of the ξ Tau system. We first describe the secular effects, which for this compact system are conveniently short in time to be detected, and then some of the long- and short-period eclipse time variations in the system A.

9.1. Secular effects

Define Delaunay momenta $L_1 = m'_1\sqrt{GM_1a_1} = m'_1n_1a_1^2$ and $L_1 = m'_2\sqrt{GM_2a_2} = m'_2n_2a_2^2$ of the A and B orbits (e.g., Harrington 1968, 1969; Soderhjelm 1975; Breiter & Vokrouhlický 2015). Here n_1 and n_2 are the mean motion values of the orbits 1 and 2, both related to the semimajor axes a_1 and a_2 via the third Kepler law: $n_1^2a_1^3 = GM_1$ and $n_2^2a_2^3 = GM_2$ (G is the gravitational constant). In a secular approximation, when longitude in orbit for both 1 and 2 orbits is removed from the interaction (e.g., Harrington 1969; Breiter & Vokrouhlický 2015), the semimajor axes a_1 and a_2 are constant.

Dynamics of the A+B system may be, in principle, studied in an arbitrary reference frame. However, its description becomes very simple in a preferred, often called Laplacian, frame. The z-axis of this frame is oriented along the conserved total orbital angular momentum of the system. In order to distinguish osculating orbital elements in the observer-oriented frame, used above, we shall denote the elements in the Laplacian frame with tilde. For instance the orbital inclinations for orbits 1 and 2 will be denoted $\tilde{\imath}_1$ and $\tilde{\imath}_2$, and the corresponding longitudes of node $\tilde{\Omega}_1$ and $\tilde{\Omega}_2$.

The secular evolution of the triple system is particularly simple when (i) the eccentricity e_1 of the inner orbit is negligible, (ii)

the mutual angle[13] $\tilde{J}$ of the 1 and 2 orbital planes small, and (iii) the system is wide-enough, such that on the timescale of interest only the quadrupole interaction of the inner and outer orbits is relevant. Luckily (i)-(iii) currently apply to the ξ Tau system.[14] Then, $e_1 = 0$ is a stable solution, and e_2 and $\tilde{J}$ are constant in time. In fact, referring the orbital elements to the invariable plane, normal to the total angular momentum of the system, orbital inclinations $\tilde{\imath}_1$ and $\tilde{\imath}_2$ of orbits 1 and 2 are constant, and both orbital planes uniformly precess in the inertial space about the total angular momentum direction. Their nodes $\tilde{\Omega}_1 = \tilde{\Omega}$ and $\tilde{\Omega}_2 = \tilde{\Omega} + \pi$ linearly advance with a rate (e.g., Soderhjelm 1975; Breiter & Vokrouhlický 2015)

$$\frac{\dot{\tilde{\Omega}}}{n_2} \simeq \frac{3}{4\eta_2^3}\frac{m^{\rm B}}{M_2}\frac{n_2}{n_1}\cos\tilde{J}\sqrt{1+\gamma^2+2\gamma\cos\tilde{J}}, \tag{25}$$

where $\gamma = L_1/(L_2\eta_2)$ is the ratio of the angular momenta of the two orbits ($\eta_2 = \sqrt{1-e_2^2}$). In triple systems usually the outer orbit has a dominant share on the total angular momentum of the system, thus $\gamma < 1$. Indeed, for ξ Tau we have approximately $\gamma \simeq 0.132$. Unless precisely coplanar, the main effect of the orbital-plane precession is in periodic changes of inclinations i_1 and i_2 in the observer's system. These variations directly affect magnitude depths of the eclipses, or eventually could make the system non-eclipsing for certain period of time.

Apart from the steady precession of the orbital planes, the second secular effect in the given setup consists in precession of the pericentre of the outer orbit. Denoting its longitude $\tilde{\varpi}_2$, we have

$$\frac{\dot{\tilde{\varpi}}_2}{n_2} \simeq \frac{3}{8\eta_2^3}\frac{m^{\rm B}}{M_2}\frac{n_2}{n_1}\gamma\left(3\cos^2\tilde{J}-1 - \frac{\gamma\,\sin\tilde{J}\sin 2\tilde{J}}{1+\gamma\cos\tilde{J}+\sqrt{1+\gamma^2+2\gamma\cos\tilde{J}}}\right), \tag{26}$$

Comparing (25) and (26), we note that the pericenter precession frequency of the outer orbit is slower by a factor $\simeq \gamma$ than the nodal frequency (assuming $\tilde{J}$ sufficiently small). Thus nodes, and inclinations observer system, typically oscillate with shorter period than the period of pericenter revolution of the outer-orbit.

9.2. Long- and short-period eclipse variations

Mutual interaction of the orbits results also in a palette of periodic perturbations. So far the long-period effects, namely those having a period P_2 of the outer orbit B, have been extensively studied (e.g., Soderhjelm 1975, 1982; Borkovits et al. 2003, 2011, 2015). Out of them we shall focus on what is known eclipse time variations (ETV), namely periodic advances and delays $\delta t_{\rm LP}$ in epochs of eclipse of the inner system 1 due to the variations in its mean motion n_1 caused by the third component. Assuming for simplicity coplanar orbits $\tilde{J} = 0°$, one obtains (e.g., Soderhjelm 1975; Borkovits et al. 2011, 2015; Rappaport et al. 2013, which also contain the $\propto \tilde{J}^2$ corrections)

$$n_1\delta t_{\rm LP} \simeq \frac{m^{\rm B}}{M_2}\frac{n_2}{n_1}W\left(e_2,\ell_2\right), \tag{27}$$

with

$$W\left(e_2,\ell_2\right) = f_2 - \ell_2 + e_2\sin f_2, \tag{28}$$

where f_2 and ℓ_2 are the true and mean anomalies of the orbit 2. For small eccentricity e_2 we have $W \simeq 3e_2\sin\ell_2$. Obviously, the principal component of ETV in (27) become zero for circular outer orbit, because it has to do with variations of n_1 triggered by variations in the distance R to the third component.

In course of this work, we noted that also the dominant short-period effect may be of interest (those having period of the inner orbit 1), provided high-quality eclipse data are collected. Using methods of the first-order perturbation theory we found that the leading short-period term reads

$$n_1\delta t_{\rm SP} \simeq \frac{21}{8}\frac{m^{\rm B}}{M_2}\left(\frac{n_2}{n_1}\right)^2\left(\frac{a_2}{R}\right)^3\sin 2\left(\lambda_1-\tilde{F}_2\right), \tag{29}$$

where R is distance of the component B to the barycentre of the inner binary system, and $\tilde{F}_2 = \tilde{\varpi}_2 + f_2$ is its true longitude in orbit. Note the term has a period equal to half-synodic period of the inner system A in a reference frame corotating with motion of the outer star B. This is because it has to do with variations of n_1 triggered by variations in the three-body potential energy for varying geometry of the orbit with respect to the B component. For that reason, this effect is not primarily dependent of the eccentricity e_2. Its magnitude is smaller by a factor 0.4 in the periastron and by 0.1 in the apoastron of the orbit 2. Nevertheless, the effect is not entirely negligible and we found that it contributes to the observed eclipse shift in the MOST data (see Fig. 12).

9.3. Comparison of the secular theory with the results of the analytic and numerical models

Here we confront the apsidal motion detected with both analytic and numerical methods and additional secular and periodical variations of orbital elements predicted by the numerical model presented in Sec. 8.1.

- **The apsidal motion of orbit 2:** First, we use results of the analytic theory above. Using nominal orbital parameters from Table 10 we obtain $\tilde{J} = 6.92 \pm 0.63$ deg, and consequently $\dot{\omega}_2 = 2.135 \pm 0.077$ deg yr^{-1}. Note that $\dot{\omega}_2$ may be directly obtained from Eq. (26), because the nodal longitude Ω_2 in the observer frame oscillates without any secular drift. This is about a third lower than the value detected with the analytic radial velocity curve model (see Table 4), but in an excellent agreement with the N-body model, whose prediction is $\dot{\omega}_2 = 2.11$ deg yr^{-1}.
- **The nodal motion of orbits 1 and 2:** Inserting nominal parameters from the Table 10 provides the mean nodal drift $\dot{\tilde{\Omega}} = 18.83 \pm 0.92$ deg yr^{-1}(Eq. 25), which is again in excellent agreement with results of the N-body model; note the periods of the nodal oscillations are effectively $\simeq 19.43$ deg yr^{-1}for the orbit of component A (Ω_1) and $\simeq 19.81$ deg yr^{-1} for the orbit B (Ω_2). The values not exactly the same, likely

[13] The mutual angle $\tilde{J} = \tilde{\imath}_1 + \tilde{\imath}_2$ may be determined by the orbital elements in the observer frame using:

$$\cos\tilde{J} = \cos i_2\cos i_1 - \sin i_2\sin i_1\cos\left(\Omega_1-\Omega_2\right) .$$

[14] As to (iii), note that the octupole interaction is very small because of nearly equal masses in the system 1, i.e., $m^{\rm Aa} \simeq m^{\rm Ab}$. The next secular contribution would arise from the non-linear quadrupole effect (e.g., Breiter & Vokrouhlický 2015), which is small on a timescale of a couple of decades.

due to interaction with the component C, which was not included in the perturbation theory. As mentioned above, there is a hint of the shallower depth of Hvar photometric observations from early 2007 when our model predicts larger value of the inclination i_1. However, to pin down the inclination variations we need more accurate photometic observations in the future.

– **Eclipse-timing variations – orbit 1:** The Eqs. (27, 28, 29) provides amplitudes of the ETVs (assuming that the component B is at the periastron) of orbit 1 $\delta t_{\mathrm{ETV,long}} = 0.0162 \pm 0.0010$ d, $\delta t_{\mathrm{ETV,short}} = 0.0068 \pm 0.0004$ d. Their sum is in a nice agreement with the detected amplitude of ETVs ($\delta t_{\mathrm{ETV,OBS}} = 0.025 \pm 0.010$ d). Note also, that the two primary eclipse minima in the MOST data were found to be phase-shifted by $\simeq 0.0003$ in Sec. 4.3. This is about 0.1° in longitude in orbit of the inner system A. Combining results in Eqs. (27, 28, 29), and taking into account $\ell_2 \simeq 86^\circ$ and $\lambda_1 \simeq F_2$ from Table 13, we obtain a very good agreement with the observed shift.

10. Motivations for future observations of ξ Tauri

First, it seems desirable to continue the observations of the times of minima and, more importantly, eclipse duration and depth. At an epoch after approximately RJD 59405.0, i.e., summer 2021, one would expect either persisting, or disappearing eclipses of the inner pair Aa+Ab for different mirror solutions. Consequently, this is a direct and independent test of our analysis of closure phase measurements in Sec. 8.4. Note that the nominal solution shown in Fig. 11 exhibits too small variations of i_1, such that the eclipsing binary would be eclipsing all the time.

Nevertheless, even the nominal solution predicts nearly 4° full amplitude of variation in i_1 and one should expect fairly well observable effects. We are suggesting, for instance, a space-born observation of a similar quality to that of MOST, obtained at the turn of 2016 and 2017, when the predicted i_1 value would be maximum (about 88.2°). The change in eclipse depth, as compared to the MOST data, should be about 0.05 magnitude, very easily to be detected. Such a single observation would further constrain parameters of ξ Tauri with an exceptional accuracy.

Second, in spite of all difficulties, it would be of a great help if the line spectra of the faint component C, separated by 200 to 600 mas from the triple Aa+Ab+B, were obtained and the corresponding radial velocity measured. This would also allow us to distinguish between the remaining two mirror orbital solutions for the motion of this component.

Precise and uninterrupted space-based photometry on a longer time-span would be useful to unambiguously resolve oscillation modes and splittings. Given the high rotation frequency $f_{\mathrm{rot}} = 2.38\,\mathrm{d}^{-1} \doteq 27.5\,\mu$Hz, it should not be that difficult (the minimum time-span $\Delta t \simeq 1/f_{\mathrm{rot}}$), but currently aliases with instrumental frequencies seem to limit the S/N in the Fourier spectrum. As an alternative, series of high-resolution high-S/N spectra would be needed to detect the oscillation modes independently, as the traveling sub-features in the line profiles of component B broadened by a relatively high rotation.

11. Conclusion

We have conducted an in-depth study of a quadruple stellar system ξ Tau, starting from simple analytic models for different kinds of observations (see section 3-7), and ending up with a complex N-body model, which combines astrometric, photometric, spectroscopic, and spectro-photometric observations to a certain degree (see section 8). We were able to put tight constraints on three components of ξ Tau, and they will provide an excellent test case for models of stellar evolution, while the full description of the geometry of the hierarchy a test of the binary formation.

The analytic models allowed us to estimate properties of components Aa, Ab and B, which show a great deal of consistency (see critical summary of the analytic models in section 7) and mean orbital elements of orbits 1, 2, and 3 using different methods – again consistent with each other, but provided limited-to-no insight into the dynamic evolution of orbits of ξ Tau.

This discrepancy was fixed with the N-body model, which properly accounts for the dynamic interaction within the system and is able to fit RVs, ETVs, and astrometric positions simultaneously. It provided a set of osculating elements and component masses, whose evolution fits the observables (see Table 11), insight into long-term and short-term evolution of osculating elements (see Figure 11) and also resolved between prograde and retrograde solution (between orbits 1 and 2) solely from ETVs. The result also gives credibility to previous analyses, because it did not drift far away from their outcome.

The perturbation theory shows that the most pronounced secular evolution of elements — the advance of the apsidal line of orbit 2, and the harmonic variation of the inclination $i_{1,2}$, and the longitude of the ascending node $\Omega_{1,2}$ — are both explained by a quadrupole interaction between orbits 1 and 2. The same applies to predicted size of ETVs, which are in good agreement with observations.

The next step in the model development is to adapt it for additional observables — especially the light curve and the interferometric observables (i.e. the fringe visibility and the closure phase). Such model has been developed by other group (e.g. PHOEBE 2.0; Prša et al. 2013; Conroy et al. 2013) and ξ Tau and our analysis may prove a test for their tool.

Acknowledgements. The research of JN, PH, MW, and PZ was supported by the grants P209/10/0715 and GA15-02112S of the Czech Science Foundation. The research of JN and PH was supported by the grant no. 678212 of the Grant Agency of the Charles University. We acknowledge the use of the electronic database from the CDS, Strasbourg and electronic bibliography maintained by the NASA/ADS system. The Navy Prototype Optical Interferometer is a joint project of the Naval Research Laboratory and the US Naval Observatory, in cooperation with Lowell Observatory and is funded by the Office of Naval Research and the Oceanographer of the Navy. The authors thank Jim Benson and the NPOI observational support staff whose efforts made this project possible. This research has made use of the SIMBAD astronomical literature database, operated at CDS, Strasbourg, France. This publication is supported as a project of the Nordrhein-Westfälische Akademie der Wissenschaften und der Künste in the framework of the academy programme by the Federal Republic of Germany and the state Nordrhein-Westfalen.

References

Aller, L. H., Appenzeller, I., Baschek, B., et al., eds. 1982, Landolt-Börnstein: Numerical Data and Functional Relationships in Science and Technology - New Series " Gruppe/Group 6 Astronomy and Astrophysics " Volume 2 Schaifers/Voigt: Astronomy and Astrophysics / Astronomie und Astrophysik " Stars and Star Clusters / Sterne und Sternhaufen

Armstrong, J. T., Mozurkewich, D., Rickard, L. J., et al. 1998, ApJ, 496, 550

Baranne, A., Queloz, D., Mayor, M., et al. 1996, A&AS, 119, 373

Bolton, C. T. & Grunhut, J. H. 2007, in IAU Symposium, Vol. 240, IAU Symposium, ed. W. I. Hartkopf, P. Harmanec, & E. F. Guinan, 66

Bonneau, D., Clausse, J.-M., Delfosse, X., et al. 2006, A&A, 456, 789

Borkovits, T., Csizmadia, S., Forgács-Dajka, E., & Hegedüs, T. 2011, A&A, 528, A53

Borkovits, T., Érdi, B., Forgács-Dajka, E., & Kovács, T. 2003, A&A, 398, 1091

Borkovits, T., Rappaport, S., Hajdu, T., & Sztakovics, J. 2015, MNRAS, 448, 946
Breiter, S. & Vokrouhlický, D. 2015, MNRAS, 449, 1691
Butterworth, S. 1930, Wireless Engineer, 7
Campbell, W. W. 1909, Astrophysical Journal, 29, 224
Claret, A. 1998, A&AS, 131, 395
Claret, A. 2001, MNRAS, 327, 989
Conroy, K., Degroote, P., Hambleton, K., et al. 2013, in EAS Publications Series, Vol. 64, EAS Publications Series, ed. K. Pavlovski, A. Tkachenko, & G. Torres, 295–298
de Laverny, P., Recio-Blanco, A., Worley, C. C., & Plez, B. 2012, A&A, 544, A126
Degroote, P., Acke, B., Samadi, R., et al. 2011, A&A, 536, A82
Drimmel, R., Cabrera-Lavers, A., & López-Corredoira, M. 2003, A&A, 409, 205
Eggleton, P. P. & Kiseleva-Eggleton, L. 2001, ApJ, 562, 1012
Eggleton, P. P. & Tokovinin, A. A. 2008, MNRAS, 389, 869
Fabrycky, D. & Tremaine, S. 2007, ApJ, 669, 1298
Fekel, J. F. C. 1981, ApJ, 246, 879
Flower, P. J. 1996, ApJ, 469, 355
Fuhrmann, K., Chini, R., Hoffmeister, V. H., et al. 2011, MNRAS, 411, 2311
Hadrava, P. 1995, A&AS, 114, 393
Hadrava, P. 1997, A&AS, 122, 581
Hadrava, P. 2009, ArXiv e-prints
Harmanec, P. 1988, Bulletin of the Astronomical Institutes of Czechoslovakia, 39, 329
Harmanec, P. 1998, A&A, 335, 173
Harmanec, P. & Horn, J. 1998, Journal of Astronomical Data, 4, 5
Harmanec, P., Horn, J., & Juza, K. 1994, A&AS, 104, 121
Harrington, R. S. 1968, AJ, 73, 190
Harrington, R. S. 1969, Celestial Mechanics, 1, 200
Hummel, C. A., Benson, J. A., Hutter, D. J., et al. 2003, AJ, 125, 2630
Hummel, C. A., Mozurkewich, D., Armstrong, J. T., et al. 1998, AJ, 116, 2536
Hummel, C. A., Zavala, R. T., & Sanborn, J. 2013, Central European Astrophysical Bulletin, 37, 127
Kaufer, A., Stahl, O., Tubbesing, S., et al. 1999, The Messenger, 95, 8
Kraft, D. 1988, A software package for sequential quadratic programming, Deutsche Forschungs- und Versuchsanstalt für Luft- und Raumfahrt Köln: Forschungsbericht (Wiss. Berichtswesen d. DFVLR)
Lafrasse, S., Mella, G., Bonneau, D., et al. 2010, VizieR Online Data Catalog, 2300, 0
Lenz, P. & Breger, M. 2004, in IAU Symposium, Vol. 224, The A-Star Puzzle, ed. J. Zverko, J. Ziznovsky, S. J. Adelman, & W. W. Weiss, 786–790
Mason, B. D., Martin, C., Hartkopf, W. I., et al. 1999, AJ, 117, 1890
Moultaka, J., Ilovaisky, S. A., Prugniel, P., & Soubiran, C. 2004, PASP, 116, 693
Mourard, D., Clausse, J. M., Marcotto, A., et al. 2009, Astronomy and Astrophysics, 508, 1073
Mozurkewich, D., Armstrong, J. T., Hindsley, R. B., et al. 2003, AJ, 126, 2502
Nemravová, J. A., Harmanec, P., Bencheikh, J., et al. 2013, Central European Astrophysical Bulletin, 37, 207
Palacios, A., Gebran, M., Josselin, E., et al. 2010, A&A, 516, A13
Press, W. H., Teukolsky, S. A., Vetterling, W. T., & Flannery, B. P. 1993, Numerical Recipes in FORTRAN; The Art of Scientific Computing, 2nd edn. (New York, NY, USA: Cambridge University Press)
Prša, A., Degroote, P., Conroy, K., et al. 2013, in EAS Publications Series, Vol. 64, EAS Publications Series, ed. K. Pavlovski, A. Tkachenko, & G. Torres, 259–268
Prša, A. & Zwitter, T. 2005, ApJ, 628, 426
Prša, A. & Zwitter, T. 2006, Ap&SS, 304, 347
Rappaport, S., Deck, K., Levine, A., et al. 2013, ApJ, 768, 33
Rica Romero, F. M. 2010, Rev. Mexicana Astron. Astrofis., 46, 263
Shao, M., Colavita, M. M., Hines, B. E., et al. 1988, A&A, 193, 357
Simon, K. P. & Sturm, E. 1994, A&A, 281, 286
Soderhjelm, S. 1975, A&A, 42, 229
Soderhjelm, S. 1982, A&A, 107, 54
Steiner, I., Stahl, O., Seifert, W., Chini, R., & Quirrenbach, A. 2008, in Society of Photo-Optical Instrumentation Engineers (SPIE) Conference Series, Vol. 7014, Society of Photo-Optical Instrumentation Engineers (SPIE) Conference Series, 4
Stellingwerf, R. F. 1978, ApJ, 224, 953
Storn, R. & Price, K. 1997, Journal of Global Optimization, 11, 341
Tallon-Bosc, I., Tallon, M., Thiébaut, E., et al. 2008, in Society of Photo-Optical Instrumentation Engineers (SPIE) Conference Series, Vol. 7013, Society of Photo-Optical Instrumentation Engineers (SPIE) Conference Series
ten Brummelaar, T. A., McAlister, H. A., Ridgway, S. T., et al. 2005, ApJ, 628, 453
Tody, D. 1986, in Society of Photo-Optical Instrumentation Engineers (SPIE) Conference Series, Vol. 627, Instrumentation in astronomy VI, ed. D. L. Crawford, 733
Tody, D. 1993, in Astronomical Society of the Pacific Conference Series, Vol. 52, Astronomical Data Analysis Software and Systems II, ed. R. J. Hanisch, R. J. V. Brissenden, & J. Barnes, 173
Tokovinin, A., Mason, B. D., Hartkopf, W. I., Mendez, R. A., & Horch, E. P. 2015, AJ, 150, 50
Tokovinin, A. A. 1997, A&AS, 124, 75
van Belle, G. T., Creech-Eakman, M. J., & Hart, A. 2009, MNRAS, 394, 1925
van Leeuwen, F. 2007, A&A, 474, 653
Walker, G., Matthews, J., Kuschnig, R., et al. 2003, PASP, 115, 1023
Zasche, P., Uhlar, R., Kucakova, H., Svoboda, P., & Masek, M. 2014, Information Bulletin on Variable Stars, 6114, 1
Zasche, P. & Wolf, M. 2007, Astronomische Nachrichten, 328, 928

[1] Astronomical Institute of the Charles University, Faculty of Mathematics and Physics,
V Holešovičkách 2, CZ-180 00 Praha 8 - Troja, Czech Republic
[2] Laboratoire Lagrange, OCA/UNS/CNRS UMR7293, BP4229, 06304 Nice Cedex, France
[3] European Southern Observatory, Karl–Schwarzschild–Str. 2, 85748 Garching bei München, Germany
[4] Department of Physics & Astronomy, University of British Columbia, 6224 Agricultural Road, Vancouver, British Columbia, V6T 1Z1 Canada
[5] Université de Lyon, 69003, Lyon, France
[6] Université Lyon 1, Observatoire de Lyon, 9 avenue Charles André, 69230, Saint Genis Laval Cedex, France
[7] CNRS, UMR 5574, Centre de Recherche Astrophysique de Lyon, Université Lyon, 19 Avenue Charles André, 69561, Saint Genis Laval Cedex, France
[8] École Normale Supérieure, 69007, Lyon, France
[9] Hvar Observatory, Faculty of Geodesy, Zagreb University, Kačićeva 26, 10000 Zagreb, Croatia
[10] Département de physique, Université de Montréal, C.P. 6128, Succ. Centre-Ville, Montréal, QC H3C 3J7, and Observatoire du mont Mégantic, Canada
[11] Astronomisches Institut, Ruhr-Universität Bochum, Universitätsstraße 150, D-44780 Bochum, Germany
[12] Instituto de Astronomía, Universidad Católica del Norte, Avenida Angamos 0610, Casilla 1280 Antofagasta, Chile
[13] NASA Ames Research Center, Moffett Field, CA 94035, USA; SETI Institute, Mountain View, CA 94043, USA
[14] CHARA Array, Mount Wilson Observatory, Mount Wilson, CA 91023, USA
[15] Department of Astronomy and Physics, Saint Mary's University, Halifax, N.S., B3H 3C3, Canada
[16] Astronomical Institute, Academy of Sciences of the Czech Republic, 251 65 Ondřejov, Czech Republic
[17] Institute of Astronomy, University Vienna, Türkenschanzstrasse 17, A-1180 Vienna, Austria
[18] Département de physique, Université de Montréal, C.P. 6128, Succ. Centre-Ville, Montréal, QC H3C 3J7, and Observatoire du mont Mégantic, Canada
[19] Observatório do Instituto Geográfico do Exército, R. Venezuela 29 3 Esq., 1500-618, Lisbon, Portugal
[20] NASA Ames Research Center, Moffett Field, CA 94035, USA; SETI Institute, Mountain View, CA 94043, USA

Appendix A: Supplementary material to spectroscopic observations and its analyses

Details on the reduction procedure of the spectroscopic observations used in this study along with supplementary material to its analyses are given in this section.

Appendix A.1: Acquisition and reduction of the spectroscopic observations

The reduction procedure applied to spectra from different observatories (the labelling of observatories corresponds to the one introduced in Table 1) were following:

i) *OND*: All slit spectra were secured in the coudé focus of the 2 m reflector in Ondřjov, the Czech Republic,and recorded with the CCD detector PyLoN 2048x512BX. The bias subtraction, flat-fielding, and wavelength calibration were carried out in IRAF[15] (Tody 1986, 1993). The spectra were normalised with Hermite polynomials (order $k \leq 10$).

ii) *FER*: The echelle spectra were acquired with the 2.2 m ESO/MPG reflector at La Silla, Chile and reduced (the bias-subtraction, flat-fielding, and wavelength calibration) with a MIDAS pipeline developed specifically for the instrument (Kaufer et al. 1999). The studied regions of the reduced spectra were normalised with Hermite polynomials (order $k \leq 10$).

iii) *BES*: The spectra were acquired with an echelle spectrograph mounted at the 1.5 m Hexapode Reflector at Cerro Amazones, Chile, which is a clone of the FEROS spectrograph and the same MIDAS pipeline was used to carry out the reduction (the bias subtraction, flat-fielding, wavelength calibration). The studied regions were normalized with Hermite polynomials (order $k \leq 10$).

iv) *ELO*: The echelle spectra were obtained with the 1.93 m reflector at Observatory Haute Provence. The initial reductions (the bias subtraction, flat-fielding, wavelength calibration) were carried out with a pipeline described in Baranne et al. (1996). The studied regions were normalised with Hermite polynomials (order $k \leq 10$).

v) *DDO*: The slit spectra were acquired with the 1.88 m reflector at the David Dunlap Observatory. The initial reductions (the bias subtraction, flat-fielding, wavelength calibration) were carried out in IRAF. The spectra were normalised with Hermite polynomials (order $k \leq 10$).

vi) *LIS*: The slit spectra were acquired with the 0.356 m reflector at the Astronomical Observatory of the Instituto Geográfico do Exército, Lisbon. The dark-frame subtraction and flat-fielding were carried out in Maxim DL[16]. The wavelength calibration has been carried out using Neon comparison spectra and telluric lines in program Visual Spec[17]. Removal of the instrumental response was also carried out therein using Castor as a reference star. The spectra were normalised with Hermite polynomials (order $k \leq 10$).

Appendix A.2: Supplementary materials to analyses of spectroscopic observations

The spectroscopic supplementary material consists of following Tables and Figures:

i) Fig. A.1 shows comparison of the disentangled and synthetic profiles. The related analyses are described in Sections 3.5 and 3.3.

[15] IRAF is distributed by the National Optical Astronomy Observatories, which are operated by the Association of Universities for Research in Astronomy, Inc., under cooperative agreement with the National Science Foundation.

[16] Maxim DL is a commercial software designed for astronomical imaging `http://www.cyanogen.com/maxim\_main.php`.

[17] Visual Spec is a freeware designed for the wavelength calibration and the instrumental response removal `http://www.astrosurf.com/vdesnoux/index.html`.

Appendix B: Supplementary material to photometric observations and its analyses

Details on the reduction procedure of the photometric observations used in this study in along with supplementary material to its analyses are given in this section.

Appendix B.1: Acquisition and reduction of the photometric observations

The reduction procedure applied to photometric observations from different observatories (the labelling of observatories corresponds to the one introduced in Table 2) were following:

i) *HVAR*: The differential observations were obtained with the 0.65 m reflector at the Hvar Observatory, Croatia, which is equipped with a photoelectric photometer with and EMI 6256 tube. The observations were acquired relative to the comparison star 4 Tau with the check star 6 Tau observed as frequently as ξ Tau and transformed to the standard UBV ($UBVR$ for observations acquired after RJD = 56000) using the non-linear transformation implemented in the reduction package HEC22[18] (see Harmanec et al. 1994; Harmanec & Horn 1998). All observations were reduced with the latest release 17, which allows the time variation of linear extinction coefficients in the course of observing night.

ii) *HIPP*: The all-sky observations were acquired with the 0.29 m reflector of the Hipparcos satellite and transformed to V magnitude using the formulæ derived by Harmanec (1998).

iii) *SAAO*: The differential observations were acquired at the South African Astronomical Observatory, South Africa with 0.5 m reflector equipped with a photoelectric photometer. The observations were acquired relative to the comparison star 4 Tau and 6 Tau served as a check star and were transformed to standard Johnson system using HEC22.

iv) *VILL*: The differential observations were acquired with the Automatic Photometric Telescope at Villanova, the USA. The observations were taken relative to the comparison star 4 Tau and the 6 Tau served as a check star.

v) *MOST*: The all-sky observations were obtained with the 0.15 m reflector at the satellite MOST. The initial reduction was carried out according to Walker et al. (2003) and references therein. Removal of the remaining instrumental artefacts and the stray light from Earth's atmosphere is described in Section 4.

Appendix B.2: Supplementary materials to analyses of photometric observations

The photometric supplementary material consists of following Tables and Figures:

i) Fig. B.1 (B.2) available primary (secondary) light curve minima. All minima cover a time interval no longer than 30 d. See Section 4 for related analyses.

[18] The whole package along with a detailed manual, auxiliary data files, and results is available at `http://astro.troja.mff.cuni.cz/ftp/PHOT`

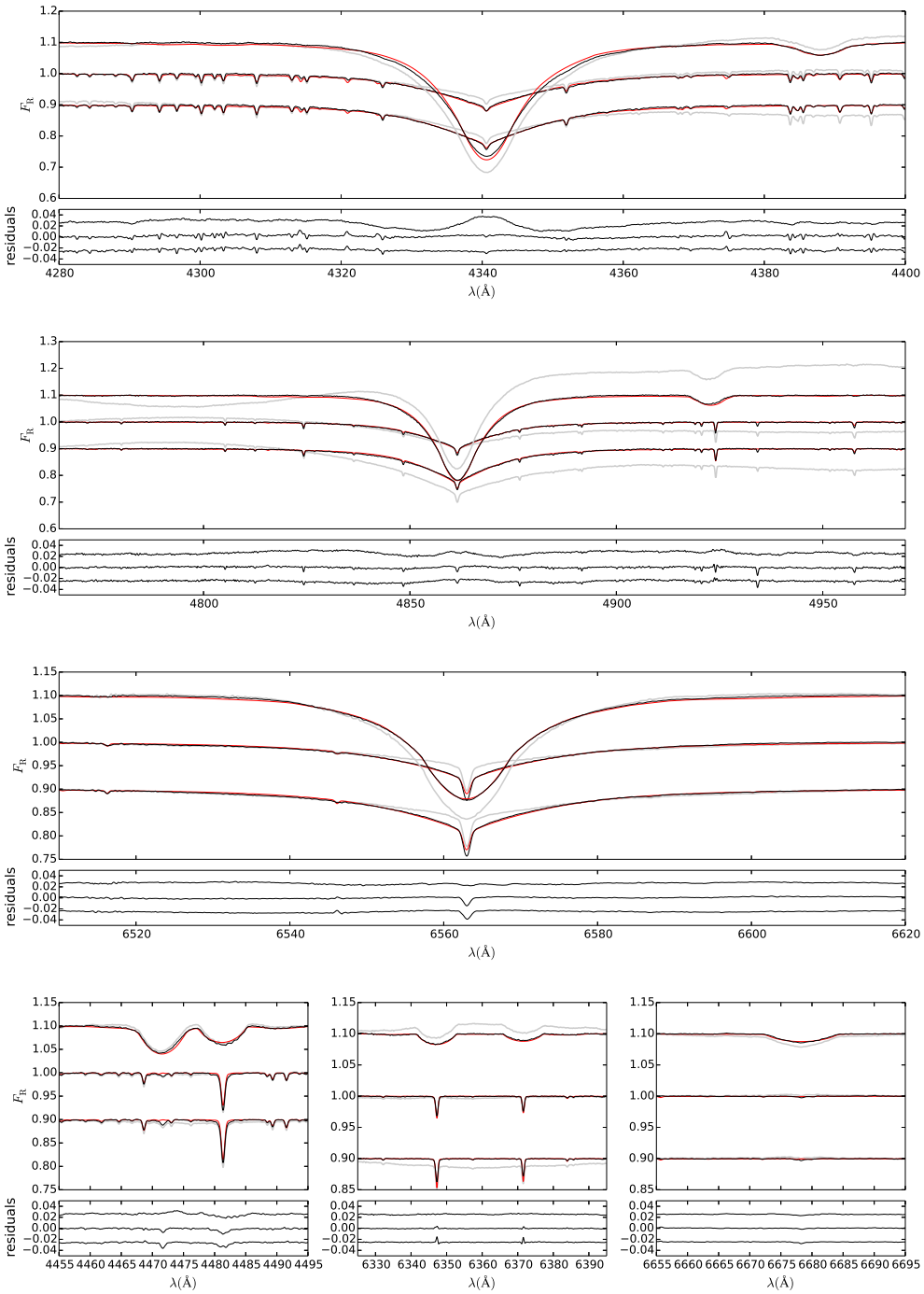

Fig. A.1. A comparison of the disentangled and synthetic spectra. The parameters defining the synthetic spectra are listed in section 3.5 In each panel: top spectrum - component B, middle spectrum - component Aa, bottom spectrum - component Ab, thick grey line - disentangled spectra, thin black line - disentangled and re-normalised spectra, thin red line - synthetic spectra. The residuals are computed for synthetic and re-normalised disentangled spectra.

Appendix C: Supplementary material to spectro-interferometric observations and its analyses

Details on the acquisition and reduction of the spectro-interferometric observations, along with Tables and Figures illustrating the analysis presented in section 6.

Appendix C.1: Mark III observations

The observations were carried out using a single North-South baseline three times in January 19, October 19, and November 2, 1991. The baseline length was 32 m in the first night, and 15 m in the two other nights. Visibilities were recorded in three narrow-band channels at 5000 Å, 5500 Å, and 8000 Å. μ and η Tau (limb darkened diameters of 0.41 mas and 0.98 mas, respectively, with 10% uncertainties) served as the calibrators. The calibrated visibilities were obtained from the Mark III data archive, which was

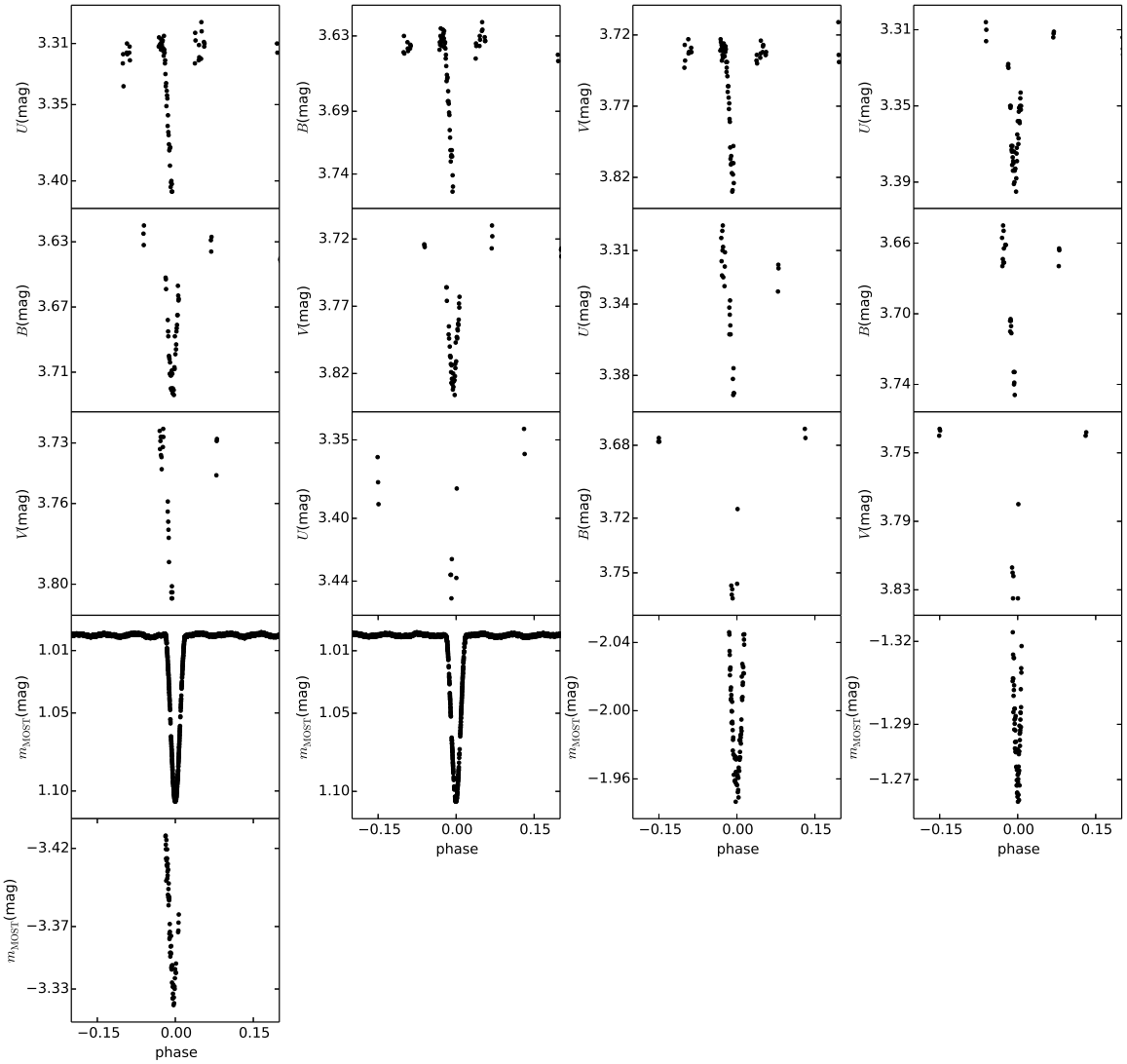

Fig. B.1. All available primary minima of orbit 1. The filters are denoted as follows: UBV - Johnson's UBV filters, $m_{\rm MOST}$, the filter of the satellite MOST.

created using the reduction and calibration methods described by Mozurkewich et al. (2003).

Appendix C.2: NPOI observations

The observations were carried out with the 3-beam combiner in 1998 and 2000, and from 2003 to 2013 with the 6-beam combiner. Visibilities, complex triple amplitudes and closure phases were recorded in 16 narrow-band channels between 5500 Å and 8500 Å. The journal of the NPOI observations including the calibrator stars is given in Table C.2, and the calibrator information is given in Table C.4.

The calibrators were taken from a list of single stars maintained at NPOI with diameters estimated from V and $(V-K)$ using the surface brightness relation by Mozurkewich et al. (2003) and van Belle et al. (2009). Values of $E(B-V)$ were derived from comparison of the observed and theoretical colours as a function of spectral type by Schmidt-Kaler in Aller et al. (1982). Values for the extinction derived from $E(B-V)$ were compared to estimates based on the maps by Drimmel et al. (2003), and used to correct V if they agreed within $0^{\rm m}.5$. Even though the surface brightness relationship based on $(V-K)$ colours is – to the first order – independent of the reddening, we included this small correction. The minimum (squared) visibility amplitudes corresponding to the diameter estimates are given in Table C.4 for all NPOI observation and show that the calibrators are either unresolved or only weakly resolved.

NPOI data and their reductions were described by Hummel et al. (1998) and Hummel et al. (2003). For the first time, we used

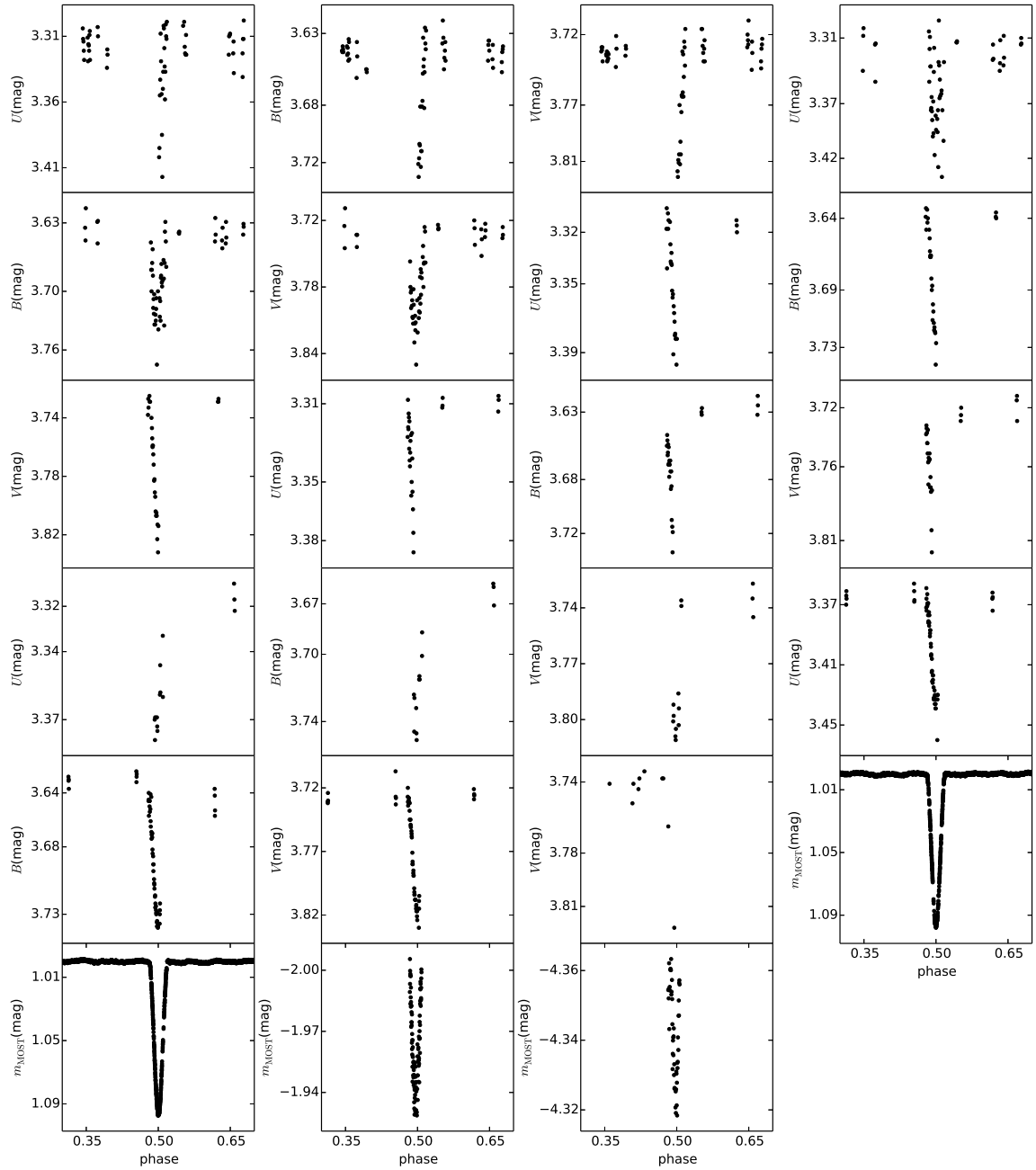

Fig. B.2. All available secondary minima of orbit 1. The filters are denoted as follows: UBV - Johnson's UBV filters, $m_{\rm MOST}$, the filter of the satellite MOST.

a pipeline written in GDL[19] for the OYSTER[20] NPOI data reduction package. The pipeline automatically edits the 1-second averages produced by another pipeline directly from the raw frames, based on expected performance such as the variance of fringe tracker delay, photon count rates, and narrow angle tracker offsets. Visibility bias corrections are derived as usual from the data recorded away from the stellar fringe packet. After averaging the data over the full length of an observation, the closure phases of the calibrators were automatically unwrapped so that their variation with time, as well as that of the visibility amplitude, could

[19] http://gnudatalanguage.sourceforge.net
[20] http://www.eso.org/$\sim$chummel/oyster

be interpolated for the observations of ξ Tau. For the calibration of the visibilities, the pipeline used all calibrator stars observed during a night to obtain smooth averages of the amplitude and phase transfer functions using a Gaussian kernel of 80 minutes in length. The residual scatter of the calibrator visibilities and phases around the average set the level of the calibration uncertainty and was added in quadrature to the intrinsic data errors. The amplitude calibration error of typically a few percent in the red channels up to 15% in the blue channels was added in quadrature to the intrinsic error of the visibilities. The phase calibration was good to about a couple of degrees.

Appendix C.3: VEGA/CHARA observations

The observations were carried out during two runs in 2011 and in 2012. Preliminary results, based on the observations obtained during the first run, were published by Nemravová et al. (2013). The reduction procedure was the same for both runs.

Five observations were acquired in 2011. All observations were obtained in the 3-telescope (3T) mode and included the CHARA baselines E1E2W2, W1W2S2, W2E2S2, ranging from 63 m to 245 m (E1, E2, S1, S2, W1, W2 denote the telescopes in the CHARA telescope array). Ten new observations were secured in 2012. Four of them were taken in the 3T mode and the remaining six were taken in the 2-telescope (2T) mode. The 2T observations included the CHARA baselines S2S1 and E2E1, their projected lengths ranging from 34 m to 66 m. The 3T observations contained the E2E1W2 and W2W1S1 baselines, their projected lengths were from 65 m to 279 m. A detailed journal of all interferometric observations with the instrument CHARA/VEGA is in Table C.3.

The observations were obtained with two cameras centred at 5350 Å (denoted BLUE) and 7300 Å (denoted RED) at spectral resolution $R \sim 6000$. Individual frames were recorded with a frequency 100 Hz and grouped into blocks containing 2500 frames. Each block was coherently summed up and each observation had from 20 to 90 blocks. Two 20 nm wide bands were chosen in the BLUE region and two 30 nm wide bands in the RED one. The four bands used are $\Delta\lambda_{\rm IF} = \{5320-5520, 5400-5600, 7000-7300, 7300-7600\}$[21] Å. The frames were summed up within these bands and the raw squared visibility $V_{\rm RAW}$ was derived from the sum. The spectral bands have to be narrow because of the limited coherence of the waves due to the atmospheric turbulence. There are no strong stellar lines in any of the four spectral bands used, the spectral band $7300-7600$ Å is affected by the telluric water vapour lines, but even those are smeared out by the low resolution of the spectra.

A calibrator was observed before and after each observation of ξ Tau. Calibrators were selected with the tool SearchCal (Bonneau et al. 2006) and their list along with their basic properties is given in Table C.5. The instrumental visibility was estimated according to formula:

$$V^2_{\rm SCI}(u,v) = V^2_{\rm SCI-RAW}\frac{V^2_{\rm CAL-UD}}{V^2_{\rm CAL-RAW}}(u,v), \qquad \text{(C.1)}$$

where $V^2_{\rm SCI}$ is the calibrated visibility of ξ Tau, $V^2_{\rm SCI-RAW}$ the raw visibility of ξ Tau, $V^2_{\rm CAL-UD}$ the visibility of an uniform disk with a diameter listed in Table C.5, and $V^2_{\rm CAL-RAW}$ the raw visibility of a calibrator. In order to avoid inaccurate observations, we removed all blocks having S/N<2 and whose optical path delay (OPD) differed from the mean OPD by more than 2σ. Such blocks usually represent only a random noise rather than a physical signal. In rare cases, when the raw visibility of ξ Tau was close to zero, but safely detected, and there was no suitable observation of a calibrator, the raw visibilities of ξ Tau were used in the analysis as if they were calibrated, but they were assigned an error $\Delta V^2 = 0.05$. It allowed us to save more usable observations for very long baselines giving strong constraints by low visibility measurements.

Appendix C.4: Night by night analysis of NPOI observations

The calibrated visibility and phase estimates are rich enough to permit night-by-night estimation of positions of individual components. Due to lower resolution, the NPOI interferometer is almost insensitive to the orbit 1 and diameters of the three components (Aa, Ab and B) of ξ Tau. Therefore the system was represented with two point sources, and relative position of component B and the eclipsing binary estimated. The results of the night-by-night analysis are given in Table C.1.

The uncertainty ellipses of position of the photocentre of orbit 1 (which is almost identical with its centre of mass due to similarity of both components of the eclipsing binary) relative to component B were computed from fits to contours of the χ^2 surfaces at the minima rather than deriving them from the interferometric PSF to take into account the limitations of fitting a component position very far from the phase centre. For the contour we chose 25% above minimum to get a reduced χ^2.

An astrometric fit to positions listed in Table C.1 confirms that NPOI is insensitive to the eclipsing binary, because the derived orbital properties do not differ significantly from those obtained from a global fit to V^2 presented in Table 9.

Appendix C.5: Supplementary materials to analyses of spectro-interferometric observations

The spectro-interferometric supplementary material consists of following Tables and Figures:

i) Table C.2 lists all available spectro-interferometric observations with NPOI and MARK III instruments. For each observation the observing stations, range of its baselines $[B_{\rm min}; B_{\rm max}]$, phase coverage of orbits 1, and 2 ϕ_1, ϕ_2, and associated calibrators are given. The numbering of calibrators is given by Table C.4.
ii) Table C.3 lists all available spectro-interferometric observations with CHARA/VEGA instrument. For each observation the lengths of projected baselines B and their orientation θ, the phase coverage of orbits 1, and 2 ϕ_1, ϕ_2, and associated calibrators are given.
iii) Table C.4 lists all calibrators which were used to calibrate NPOI observations of ξ Tau. For each calibrator its Johnson V magnitude, spectral type, colour index $V-K$, interstellar reddening $E(B-V)$, the minimum amplitude squared visibility V^2 and the uniform disk diameter $\theta_{\rm V-K}$ for wavelength range from V to K band are given.
iv) Table C.5 lists all calibrators which were used for CHARA/VEGA observations. For each calibrator the spectral type, effective temperature $T_{\rm eff}$, gravitational acceleration $\log g$, Johnson V (R) magnitude V (R), the uniform disk diameter in these bands $\theta_{\rm V}$, $\theta_{\rm R}$.

[21] The only difference between the reduction procedure of the observations acquired in 2011 and 2012 is in the choice of the spectral bands. The following bands were used in 2011 $\Delta\lambda_{\rm IF(OLD)} = \{5350-5450, 5450-5600, 7000-7200, 7100-7300, 7200-7400\}$ Å.

Table C.1. Astrometric positions of photocentre of orbit 1 relative to component B derived from night by night analysis of NPOI observations. ρ is the separation, θ the position angle measured counter-clockwise from the North, a, b and α are the semimajor axis, semiminor axis, and the position angle (again measured counter-clockwise from the North) of the uncertainty ellipse.

RJD	ρ (mas)	θ (deg)	a (mas)	b (mas)	α (deg)
48275.689	18.18	328.84	0.852	0.146	80.6
48548.925	15.20	323.62	2.490	0.219	72.8
48562.870	18.02	327.93	1.066	0.314	85.6
51093.906	9.71	145.08	0.831	0.157	177.1
51097.971	11.87	148.00	0.838	0.169	169.1
51171.722	18.31	327.53	0.844	0.153	173.7
51815.933	7.36	142.65	0.842	0.156	176.2
51835.927	11.98	149.63	0.853	0.163	171.7
52913.988	18.72	327.60	0.628	0.111	151.8
52927.944	18.46	328.68	1.962	0.223	149.7
52930.924	18.30	329.24	0.608	0.263	167.0
55463.974	12.48	148.89	1.874	0.256	152.7
55464.970	12.23	148.82	0.675	0.256	162.2
55465.970	12.22	149.96	0.666	0.252	162.2
55466.962	11.74	149.30	0.653	0.254	162.7
55467.963	11.41	150.01	0.651	0.256	162.8
55468.959	11.12	150.03	0.650	0.257	162.7
55469.886	10.93	150.16	0.624	0.274	180.0
55470.955	10.11	150.39	0.643	0.272	163.5
55999.608	10.00	334.30	2.952	0.229	130.3
56001.610	8.30	335.23	3.155	0.250	126.8
56221.917	5.90	318.92	0.424	0.091	158.9
56227.894	9.59	322.81	0.544	0.081	160.8
56228.900	10.52	324.06	0.609	0.098	154.1
56229.901	11.28	324.86	0.620	0.095	154.8
56230.899	11.53	324.83	0.631	0.088	156.9
56235.880	14.12	325.89	0.527	0.081	160.3
56236.878	14.59	325.94	0.497	0.088	158.4
56237.869	15.02	326.35	0.552	0.080	161.1
56238.864	15.45	326.38	0.550	0.080	161.2
56297.679	4.12	337.15	0.787	0.107	178.3

v) Table C.1 lists astrometric positions of the photocentre of the eclipsing binary relative to the component B (at $rho_{\rm B} = 0.0$). The positions were obtained for each observational night with the reduction package OYSTER. The related analysis is presented in Section 2.

vi) Figures C.1, C.2, C.3, C.4, C.4, C.5, C.6 show fit of the global model given by Eq. (9) and corresponding to parameters listed in Table 9.

Table C.3. Journal of the spectro-interferometric observations of ξ Tau. ϕ_1 (ϕ_2) denote the orbital phase of orbit 1 (2), B the mean length of the projected baseline, θ the position angle of the projected baseline. The calibrator stars are identified as follows: 1 - HD 21686, 2 - HD 18604, and 3 - HD 26793.

RJD	NB	ϕ_1	ϕ_2	B (m)	θ (deg)	Cal.
The 2011 run						
55825.8907	3-1	0.193	0.488	064.6	-155.9	1,2
	3-2			150.0	-160.6	1,2
	3-3			217.2	-158.9	1,2
55846.8703	3-1	0.129	0.633	065.8	-154.2	2
	3-2			155.8	-159.3	2
	3-3			221.4	-157.8	2
55850.8130	3-1	0.680	0.660	147.0	-160.9	1,2
	3-2			154.1	-090.1	1,2
	3-3			244.8	+056.0	1,2
55854.8645	3-1	0.247	0.688	065.6	-153.1	1,2
	3-2			156.2	-158.3	1,2
	3-3			221.6	-156.8	1,2
55854.9548	3-1	0.260	0.688	135.3	-148.5	1,2
	3-2			172.7	-057.7	1,2
	3-3			217.7	+084.1	1,2
55856.8928	3-1	0.531	0.702	063.3	-149.9	2,3
	3-2			152.5	-155.6	2,3
	3-3			216.3	-154.2	2,3
The 2012 run						
56194.8118	2-1	0.814	0.029	054.8	-156.0	1
56194.9180	2-1	0.829	0.030	065.9	-154.1	1
56197.8894	3-1	0.245	0.050	065.6	-155.2	1
	3-2			153.5	-160.1	1
	3-3			218.7	-158.6	1
56197.9362	3-1	0.252	0.051	065.0	-152.1	1
	3-2			155.6	-157.5	1
	3-3			220.4	-155.9	1
56200.0052	3-1	0.541	0.065	106.3	-002.5	1
	3-2			203.9	-060.1	1
	3-3			276.1	-041.1	1
56200.0306	3-1	0.545	0.065	099.2	-000.3	1
	3-2			207.7	-056.8	1
	3-3			278.3	-039.2	1
56226.9927	2-1	0.317	0.251	045.4	-125.8	1
56227.0299	2-1	0.323	0.251	040.0	-109.9	1
56227.8758	2-1	0.441	0.257	031.3	+100.3	1
56227.9720	2-1	0.454	0.258	033.4	+117.0	1

Notes. Ephemeris, which was used to compute the orbital phases: 1 - $T_{\rm min,1}({\rm RJD}) = 7.1467\times E + 56224.7246$, 2 - $T_{\rm p,2}({\rm RJD}) = 145.17\times E + 55609.05$,, where E is the epoch, $T^1_{\rm min}$ the epoch of the primary minimum of the orbit 1, $T_{\rm p,2}$ the epoch of the periastron passage of the orbit 2.

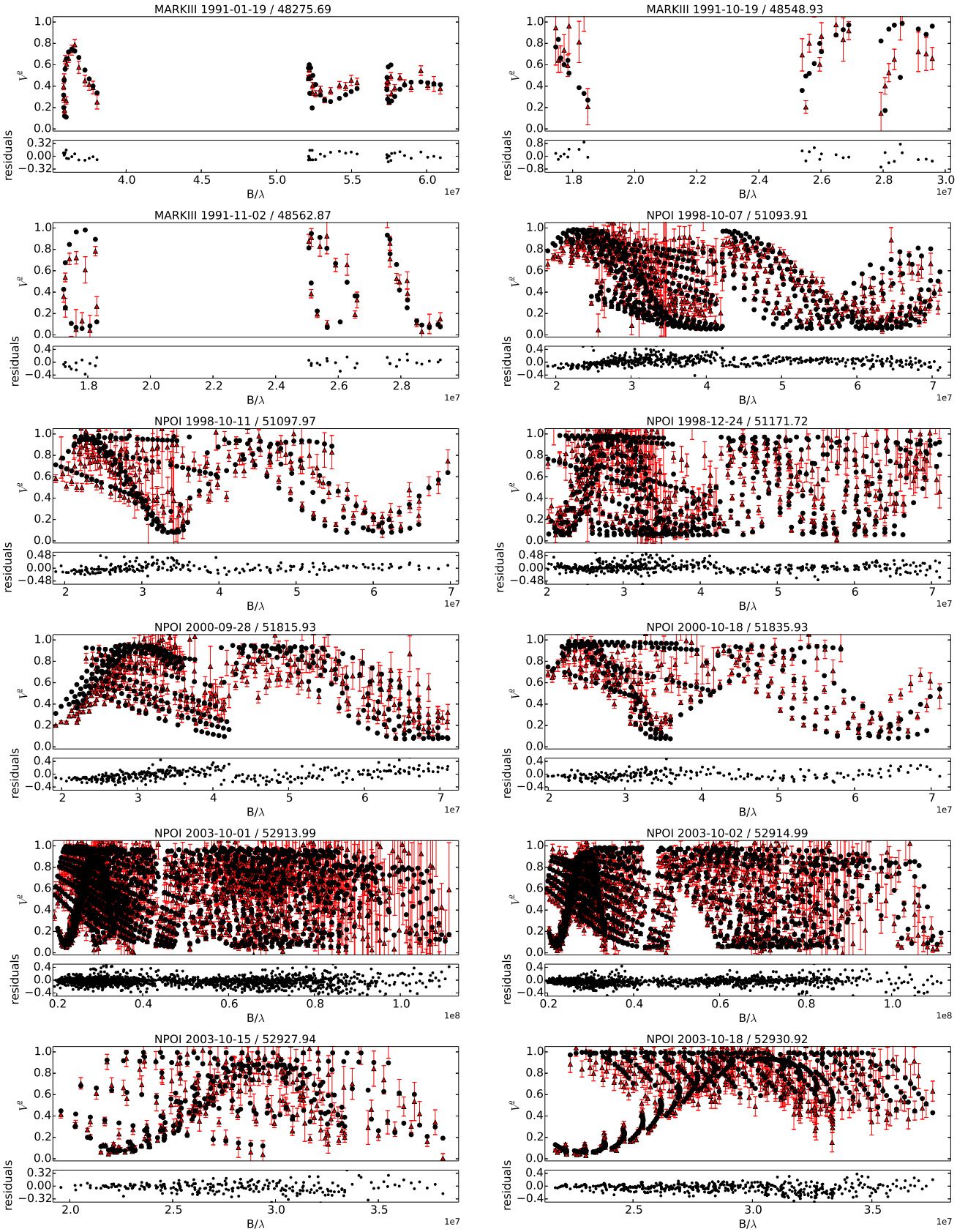

Fig. C.1. Best-fitting model (part one) plotted against the observations from the MARKIII and NPOI spectro-interferometers. Each panel - the observations are plotted with red triangles, the model corresponding to parameters listed in Table 9 is denoted with black points. Residuals of the fit are shown bellow each panel. The mean acquisition date, the corresponding mean heliocentric Julian date, and the instrument is indicated above each panel.

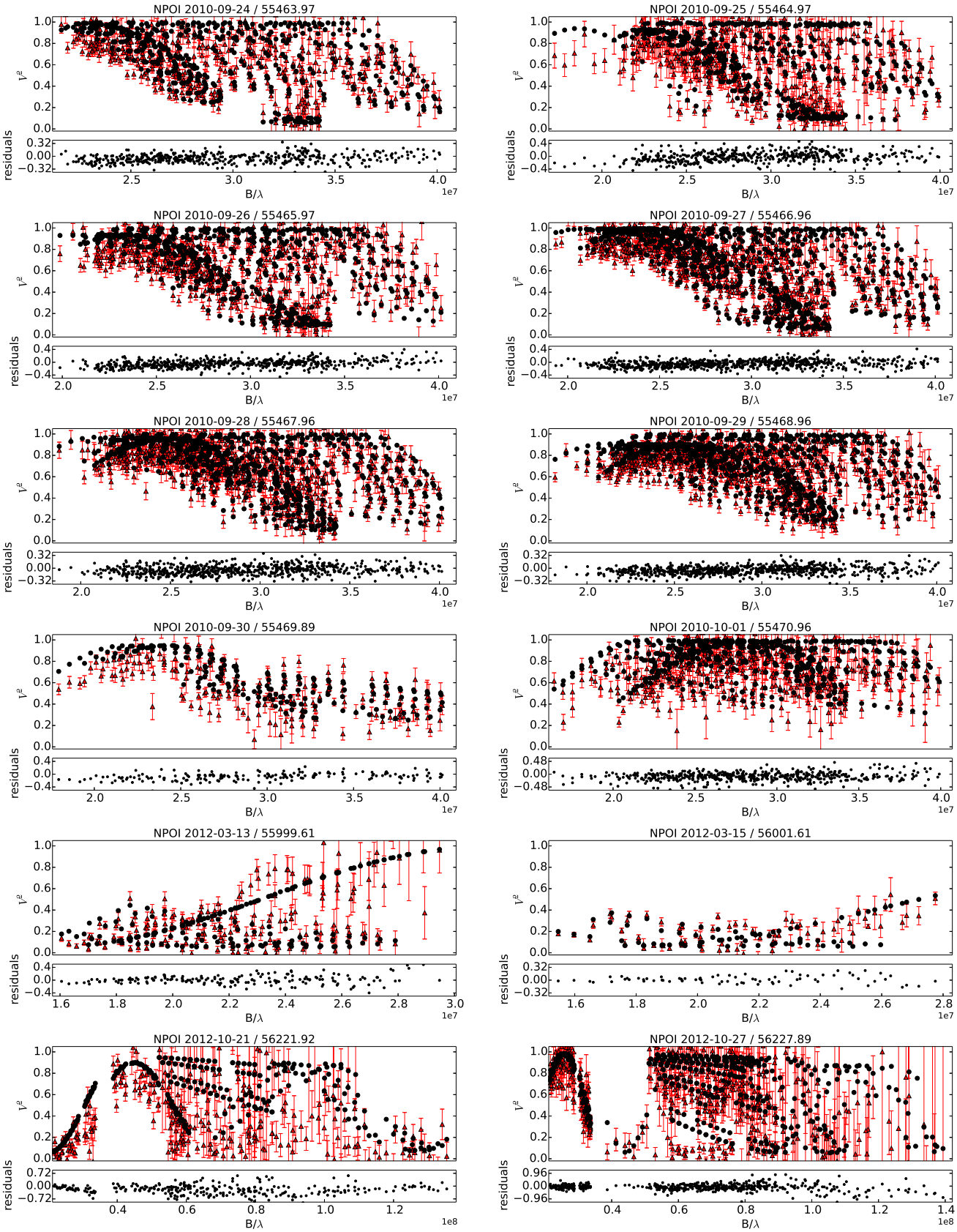

Fig. C.2. Best-fitting model (part one) plotted against the observations from the NPOI spectro-interferometer. Each panel - the observations are plotted with red triangles, the model corresponding to parameters listed in Table 9 is denoted with black points. Residuals of the fit are shown bellow each panel. The mean acquisition date, the corresponding mean heliocentric Julian date, and the instrument is indicated above each panel.

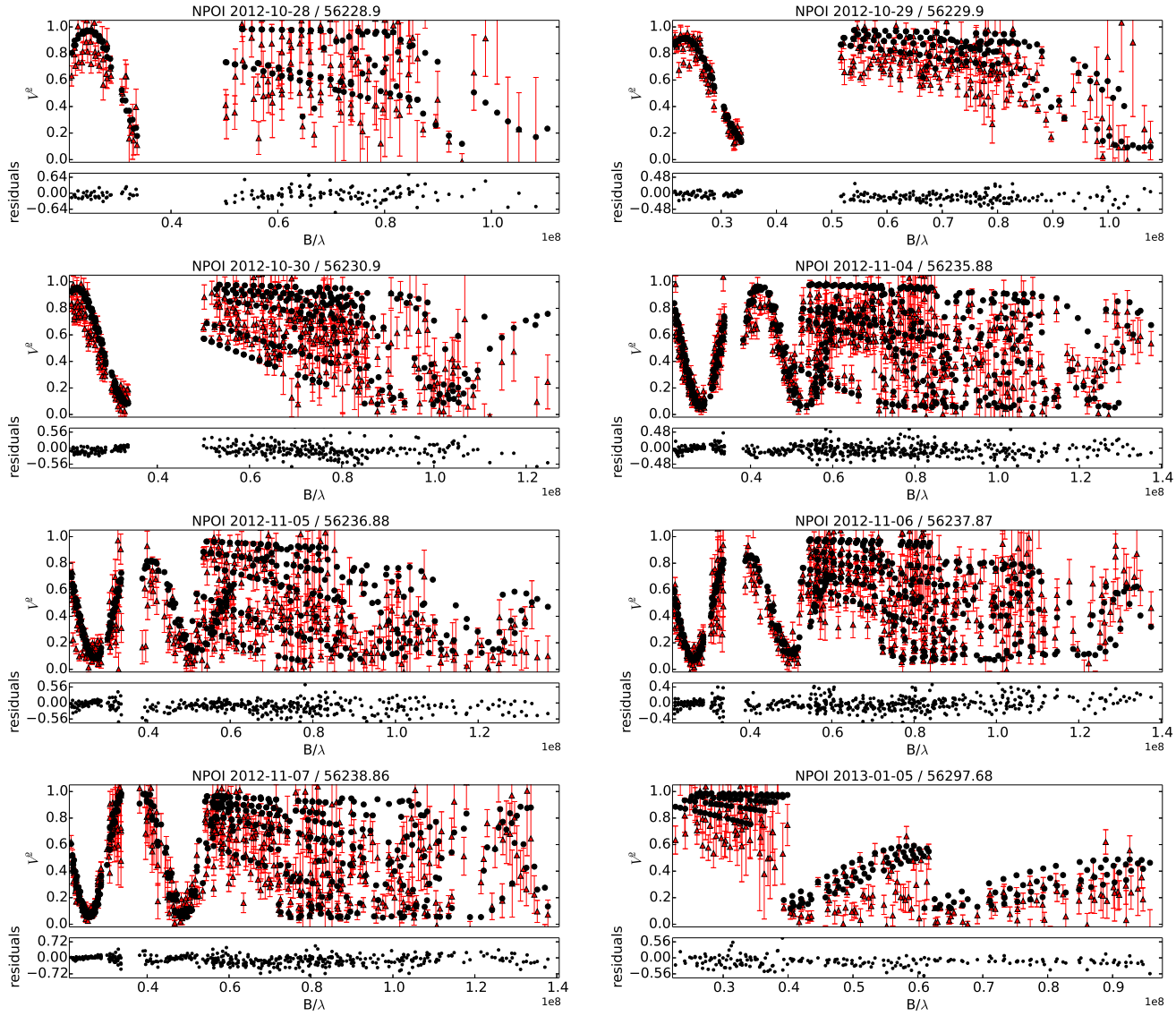

Fig. C.3. Best-fitting model (part one) plotted against the observations from the NPOI spectro-interferometer. Each panel - the observations are plotted with red triangles, the model corresponding to parameters listed in Table 9 is denoted with black points. Residuals of the fit are shown bellow each panel. The mean acquisition date, the corresponding mean heliocentric Julian date, and the instrument is indicated above each panel.

Table C.5. Properties of calibrator stars HD 21686, HD 18604. $T_{\rm eff}$ is the effective temperature, g the gravitational acceleration, $\theta_{\rm V}$ ($\theta_{\rm R}$) the uniform disk diameter for the filter V (R) of Johnson photometric system, V (R) magnitude of the calibrator in Johnson V (R) filter. They were adopted from Lafrasse et al. (2010).

Parameter	Unit	Value		
Calibrator		HD 21686	HD 18604	HD 26793
Spectral type		A0V	B6III	B9Vn
$T_{\rm eff}$	(K)	9790	13000	10500
$\log g_{\rm [cgs]}$		4.1	3.4	4.0
V	(mag)	5.125	4.703	5.210
R	(mag)	5.087	4.730	5.194
$\theta_{\rm V}$	(mas)	0.245(18)	0.257(18)	0.207(15)
$\theta_{\rm R}$	(mas)	0.247(18)	0.257(18)	0.209(15)

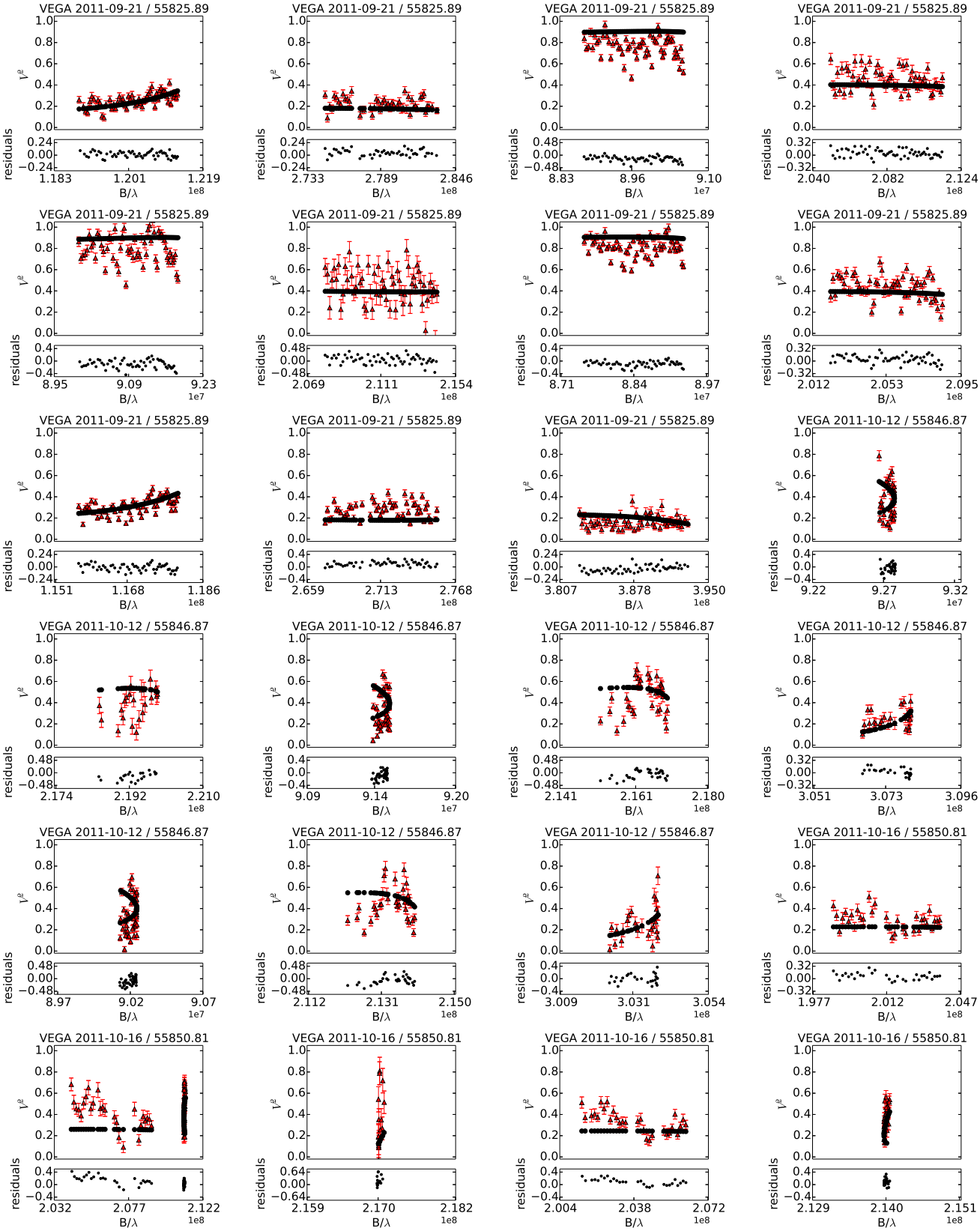

Fig. C.4. Best-fitting model (part one) plotted against the observations from the VEGA/CHARA spectro-interferometer. Each panel - the observations are plotted with red triangles, the model corresponding to parameters listed in Table 9 is denoted with black points. Residuals of the fit are shown bellow each panel. The mean acquisition date, the corresponding mean heliocentric Julian date, and the instrument is indicated above each panel.

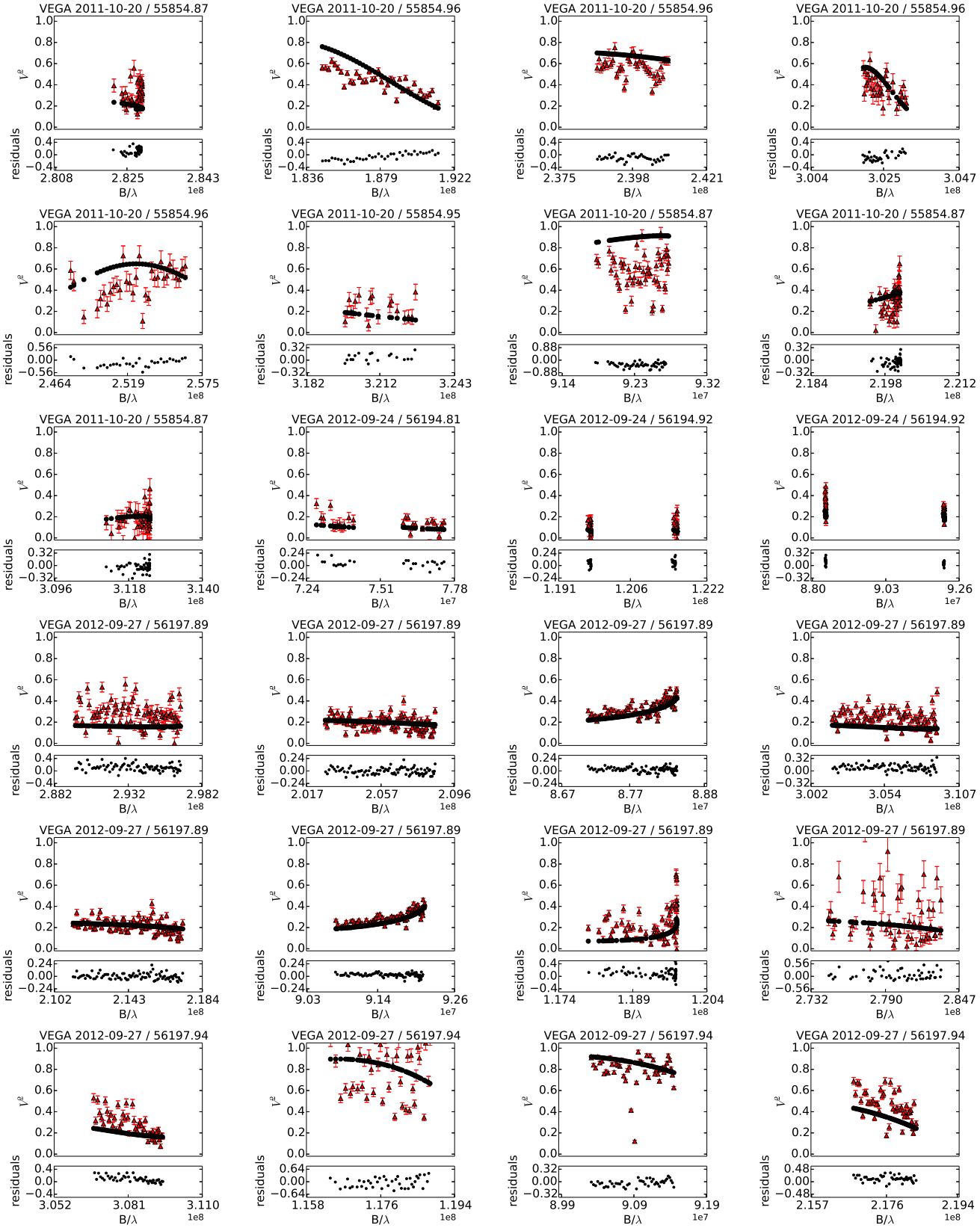

Fig. C.5. Best-fitting model (part two) plotted against the observations from the VEGA/CHARA spectro-interferometer. Each panel - the observations are plotted with red triangles, the model corresponding to parameters listed in Table 9 is denoted with black points. Residuals of the fit are shown bellow each panel. The mean acquisition date, the corresponding mean heliocentric Julian date, and the instrument is indicated above each panel.

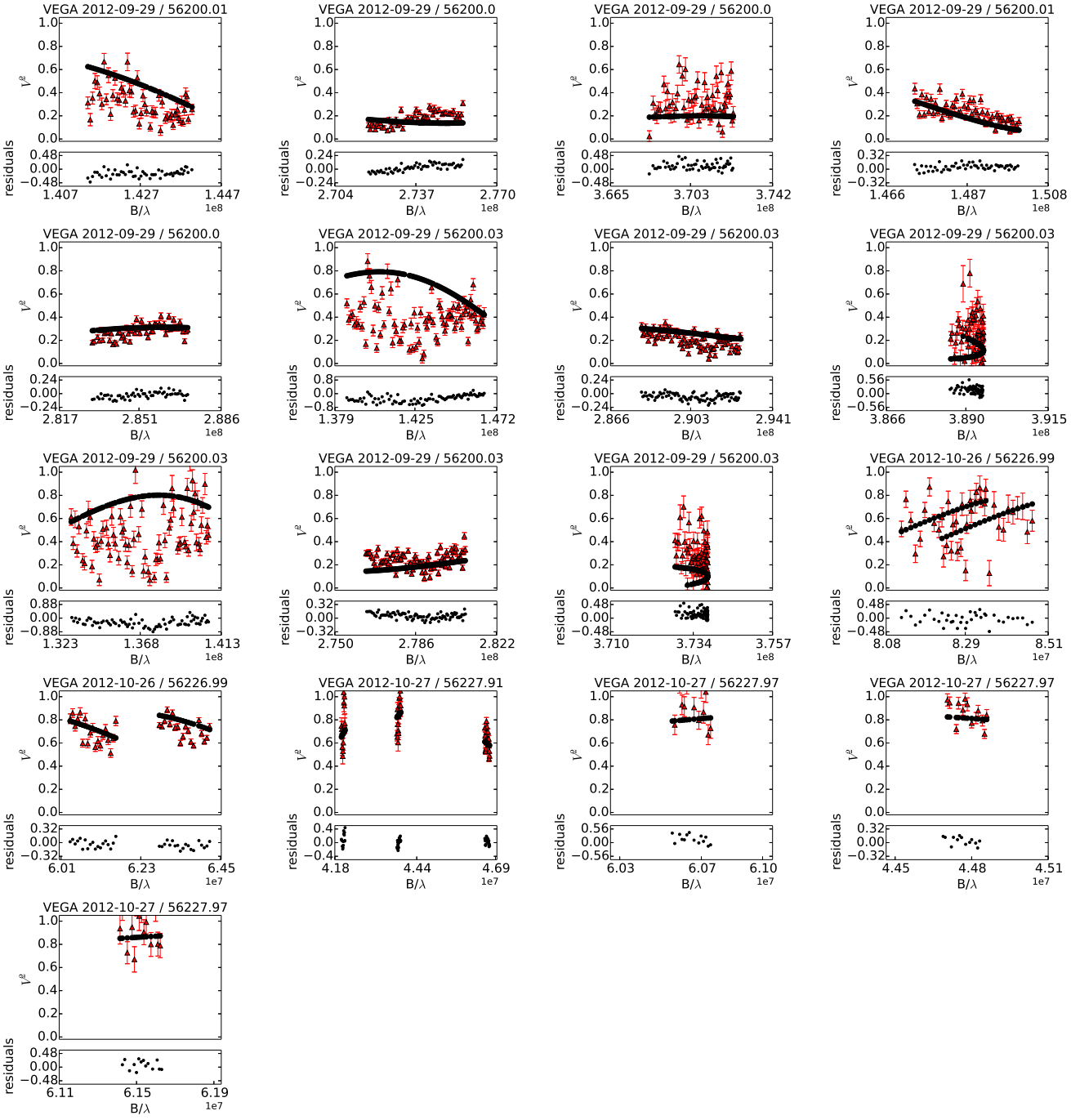

Fig. C.6. Best-fitting model (part three) plotted against the observations from the VEGA/CHARA spectro-interferometer. Each panel - the observations are plotted with red triangles, the model corresponding to parameters listed in Table 9 is denoted with black points. Residuals of the fit are shown bellow each panel. The mean acquisition date, the corresponding mean heliocentric Julian date, and the instrument is indicated above each panel.

Table 10. Summary of parameters derived from the spectroscopic, photometric, and spectro-interferometric analyses. In some cases more values are listed for a parameter, to show, that the methods do not contradict each other. The listed parameters are the anomalistic period $P_{\rm AN}$, the sidereal period $P_{\rm S}$, the periastron epoch $T_{\rm p}$, the epoch of the primary minimum $T_{\rm min}$, the semimajor axis a, the mass ratio q, the eccentricity e, the inclination i, the periastron argument ω, the position angle of the nodal line Ω, the effective temperature $T_{\rm eff}$, the surface gravitational acceleration $\log g$, the projected rotational velocity $v \sin i$, the mass M, the radius R, the angular diameter θ, the bolometric magnitude $M_{\rm BOL}$, the Johnson V magnitude and colour indices V, $B-V$, $U-B$, the deredened Johnson V magnitude and colour index V_0, B_0-V_0, the parallax π.

Parameter	Unit	Source	Value		
			Orbital properties		
Orbit			2	1	
$P_{\rm AN}$	(d)	RV/LC	145.598±0.041	7.14665±0.00001	
$P_{\rm S}$	(d)	RV/LC	145.110±0.061	7.14665±0.00001	
$T_{\rm p}$	(RJD)	RV/–	55609.07±0.57	–	
$T_{\rm min}$	(RJD)	–/LC	–	56224.72502±0.00022	
a	($R_\odot$)	IF+HP/IF+HP	218±15	23.6±1.9	
	($R_\odot$)	IF+RV/IF+RV	*229±14	25.513±0.093	
	($R_\odot$)	–/RV+LC	–	*25.553±0.090	
$a_{\rm angular}$	(mas)	IF/IF	15.778±0.0678	1.711±0.082	
e		RV/–	*0.2048±0.0048	0.0[1]	
		IF/–	0.220±0.0023	0.0[1]	
q		RV/RV	0.89±0.10	0.9439±0.0037	
i	(deg)	IF/IF	86.66±0.11	90.5±3.8s	
	(deg)	–/LC	–	*86.76±0.16	
ω	(deg)	RV/–	*8.07±1.48	90.0[1]	
	(deg)	IF/–	10.5±1.2	90.0[1]	
$\dot{\omega}$	(deg yr^{-1})	RV/–	3.04±0.28	0.0[1]	
Ω^2	(deg)	IF/IF	328.488±0.073	326.3±1.3	
			Component properties		
Component			B	Aa	Ab
$T_{\rm eff}$	(K)	SP	14190±150	10700±160	*10480±130
	(K)	LC	–	10700[1]	10378±22
$\log g_{\rm [cgs]}$		SP	4.527±0.041	4.08±0.12	4.01±0.10
		RV+LC	4.21±0.15	4.312±0.035	4.360±0.038
$v \sin i$	(km s^{-1})	SP	229.2±1.7	12.6±2.6	14.3±3.1
M	($M_\odot$)	RV+LC	*3.90±0.44	*2.253±0.027	*2.127±0.027
	($M_\odot$)	RV+IF	3.59±0.93	2.08±0.48	1.96±0.45
R	($R_\odot$)	RV+LC	–	1.736±0.069	1.596±0.069
	($R_\odot$)	IF+HP	2.45±0.27	–	–
θ	(mas)	IF	0.361±0.028	–	–
	(mas)	LC+HP	–	0.252±0.020	0.231±0.018
$M_{\rm BOL}$	(mag)	LC+RV+IF	-1.13±0.24	0.87±0.11	1.15±0.11
V	(mag)	LC	4.228±0.039	5.455±0.069	5.724±0.068
$B-V$	(mag)	LC	-0.137±0.067	-0.01±0.13	0.01±0.12
$U-B$	(mag)	LC	-0.409±0.062	-0.15±0.15	-0.13±0.15
V_0	(mag)	LC	4.095±0.28	5.32±0.54	5.54±0.52
B_0-V_0	(mag)	LC	-0.449±0.085	-0.049±0.167	-0.047±0.162
				Parallax	
$\pi_{\rm a_1}$	(mas)			14.40 ± 0.69	
$\pi_{\rm a_2}$	(mas)			14.83 ± 0.89	
$\pi_{\rm DM,Aa}$	(mas)			15.57 ± 3.95	
$\pi_{\rm DM,Ab}$	(mas)			15.57 ± 3.83	
$\pi_{\rm DM,B}$	(mas)			14.99 ± 2.49	

Notes. [1]Assumed. [2]A solution, where $\Omega_1 = 148.488 \pm 0.073$ and $\Omega_2 = 146.3 \pm 1.3$, is also plausible and has the same $\chi^{\rm R}$. *Parameters which we believe are the closest to the true nature of ξ Tau. Sources: RV.. solution of the RV curve presented in Table 4, SP.. comparison of the observed and synthetic spectra presented in Table 6, LC.. solution of the light curve presented in Table 7, IF.. solution of the V^2 presented in Table 9, HP.. the Hipparcos parallax $\pi = 15.60 \pm 1.04$ mas. The parallaxes: $\pi_{\rm a_1}$ estimated from the size of the semimajor axis of orbit 1 (physical and angular), $\pi_{\rm a_2}$ estimated from the size of the semimajor axis of orbit 2 (physical and angular), $\pi_{\rm DM,Aa}$ estimated from the distance modulus of component Aa, $\pi_{\rm DM,Ab}$ estimated from the distance modulus of component Ab, $\pi_{\rm DM,Ab}$ estimated from the distance modulus of component B.

Table 13. Initial osculating orbital elements $a_j, e_j, i_j, \Omega_j, \omega_j, M_j$ of ξ Tau system as derived by our N-body model. The epoch is $T_0 = 2456224.724705$. The values below correspond to the one of best-fit solutions with $\chi^2 = 2,578$, with individual contributions: $\chi^2_{\rm rv} = 2,237$, $\chi^2_{\rm etv} = 151$, $\chi^2_{\rm edv} = 3.3$ and $\chi^2_{\rm sky} = 185$. The masses of components in $M_\odot$ units were: $m_{\rm Aa} = 2.232904^{+0.000094}_{-0.000093}$, $m_{\rm Ab} = 2.009987^{+0.000094}_{-0.000093}$, $m_{\rm B} = 3.7339^{+0.0074}_{-0.0071}$ and $m_{\rm C} = 0.92^{+0.73}_{-0.06}$. The component B is on its lower limit $m_{\rm B,min}$. The mass of the component C is very poorly constrained, being rather a distant test mass compared to the others. The 3-σ uncertainties of the elements were determined by a simplified 1-dimensional χ^2 mapping, assuming a relative increase of χ^2 by a factor of 1.13, i.e. suitable for the number of degrees of freedom we have ($\nu = 908$). The uncertainty values were verified using the bootstrap method — with 100 random selections of datasets and corresponding simplex optimisation — but realistic uncertainties are likely to be larger than that because there are a number of local minima with statistically equivalent χ^2 values. We do not report a full correlation matrix of our solution here. Its non-diagonal terms indicate larger values of uncertainties for those elements which are strongly correlated or anti-correlated with others (e.g. $r_{m_{\rm Aa},\omega_2} = 0.74$, $r_{a_1,\Omega_2} = -0.77$, $r_{a_1,\omega_2} = -0.80$, $r_{a_3,i_3} = -0.79$).

Parameter	Value					Unit	Note
a_1	$0.1175670^{+0.0000007}_{-0.0000008}$	a_2	$1.08293^{+0.00034}_{-0.00032}$	a_3	$28.02^{+0.79}_{-0.79}$	au	
e_1	$0.0000^{+0.0021}_{-0.0000}$	e_2	$0.1974^{+0.0009}_{-0.0010}$	e_3	$0.564^{+0.023}_{-0.023}$		
i_1	$86.5^{+4.2}_{-1.5}$	i_2	$86.4^{+2.1}_{-1.7}$	i_3	$-24.4^{+13.6}_{-\ 8.6}$	deg	
Ω_1	$331.4^{+1.5}_{-2.0}$	$\Omega_2^\dagger$	$329.2^{+1.3}_{-1.2}$	Ω_3	$110.2^{+3.3}_{-3.4}$	deg	
ω_1	$274.10^{+0.16}_{-0.15}$	ω_2	$9.64^{+0.19}_{-0.11}$	ω_3	$7.0^{+3.2}_{-3.3}$	deg	
M_1	$176.02^{+0.18}_{-0.13}$	M_2	$85.74^{+0.17}_{-0.09}$	M_3	$31.8^{+1.4}_{-1.4}$	deg	
γ	$8.5^{+1.7}_{-1.7}$					$\mathrm{km\,s^{-1}}$	
i_1'	$93.5^{+1.3}_{-2.4}$					deg	mirror solution with $\chi^2 = 2,545$, Aa+Ab eclipses partially disappear
Ω_1'	$148.6^{+5.4}_{-2.7}$					deg	mirror solution with $\chi^2 = 2,749$, Aa+Ab eclipses partially disappear, orbit 1 is retrograde wrt. orbit 2
				i_3'	$23.6^{+\ 9.1}_{-16.0}$	deg	mirror solution with $\chi^2 = 2,678$

Notes. † The value is expressed in hierarchical Jacobian elements, with respect to Aa+Ab barycenter, because this pair is the most compact and massive. If the reference point would be the photocentre of the brigthest component B instead, the longitude of the ascending node would be shifted by -180°.

Table C.2. NPOI and MARK III observations of ξ Tau. Column two lists the configuration used as a triple of stations (e.g. "AC-AE-W7", using astrometric stations Centre and East, as well as imaging station W7) if data from all three involved baselines were recorded, including the corresponding closure phase. If a single baseline is listed, only squared visibility data were recorded but no closure phases on that baseline. ϕ_1 (ϕ_2) refers to mean orbital phase of orbit 1 (2) at the given RJD. Calibrator numbers correspond to the numbering in Table C.4.

RJD[1]	Triangles	$B_{\min}$ (m)	$B_{\max}$ (m)	ϕ_1	ϕ_2	Calibrators
		NPOI				
51093.906	AC-AE-AW	15	37	0.066	0.897	09 11 25 28 33
51097.971	AC-AE-AW	16	37	0.635	0.925	09 11 28 33
51171.722	AC-AE-AW	17	37	0.954	0.433	09 11 17 18
51815.933	AC-AE-AW	16	37	0.096	0.871	01 03 09 08
51835.927	AC-AE-AW	17	37	0.894	0.008	36 09 12 26 28 29 08
52913.988	AC-AE-W7AC-AW-W7	17	63	0.742	0.435	26 27 35
52927.944	AE-ACAW-AC	17	49	0.695	0.531	05 26 35
52930.924	AE-ACAW-AC	19	56	0.112	0.551	05 26 35
55463.974	AC-AEAC-AW	18	22	0.551	0.000	06 29 30 31 37
55464.970	AC-AEAC-AW	14	22	0.690	0.007	06 29 30 31 37
55465.970	AC-AEAC-AW	17	22	0.830	0.014	06 29 30 31 37
55466.962	AC-AEAC-AW	16	22	0.969	0.021	06 29 30 31 37
55467.963	AC-AEAC-AW	16	22	0.109	0.028	06 29 30 31 37
55468.959	AC-AEAC-AW	15	22	0.248	0.034	06 29 30 31 37
55469.886	AC-AEAC-AW	15	22	0.378	0.041	06 29 30 31 37
55470.955	AC-AEAC-AW	14	22	0.528	0.048	06 29 30 31 37
55999.608	AE-ACAW-AC	13	16	0.500	0.690	10 11 16 23
56001.610	AE-ACAW-AC	13	15	0.780	0.704	10 11 16 23
56221.917	AC-E6-W7AC-AE	19	73	0.607	0.221	01 07 11 34
56227.894	AC-AE-W7AC-E6-W7	19	79	0.443	0.262	32 07 11 30 34 02 37
56228.900	AC-AE-W7	18	64	0.584	0.269	32 07 11 13 30 34 02 37
56229.901	AC-AE-W7	19	67	0.724	0.276	32 07 11 13 30 34 02 37
56230.899	AC-AE-W7W7-E6	18	73	0.863	0.283	32 07 11 13 30 34 02 37
56235.880	AC-AE-W7AC-E6-W7	18	77	0.560	0.317	32 07 11 13 30 34 02 37
56236.878	AC-AE-W7AC-E6-W7	19	75	0.700	0.324	32 07 11 13 30 34 02 37
56237.869	AC-AE-W7AC-E6-W7	19	77	0.839	0.331	32 07 11 13 30 34 02 37
56238.864	AC-AE-W7AC-E6-W7	18	78	0.978	0.338	15 32 07 11 13 30 34 04 37
56297.679	AC-AW-E6	0	53	0.208	0.743	10 11 14 17 20 21 22 24 19
		Mark III				
48275.689	AC-AW-E6	29	30	0.725	0.484	μ Tau, η Tau
48548.925	AC-AW-E6	14	15	0.958	0.366	μ Tau, η Tau
48562.870	AC-AW-E6	14	15	0.909	0.462	μ Tau, η Tau

Notes. [1]Mean RJD. Ephemeris, which was used to compute the orbital phases: 1 - $T_{\min,1}(\mathrm{RJD}) = 7.1467 \times E + 56224.7246$, 2 - $T_{\mathrm{p},2}(\mathrm{RJD}) = 145.17 \times E + 55609.05$, where E is the epoch, $T_{\min,1}$ the epoch of the primary minimum of the orbit 1, $T_{\mathrm{p},2}$ the epoch of the periastron passage of the orbit 2.

Table C.4. List of NPOI calibrators used for ξ Tau, where V (K) is the apparent magnitude in the Johnson V (K) filter, $E(B-V)$ the interstellar reddening, V^2 the squared visibility and θ the uniform disk diameter.

No	HD	Type	V	$V-K$	$E(B-V)$	V^2	$\theta_{\mathrm{V-K}}$ (mas)
01	886	B2IV	2.83	-0.940	0.010	0.85	0.498
02	7804	A3V	5.16	0.239	-0.010	0.91	0.366
03	7964	A3V	4.76	0.224	-0.050	0.97	0.434
04	11171	F3III	4.65	0.778	-0.035	0.73	0.653
05	12216	A2V	3.98	0.059	-0.060	0.98	0.562
06	16582	B2IV	4.07	-0.632	0.020	0.99	0.343
07	17081	B7V	4.25	-0.255	-0.010	0.89	0.403
08	20630	G5Vvar	4.83	1.873	0.000	0.86	0.956
09	23630	B7III	2.90	0.264	0.010	0.85	0.981
10	24760	B0.5V	2.88	-0.833	0.110	0.91	0.519
11	25490	A1V	3.91	0.127	0.020	0.77	0.600
12	37128	B0Ia	1.70	-0.573	0.040	0.84	1.012
13	58946	F0V	4.16	1.182	0.010	0.61	0.831
14	71155	A0V	3.90	-0.179	0.000	0.99	0.502
15	75137	A0Vn	4.36	0.000	-0.020	0.97	0.454
16	76756	A5m	4.20	0.256	0.190	0.98	0.582
17	79469	B9.5V	3.88	-0.063	-0.016	0.95	0.546
18	97633	A2V	3.34	0.258	-0.060	0.88	0.858
19	98058	A7IVn	4.50	0.374	-0.040	0.98	0.536
20	98664	B9.5V	4.06	-0.079	-0.026	0.99	0.491
21	106625	B8III	2.59	-0.355	0.000	0.97	0.816
22	108767	B9V	2.95	-0.053	0.020	0.97	0.842
23	109387	B6IIIp	3.87	0.050	0.020	0.98	0.587
24	112413	A0p	2.90	-0.245	-0.120	0.97	0.763
25	156164	A3IV	3.14	0.332	0.000	0.88	0.987
26	176437	B9III	3.24	0.118	0.020	0.76	0.817
27	177724	A0Vn	2.99	0.114	0.030	0.85	0.919
28	184006	A5Vn	3.79	0.192	-0.010	0.93	0.668
29	192696	A3IV-Vn	4.30	0.222	0.030	0.96	0.536
30	195810	B6III	4.03	-0.351	0.020	0.88	0.421
31	196724	A0V	4.82	-0.034	0.000	0.99	0.360
32	209409	B7IVe	4.70	0.039	0.060	0.89	0.390
33	213558	A1V	3.77	-0.081	0.000	0.95	0.568
34	213998	B9IV-Vn	4.02	-0.216	-0.020	0.85	0.462
35	214923	B8.5V	3.40	-0.166	0.003	0.85	0.635
36	216735	A1V	4.90	0.060	-0.010	0.99	0.366
37	217891	B6Ve	4.53	-0.220	0.030	0.92	0.360